Fluxon Dynamics and Radiation Emission in Twofold Long Josephson Junction Stacks

Andreas Wallraff

Diplomarbeit in Physik
vorgelegt der
Mathematisch–Naturwissenschaftlichen Fakultät der
Rheinisch–Westfälischen Technischen Hochschule Aachen

angefertigt am
Institut für Schicht– und Ionentechnik des
Forschungszentrums Jülich (KFA)

January 27, 1997

Contents

Introduction

Since the theoretical prediction of the Josephson effect [Jos62] by B.D. Josephson in 1962 and its first experimental observation [AR63] by Anderson and Rowell in 1963, the physics of Josephson junctions has stimulated a great deal of experimental and theoretical research. Josephson junctions have always received a lot of attention due to their fascinating basic physical properties and the wide range of already existing or prospective applications.

From the point of view of basic physics, the features of Josephson junctions are intriguing because quantum mechanical properties of the junction are manifested by macroscopic quantities. That is the difference in phase between the two wavefunctions describing the superconducting electrons in each electrode is revealed by the current flowing through the junction and the voltage drop appearing across it. Up to date the most prominent device taking advantage of the quantum properties of the Josephson junction is the SQUID (superconducting quantum interference device), which is capable of measuring flux densities of less than 10^{-5} of the fundamental flux quantum Φ_0 in its pick–up loop. Further research is directed towards studying other quantum effects in Josephson junctions. Exciting new ideas to use mesoscopic long Josephson junctions to investigate macroscopic quantum tunneling (MQT) and macroscopic quantum coherence (MQC) have recently been presented [KI96].

Another major field in Josephson physics is concerned with non–linear electrodynamics in extended Josephson junctions, which I focus on in this diploma thesis. In this field a large extent of work is devoted to the investigation of fluxon dynamics in long Josephson junctions. Fluxons are soliton–like waves, which are also frequently called Josephson vortices or sine–Gordon kinks. The long Josephson junction, the electrodynamics of which is described well by the perturbed sine–Gordon equation, is an ideal experimental system to examine soliton dynamics. This system serves as a good model to test theoretical approaches to soliton dynamics and is a forerunner in the field of soliton research. Solitons also receive a lot of attention in a wide range of other fields like nonlinear optics, laser and plasma physics etc. .

This work is focused on soliton dynamics in stacked long Josephson tunnel junctions based on low temperature superconducting materials and its application to practical radiation sources. Single layer flux–flow oscillators are known to be suitable as radiation sources in the frequency range between 100 and 800 GHz [MKS$^+$95]. The maximum output power of such an oscillator is of the order of 1 μW. Both the power and the frequency of the radiation emitted by the oscillator can be tuned continuously in this range [MKS$^+$95]. Flux–flow oscillators are based on the unidirectional viscous flow of Josephson vortices along the junction [NEIY83, NEYI84, NEYI85]. The vortices propagate as electromagnetic pulses at a speed which is several percent of the speed of light in vacuum. Such flux–flow oscillators have recently found application in sub–mm wave band detector systems and integrated receivers [KSF$^+$96, KSF$^+$97]. Integrated receivers, which incorporate a detector and a local oscillator on the same superconducting chip are particularly attractive for space applications. In space applications integrated sub–mm receivers possess advantages over standard microwave detector and mixer technology due to the low power consumption and the small volume and weight. The most crucial limitation on the use of single long Josephson junctions as radiation sources is the limited output power available. Additionally, an increase in the available frequency range would be advantageous.

Currently there are two major approaches to increase the output power of Josephson oscillators:

- planar integration of small Josephson junctions into arrays,

- vertical integration of long Josephson junctions in stacks.

The objective of both approaches is to coherently operate a number of Josephson junctions in a phase locked mode to increase the available power. A power of as much as 0.85 mW has already been obtained from a coherently operating array of junctions [BB95]. However, it is difficult to adjust the power and the frequency of radiation in those structures. Vertical integration of long Josephson junctions seems to be a more feasible approach, due to the stronger mutual coupling between the junctions and the possibility to tune frequency and power.

By successfully coupling oscillations in long Josephson junctions coherently and phase locked, one would expect an increase in radiation power proportional to N^2 (for a not impedance–matched load) compared to a single oscillator, where N is the number of junctions comprising the stack. Additionally, the linewidth of the emitted radiation can be expected to decrease with the number of phase locked junctions in the stack. Recently, the intrinsic Josephson effect has been found in the highly anisotropic high T_c superconducting BiSrCaCuO single crystals [KSKM92, KM94]. These crystals can be regarded as an intrinsically stacked system of Josephson junctions. Therefore the experience gained with inter–layer fluxon interaction in low T_c Josephson stacks may lead to a better understanding of features of high T_c materials, that exhibit the intrinsic Josephson effect.

These prospects have stimulated the interest in investigating in detail the interaction of Josephson vortices in layered Josephson tunnel junctions. In this work attention is focused on the most simple stacked Josephson junction system, i.e. the twofold stack. Underdamped systems, in which the vortices have almost ballistic properties, are investigated. Flux–flow and different resonant structures in stacked Josephson junctions are shown to be well described by the Sakai–Bodin–Pedersen model [SBP93]. According to this model two major modes of vortex motion in twofold stacks do exist: the out–of–phase mode, in which fluxons in two junctions move coherently, but with a relative shift in phases of the corresponding electromagnetic waves and the in–phase mode, where fluxons move phase matched [SUK$^+$94]. Recently, both of these modes have been verified experimentally [UK96, SUIK96].

In this work the dynamics of fluxon propagation in twofold stacks of magnetically coupled long Josephson junctions is investigated in detail numerically and experimentally. In particular the different soliton propagation modes are studied with respect to the radiation characteristics of the stacked system.

In **chapter 1** the basic Josephson equations are briefly reviewed and the tunneling characteristics of Nb–Al/AlO$_x$–Nb type junctions are discussed. In **chapter 2** the fundamental equations governing the electrodynamics of single and stacked long Josephson junctions are presented. For the first time the Sakai–Bodin–Pedersen model is considered in the case of the twofold stack of Josephson junctions with *arbitrary parameters*. It is important to examine this case, because in stacked experimental systems the spread in parameters of individual junctions strongly influences its characteristics. Different classes of electromagnetic waves propagating in both types of junctions are discussed using examples of experimental measurements and numerical simulations performed in this work. A method for simulating the electrodynamics of the stacked flux–flow oscillator and analyzing the properties of its radiation field is presented in **chapter 3**. The coherent radiation emission from twofold stacked oscillators is studied. The main part of this work is also published in [WGU96]. Numerical results are subsequently compared to experimental measurements of the radiation emitted by a twofold linear stack and detected with an on–chip SIS detector. In **chapter 4** the phase locking of two annular long Josephson junctions with different damping parameters is analyzed numerically and theoretically. The implications of the results, which are accepted for publication [GWMU96], for the phase locking of stacked junctions are pointed out. An experimental method to observe these effects is suggested. **Chapter 5** comprises of a discussion of preliminary measurements of stacked annular Josephson junctions, which are to be extended in the future with respect to the issues discussed in chapters 3 and 4. For comparison, single junction measurements are also presented. The work is concluded by a summary and a discussion of some future prospects.

In the appendices several important but rather technical aspects of this work are discussed. A brief

outline of the fabrication technique of stacked Josephson junctions is presented in **appendix A**. The very important aspect of numerical Fourier transforms of periodic signals, used to calculate the radiation spectra in chapter 3, is discussed in detail in **appendix B**. In **appendix C** an approximate analytic solution of the sine–Gordon equation used in chapters 3 and 4 is calculated. Finally, some features of the stacked Josephson junction simulation program developed for this work are covered in **appendix D**.

Chapter 1

Basic properties of Josephson junctions

In this chapter the basic features of Josephson junctions are briefly reviewed. Effects that are of importance for later chapters are discussed in some detail.

1.1 Josephson junctions

Josephson junctions are systems, in which two superconductors are brought into contact such that an interaction via a *weak link* that suppresses the superconducting properties is possible. Different types of weak links providing the coupling between the superconductors are discussed in detail in the literature [Lik79]. The classic type of Josephson junctions is the superconductor–isolator–superconductor (SIS) tunnel junction, in which the Josephson effect, predicted by B.D. Josephson [Jos62] in 1962, was for the first time experimentally observed by Anderson and Rowell [AR63] in 1963. This thesis solely deals with junctions of the SIS type, which are most commonly used in low–T_c Josephson junction applications.

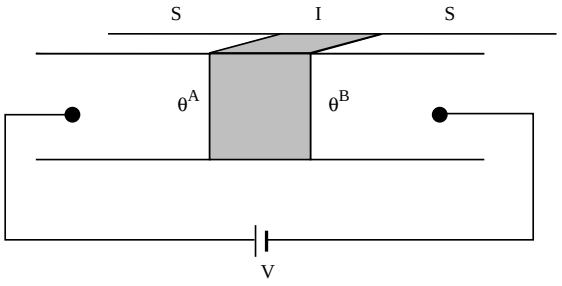

Figure 1.1: Voltage biased SIS type Josephson junction with quantum mechanical phases $\theta^{A,B}$ of the superconducting wavefunction in each electrode.

1.2 Josephson effect

Josephson predicted in [Jos62] that tunneling of the supercurrent carriers through a thin isolating barrier between the superconductors in a SIS type junction is possible. The supercurrent carriers are pairs of electrons with opposite spin and momentum. They are weakly bound by the phonon interaction with the crystal lattice and are called Cooper pairs. Due to the combination of spin and momentum the total angular momentum vanishes and the Cooper pairs have boson character. In good approximation they condense into a single quantum state that can be described by the effective macroscopic wavefunction

$$\Psi(\vec{r},t) = \sqrt{n(\vec{r},t)}\exp\left(i\,\theta(\vec{r},t)\right), \tag{1.1}$$

where $n(\vec{r},t)$ is the density of Cooper pairs, and $\theta(\vec{r},t)$ is a common phase factor. Here $\vec{r}$ is a three-dimensional coordinate in the bulk superconductor. If two superconductors are coupled as described in Sec. 1.1 the quantum mechanical tunneling problem can be solved [Jos62].[1] The local superconducting tunnel current density at zero voltage is found to be

$$j(\vec{r},t) = j_c \sin\left(\phi(\vec{r},t)\right) , \tag{1.2}$$

where $\phi = \theta^A - \theta^B$ is the difference of the superconducting phase between the two electrodes of the junction (see Fig. 1.1[2]). j_c is the maximum supercurrent[3] that can be sustained by the Josephson junction. Equation (1.2) is called *dc Josephson equation*. In Eqs. (1.2) and (1.3) $\vec{r}$ is a one or two-dimensional coordinate along the barrier of the junction.

As a constant dc voltage is applied to the tunnel junction the *ac Josephson equation* for the temporal evolution of ϕ is given by

$$V(\vec{r},t) = \frac{h}{2e}\frac{1}{2\pi}\frac{d}{dt}\phi(\vec{r},t) . \tag{1.3}$$

In this equation the local voltage drop V between the two superconductors and the rate of phase change between them are related by the fundamental flux quantum

$$\Phi_0 = \frac{h}{2e} = 2.07\ 10^{-15}\ \mathrm{Wb} \tag{1.4}$$

as the proportionality constant. An important quantity defined by this equation is the oscillation frequency of the phase difference per applied voltage unit

$$\frac{\frac{\partial\phi}{\partial t}}{2\pi V} = \frac{2e}{h} = 483.6\,\mathrm{GHz/mV} . \tag{1.5}$$

Equations (1.2) and (1.3) govern the behavior of Josephson junctions and will be used in the derivation of the electrodynamic properties of extended Josephson junction systems.

1.3 Gauge invariance of ϕ

In this section the spatial dependence of the phase difference across an extended junction on an applied magnetic field is briefly introduced. A full treatment can be found in [VDT81]. Considering the gauge invariant phase difference ϕ across the junctions as

$$\phi = \theta_2 - \theta_1 + \frac{2e}{\hbar}\int_{Q_1}^{Q_2} \vec{A}(x,t)\, d\vec{l} \tag{1.6}$$

and calculating the difference in ϕ between the points P and Q as in Fig. 1.2a according to Eq. (1.6) one finds

$$\phi(Q) - \phi(P) = \frac{2e}{\hbar}\left[\int_{P_1}^{P_2} \vec{A}(P,t)d\vec{l} - \int_{Q_1}^{Q_2} \vec{A}(Q,t)d\vec{l}\right] . \tag{1.7}$$

The flux through the path P' in Fig. 1.2a is given by

$$\Phi = \int_S \vec{B}\, d\vec{S} = \oint \vec{A}\, d\vec{l} = \int_{Q_2}^{Q_1} \vec{A}\, d\vec{l} + \int_{Q_1}^{P_1} \vec{A}\, d\vec{l} + \int_{P_1}^{P_2} \vec{A}\, d\vec{l} + \int_{P_2}^{Q_2} \vec{A}\, d\vec{l} , \tag{1.8}$$

[1] The quantum mechanical problem of Cooper pair tunneling was elegantly solved in the Schrödinger picture by Feynman [FLS65]. This derivation is most commonly quoted in standard textbooks [BP82, Lik86, PJFC95].

[2] Here voltage biasing is chosen as in the derivation of the Josephson equations. Though, in most other situations Josephson junctions are used in the current biased mode.

[3] Most textbooks (for example [PJFC95]) give references to analytical calculations of j_c from microscopic theory.

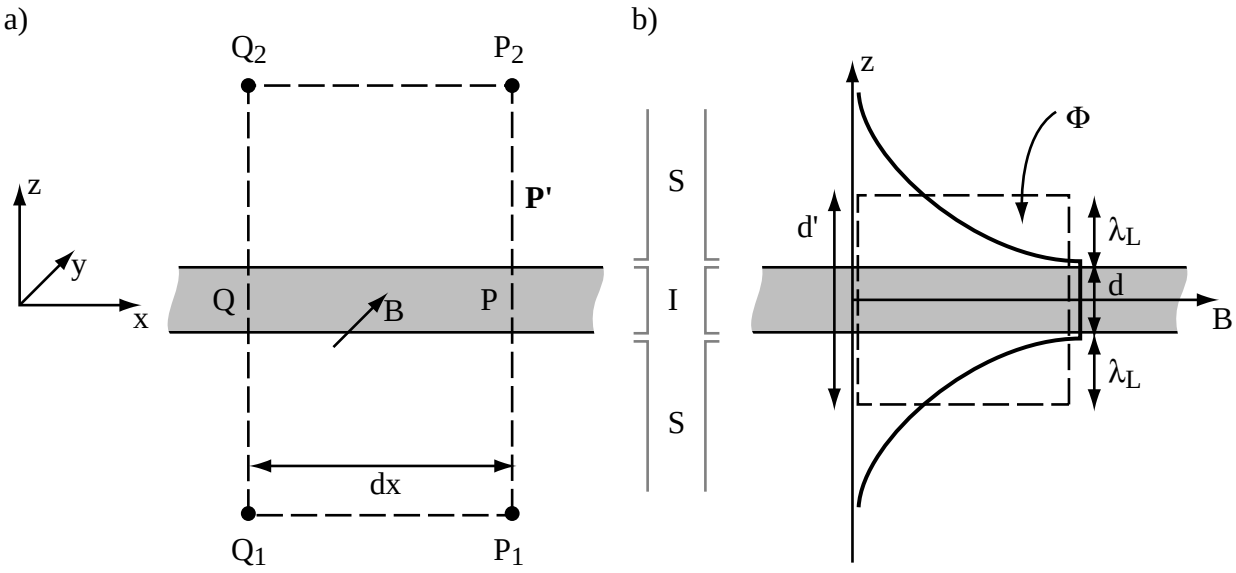

Figure 1.2: a) Closed path across the barrier of a Josephson junction. b) Magnetic field (thick line) penetration into the superconductor according to London equations. The total flux Φ in the interval dx of the junction is indicated by a dashed box.

where the second and fourth terms can be neglected if the horizontal parts of the path are chosen considerably deeper in the superconductor than the London penetration depth λ_L. Thus equating (1.8) and (1.7) leads to

$$\phi(Q) - \phi(P) = \frac{2e}{\hbar}\Phi \,. \tag{1.9}$$

Equation (1.9) can be transformed into a differential equation for ϕ by inserting the expression for the flux enclosed in an increment $dx = x_P - x_Q$ of the junction

$$\Phi = \frac{2ed'}{\hbar} B dx \tag{1.10}$$

where $d' = d + 2\lambda_L$ is the magnetic thickness of the junction calculated according to the magnetic field B penetrating to a depth of λ_L into the superconductor (see Fig. 1.2 b), d is the insulator thickness. Hence the expression for the gradient of ϕ considering the more general two-dimensional case is given by

$$\nabla\phi = \frac{2ed'\mu_0}{\hbar}\vec{H} \times \hat{z} \,. \tag{1.11}$$

This equation complements the basic Josephson equations in the sense that it relates ϕ to magnetic fields, where the dc Josephson equation relates ϕ to electric fields.

1.4 Tunneling regimes in Josephson tunnel junctions

Different tunneling processes in a Josephson junction can be identified by analyzing its current voltage characteristic (IV curve). A typical IV curve of an *underdamped* Josephson junction (see Sec. 2.1.1), prepared and measured at KFA, is shown in Fig. 1.3. Four major tunneling regimes can be identified:

- **Cooper pair tunneling (ZV):** At $V = 0$ lossless tunneling of Cooper pairs according to the dc Josephson effect is observed. The supercurrent reaches its maximum at I_c and the voltage abruptly rises to the gap voltage V_g which is related to the binding energy Δ of the Cooper pairs (energy gap Δ) by

$$V_g = \frac{2\Delta}{e} \,. \tag{1.12}$$

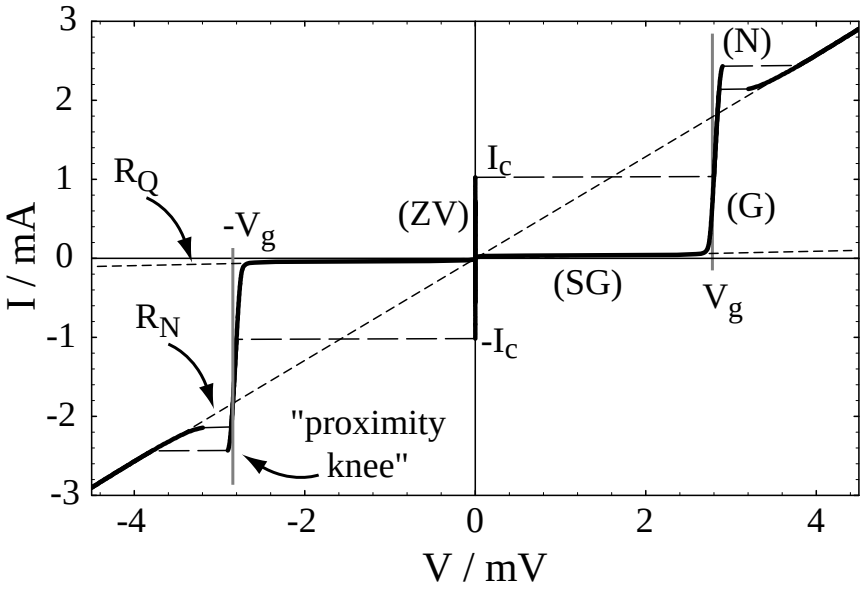

Figure 1.3: Current voltage characteristic of a long underdamped Josephson junction. Different tunneling regimes are indicated by labels (**ZV** – zero voltage, **SG** – sub–gap, **G** – gap, **N** – normal)

- **Gap voltage (G):** The gap voltage corresponds to the overlap of the quasiparticle densities of states of the two superconductors, giving rise to a large increase in the tunneling current.

- **Sub–gap quasiparticle tunneling (SG):** Upon decreasing the bias current such that the voltage drop across the junction is less than the gap voltage, a small sub–gap current is observed. This sub–gap current appears at finite temperatures $T > 0\,\mathrm{K}$ and is due to the quasiparticles excited above the energy gap. In terms of the phase difference ϕ, this state corresponds to a uniform rotation of ϕ, which is known as the McCumber solution [McC68]. Strictly speaking, such a spatially uniform rotation only exists in zero magnetic field. The subgap part of the IV curve is also termed McCumber branch.

- **Normal tunneling (N):** Substantially above the gap voltage one observes a linear dependence between the bias current and the voltage drop across the junction. This situation corresponds to the normal electron tunneling and reflects the normal resistance R_N of the junction.

The features described above can all be analytically calculated from the density of states in the different tunneling regimes. A concise review of the relevant tunneling processes can be found in [PJFC95].

The IV curve presented in Fig. 1.3 is measured at 4.2 K (i.e. liquid helium temperature). Most of the tunneling effects are strongly dependent on the temperature. The prominent features when increasing the temperature is a decrease in the gap voltage [proportional to the temperature dependence of the gap parameter Δ according to BCS theory [BCS57] (for a detailed discussion see [PJFC95])] and a reduction of the sub–gap resistance R_Q (due increased thermal excitation of quasiparticles). For a more detailed explanation of temperature effects, I refer to the literature [VDT81, PJFC95].

A remarkable feature in the IV curve of the Nb-Al/AlO_x-Nb junctions is the proximity knee structure indicated in Fig. 1.3. This knee can not be explained by the standard tunneling theory of SIS junctions and is not discussed in standard textbooks on Josephson junctions, even though it is present in most low T_c junctions. The modification of the current voltage characteristic in comparison to the expected SIS–like behavior is related to the more complex interface between superconducting and isolating layers in Nb-Al/AlO_x-Nb type junctions. In fact the sequence of layers in such a junction is more accurately described by a SNINS or SNIS structure, where N is indicating a normal metal, because the interface contains a non-oxidized Al layer which modifies the tunneling characteristics of the junction. In [GK88] a microscopic

model of such junctions is developed and current voltage characteristics are calculated. The main effect is the modification of the density of states in the SN system induced by the proximity effect. In comparison to the BCS density of states a pronounced singularity appears at energies below the bulk energy gap Δ, which reduces its effective value to Δ_{eff} [GK88]. Calculating IV curves with the modified densities of states qualitatively reproduces the knee feature observed in Fig. 1.3. More recently the theory was extended considering interfaces with finite transparencies [GHG$^+$95]. In this paper theoretical results are compared with recent experimental results in detail. Some extended discussion of this subject in the framework of Josephson junctions used as X–ray detectors can be found in [lG94, Gij95].

1.5 Flux–flow and other resonant structures

In the remainder of this thesis features of the current voltage characteristic of extended Josephson junctions at voltages below the gap voltage will be discussed in detail. Such features become visible in long Josephson junctions as resonant voltage steps. They are a manifestation of a complex spatial and temporal variation of the superconducting phase difference ϕ across the junction. In the next chapter the fundamental electrodynamics governing the evolution of ϕ are discussed.

Chapter 2

Electrodynamics in long Josephson junctions

In this chapter I present the equations governing the complex and very interesting electrodynamics of long Josephson junctions. First the dynamic equation for the propagation of electromagnetic waves on a single junction is derived and the various types of solutions are briefly introduced. Some examples of numerical and experimental manifestations of these effects, which were acquired during this work, are presented. In the second part a model for magnetically coupled stacks of Josephson junctions is applied to the two junction stack. The predominant effects of the coupling are pointed out by some numerical examples and references to experimental measurements are given.

2.1 Single long Josephson junctions

In this section some properties of single long Josephson junctions are discussed, to develop the theoretical foundation for the more complex coupled Josephson junction systems.

2.1.1 Geometry

Josephson junctions of the overlap geometry were considered in the numerical and experimental investigations carried out in this work. In the overlap geometry two planar superconducting electrodes get into contact via a thin insulating barrier forming a long Josephson junction (see Fig. 2.1). In addition to the

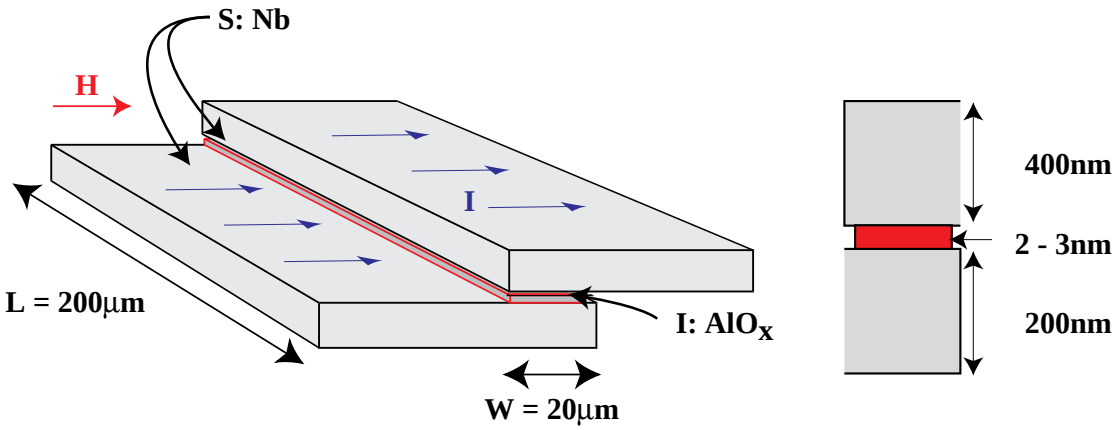

Figure 2.1: A typical linear long Josephson contact. a) Typical planar dimensions L, W. Directions of bias current I and externally applied magnetic field H are shown. b) Typical thicknesses of superconducting (Nb) and isolating (AlO_x) layers.

linear geometry shown in Fig. 2.1 Josephson junctions of annular geometry (Fig. 2.2) were simulated and experimentally tested, giving the possibility to examine different types of boundary conditions.

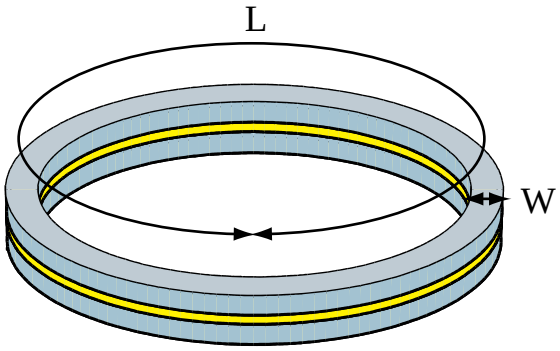

Figure 2.2: A typical annular long Josephson contact.

Typically a long Josephson junction has a length of about $L = 200\ \mu\mathrm{m}$ and a width of $W = 20\ \mu\mathrm{m}$. These dimensions are chosen with respect to the characteristic length scale of a Josephson junction called the Josephson length λ_J. Sometimes λ_J is also referred to as the Josephson penetration depth. A junction is called long, if $L/\lambda_J \gg 1$ and $W/\lambda_J \ll 1$. λ_J is formally introduced in Sec. 2.1.2.

The superconducting layers consist of niobium (Nb), which for the sputtered form employed in our laboratory has a London penetration depth of approximately $\lambda_L = 90\ \mathrm{nm}$. The insulating tunnel barrier consists of AlO_x, which is formed by partially oxidizing a thin film of sputtered aluminum. The Al/AlO_x tunnel barrier is about 5–$10\ \mathrm{nm}$ thick, of which 2–$3\ \mathrm{nm}$ are actually oxidized. In single junctions the superconducting layers are typically several $100\ \mathrm{nm}$ thick. A brief summary of the fabrication technique is given in Appendix A.

In the linear overlap geometry shown in Fig. 2.1 a bias current flows perpendicular to the longer dimension of the junction and a magnetic field is applied in the plane of the barrier.

2.1.2 Electrodynamics

Using Maxwell's equations, the Josephson relations, the gauge invariance of the superconducting phase and the expression for the quasiparticle tunnel current across the junction one can derive the wave equation of an extended Josephson junction.

Starting from the third Maxwell equation

$$\nabla \times \vec{H} = \vec{j} + \frac{\partial \vec{D}}{\partial t}, \tag{2.1}$$

and assuming linear and isotropic polarization of the barrier one can express the third component of Eq. (2.1) as

$$\frac{\partial H_y}{\partial x} - \frac{\partial H_x}{\partial y} = j_z + \epsilon_0 \epsilon_r \frac{\partial E_z}{\partial t}\ , \tag{2.2}$$

where the junction area is chosen parallel to the x–y plane and perpendicular to the z axes. The total current density across the barrier in the z–direction is given by

$$j_z = j_c \sin\phi + \sigma V + \sigma_i V \cos\phi\ , \tag{2.3}$$

where first term is the Josephson current density (1.2), the second term is the quasiparticle tunnel current density, and the third term is an interference term between the latter two current densities. σ and σ_i are the conductances of the respective processes. Usually the interference current can be neglected in SIS junctions, because of its small contribution to the overall current. The electric field E_z in Eq. (2.2) can be expressed as $E_z = V/d$, where d is the barrier thickness and V the voltage across it. Using the relation

between phase and voltage from the dc Josephson equation (1.3) and between phase and magnetic field from the gauge invariance (1.11) one can express Eq. (2.2) as a wave equation for the phase difference ϕ:

$$\frac{\hbar}{2e\mu_0 d'}\left(\frac{\partial^2\phi}{\partial x^2}+\frac{\partial^2\phi}{\partial y^2}\right)-\frac{\hbar}{2e}C^*\frac{\partial^2\phi}{\partial t^2}=j_c\sin(\phi)+\frac{\hbar\sigma_0}{2e}\frac{\partial\phi}{\partial t}\,, \tag{2.4}$$

where I introduced the specific capacitance

$$C^*=\frac{\epsilon\epsilon_r}{d}\,. \tag{2.5}$$

This type of nonlinear partial differential equation is called *perturbed sine–Gordon equation* (PSGE). Equation (2.4) can be rewritten in the following form

$$\lambda_J^2\left(\phi_{xx}+\phi_{yy}\right)-\frac{1}{\omega_p^2}\phi_{tt}=\sin\phi+\frac{1}{\omega_c}\phi_t\,, \tag{2.6}$$

where partial derivatives are expressed as $\frac{\partial X}{\partial\xi}=X_\xi$. The following quantities were introduced:

- The Josephson length λ_J

$$\lambda_J=\sqrt{\frac{\hbar}{2e}\frac{1}{\mu_0 j_c d'}}\,, \tag{2.7}$$

  which is the characteristic length scale over which ϕ may change.

- The plasma frequency ω_p

$$\omega_p=\sqrt{\frac{2e}{\hbar}\frac{j_c}{C^*}}\,, \tag{2.8}$$

  which is the characteristic oscillation frequency of ϕ.

- The characteristic damping frequency ω_c

$$\omega_c=\frac{2e}{\hbar}\frac{j_c}{\sigma} \tag{2.9}$$

  determines the relaxation rate of ϕ.

Dividing the Eq. (2.6) by λ_J^2 one can define the propagation velocity of linear waves in the junction as

$$c_0=\lambda_J\omega_P=\frac{1}{\sqrt{\mu_0 C^* d'}}\,, \tag{2.10}$$

which is also called the *Swihart velocity* [Swi61].

2.1.3 Normalization

In papers about long Josephson junctions Eq. (2.6) is often used in its more convenient normalized form. The spatial coordinates are normalized with respect to λ_J and time by $1/\omega_p$ according to

$$\tilde{t} = \omega_p t\,, \tag{2.11}$$

$$\tilde{x} = \frac{x}{\lambda_J}\,. \tag{2.12}$$

Thus Eq. (2.6) is transformed to the simple form

$$\phi_{\tilde{x}\tilde{x}}+\phi_{\tilde{y}\tilde{y}}-\phi_{\tilde{t}\tilde{t}}=\sin\phi+\alpha\phi_{\tilde{t}}\,, \tag{2.13}$$

where α is the normalized quasiparticle damping term

$$\alpha = \frac{\sigma}{\sqrt{\frac{2e}{\hbar} j_c C^*}} \,. \tag{2.14}$$

In units of Eq. (2.13) the Swihart velocity (2.10) is equal to unity. At this stage one can easily introduce a bias term $\gamma = j/j_c$ on the r.h.s. of Eq. (2.13), which models an externally applied uniform bias current. The implications of this term for the dynamics of the system are discussed later in this section.

In this model we neglected ac quasiparticle currents circulating in the superconducting electrodes. These would give rise to another damping term in Eq. (2.6) proportional to $\partial^3\phi/\partial x^2\partial t$. This term is often referred to as the β term and is treated in detail in [PPSD86, Pag87, DPP86], which include additional references.

Equation (2.13), in conjunction with the boundary conditions, models the electrodynamics of an extended homogeneous Josephson junction with good accuracy. All electromagnetic quantities (e.g. the local voltage and the magnetic field) can be derived from the superconducting phase difference ϕ across the junction.

2.1.4 Boundary conditions

From here on I will focus my attention on long quasi-one-dimensional Josephson junctions of overlap type geometry. A junction can be treated as one-dimensional, if its length L is much longer than the characteristic length λ_J and its width W is smaller than λ_J. As a result one can treat the phase ϕ as a constant value along the shorter dimension. We choose x to be the coordinate of the longer dimension. The normalized length of the junction is given by $\ell = L/\lambda_J$.

Hence the boundary conditions in the case of annular geometry can be written as

$$\begin{cases} \phi|_{\bar{x}=0} = \phi|_{\bar{x}=\ell} - 2\pi N \\ \phi_{\bar{x}}|_{\bar{x}=0} = \phi_{\bar{x}}|_{\bar{x}=\ell} \end{cases} \,. \tag{2.15}$$

In the first condition N fixes the number of 2π *phase shifts* (i.e. *fluxons*, see Sec. 2.1.5) on the length L. The second condition guarantees a continuous magnetic field distribution in the ring. For linear geometry boundary conditions are determined by the normalized magnetic field $\tilde{H}$:

$$\phi_{\bar{x}}|_{\bar{x}=0,\ell} = \tilde{H} \,. \tag{2.16}$$

$\tilde{H}$ can be calculated from the externally applied magnetic field and the junction properties according to Eq. (2.57) in Sec. 2.3.4. The boundary conditions are discussed in more detail when they are applied to the specific problem.

2.1.5 Properties of the wave equation

Equation (2.13) is a nonlinear partial differential equation for the variable ϕ. Because of its resemblance to the Klein–Gordon equation it is called perturbed sine–Gordon equation (PSGE). No exact analytic solutions to this equation are known. Therefore PSGEs have to be solved numerically or by using analytical approximation methods. Both approaches are used in this thesis.

Nevertheless non-trivial analytic solutions to the *unperturbed* one–dimensional sine–Gordon Equation (SGE)

$$\phi_{\bar{x}\bar{x}} - \phi_{\bar{t}\bar{t}} = \sin\phi \tag{2.17}$$

can be found. There are three main classes of solutions of (2.17) on an infinitely long spatial interval.

- **Solitons.** The most important solution is given by

$$\phi(x,t) = 4\arctan\left[\exp\left(\pm\frac{x - ut - x_0}{\sqrt{1-u^2}}\right)\right] \,, \tag{2.18}$$

where the (+) sign pertains to a soliton (kink) and the (-) sign to an antisoliton (antikink). The kink (antikink) corresponds to a 2π (-2π) change of the phase difference ϕ around the center of the kink located at $x = x_0$. Solitonic solutions appear in systems with a nonlinear dispersion relation and an additional nonlinearity. In these system dispersive effects, which lead to a spread of the energy of the waveform in space, and nonlinear effects compensate each other. As a result a stable solitary wave propagating at a velocity u can exist, while its energy stays localized in space.[1]

In Fig. 2.3a a plot of the soliton solution (2.18) at two values of the propagation velocity u is presented. In long Josephson junctions the derivative ϕ_x is proportional to the magnetic field [see Eq. (1.11)]. Thus the soliton (antisoliton) solution corresponds to a localized magnetic flux distribution, which is called a *fluxon* (*antifluxon*). In Fig.2.3b the magnetic field profiles are shown at the same values of u as in Fig. 2.3a. For $u \to c_0$ the function $\phi(x,t)$ is a step function centered at $x = x_0$ and all energy is localized at $x = x_0$.

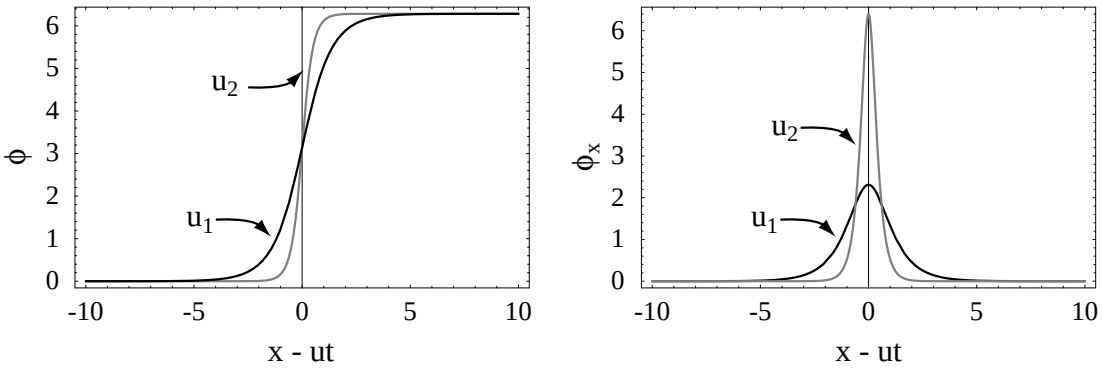

Figure 2.3: a) The soliton solution (2.18) plotted vs. $x - ut$ for the two velocities $u_1 = 0.5$ and $u_2 = 0.9$. b) The respective ϕ_x–profiles (i.e. magnetic field profiles).

Using a more general approach traveling wave solutions of Eq. (2.17) have been found by Kulik [Kul67]. These solutions can be understood as traveling chains of solitons . They are important if multi–soliton solutions or systems of finite length are considered.

- **Plasma oscillations.** This type of solution is related to an oscillation of the phase ϕ around an equilibrium phase angle ϕ_0. Analytical expressions for this solution, as well as for breather type solutions (see below), can be found in [CPS+78, Bar95].

- **Breathers.** This type of solution can be interpreted as a bound state of a soliton and an antisoliton. Breathers are unstable with respect to the perturbation terms in the PSGE (2.17) and decay after some transient time. Expressions for the above solutions on finite systems and open boundary conditions can be found in [CPS+78].

A very instructive discussion of different types of solutions to the perturbed sine–Gordon system is given in [CPS81]. In this paper by Cirillo et al. a mechanical analog to the long Josephson junction is presented and the different types of excitations are discussed in detail.

2.1.6 Relativistic invariance

In the field profile in Fig. 2.3b one can clearly observe a contraction of the soliton profile with increasing fluxon velocity. The contraction is often referred to as relativistic contraction of the fluxon. This can be understood by noting that the SGE is invariant under the Lorentz transform

$$x \quad \to \quad x' = \frac{x - ut}{\sqrt{1 - u^2}} \,, \tag{2.19}$$

[1] For other types of solitons in different systems see [KM89] or [Abd94]

$$t \rightarrow t' \frac{t - \frac{x}{u}}{\sqrt{1-u^2}} \,. \tag{2.20}$$

A very interesting direct observation of the Lorentz contraction of fluxons in an annular long Josephson junction by low temperature scanning electron microscope (LTSEM) measurements was recently presented in [LDL+95].

2.2 Fluxon motion in single long Josephson junctions

In this section I briefly discuss fluxon dynamics in single junctions of the annular and linear types by giving some basic examples of my measurements and numerical simulations.[2]

2.2.1 Annular junctions

Long annular junctions allow the analysis of fluxon dynamics without disturbing interactions with the boundaries. The motion of one or multiple fluxons in an annular junction is manifested by the appearance of sub–gap voltage steps in the IV curve of the junction. As an example, a measured IV curve of an annular junction with three trapped fluxons ($N = 3$) is shown in Fig. 2.4.[3] In comparison to a junction with no trapped fluxons (see Fig. 1.3), the Josephson current I_c at zero voltage is strongly suppressed. Even a small bias current causes the trapped fluxon to move along the junction inducing a finite voltage state as explained below.

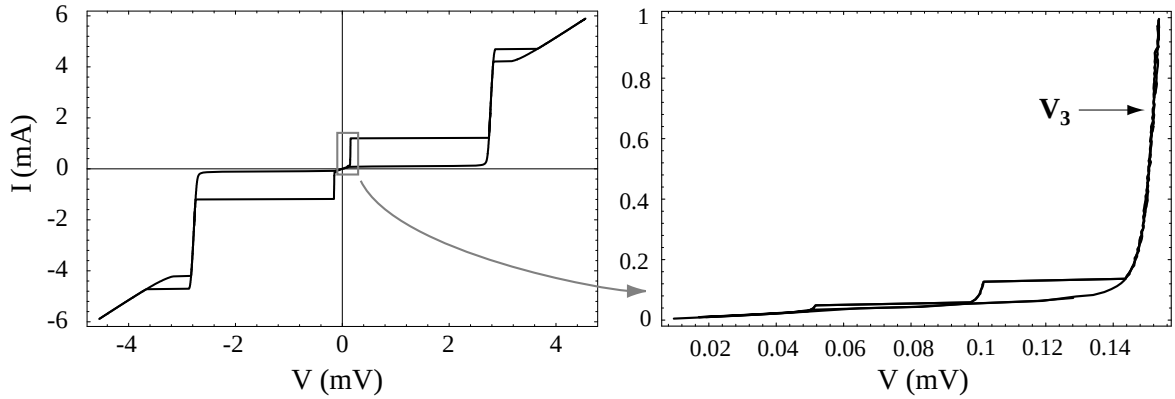

Figure 2.4: Measured IV curve of a long annular Josephson junction ($N = 3$, $L = 400\ \mu\mathrm{m}$). Left plot shows the full IV curve with trapped fluxons, right plot is a close up of the flux–flow step. In the right plot at low bias currents the first and second flux–flow steps are visible because of some pinning potentials in the junction preventing the fluxon chain to move as a whole at low bias.

The asymptotic voltage of a **fluxon step** is given by the equation

$$V_N = \Phi_0 \frac{N c_0}{L} \,, \tag{2.21}$$

where N is the number of fluxons in the junction, c_0 is the Swihart velocity, and L is the circumference of the junction. This expression is a simple consequence of the ac Josephson equation (1.3). It can easily be derived by considering $d\phi$ as the number N of 2π kinks passing through a given point in the junction during the time interval $dt = L/c_0$.

The shape of the current voltage step is determined by the dependence of the fluxon velocity u on the bias current $\gamma = I/I_c$ and reflects the dynamics of fluxons in the junction. The fluxon dynamics are

[2] The numerical method to solve the PSGE is discussed in Sec. 3.2.

[3] Details on how to prepare an annular junction in a state with a certain number of trapped fluxons can be found in chapter 5.

very well described by the PSGE and, generally, direct numerical simulations of IV curves are in good agreement with experiment. As an example a numerically simulated IV curve of an annular junction with three trapped fluxons is shown in Fig. 2.5. The normalized bias current is given by γ and the voltage is expressed as

$$V_{(norm.\,units)} = \frac{\langle \phi_t \rangle}{\frac{2e}{\hbar}\frac{c_0}{L}} \,, \tag{2.22}$$

such that the asymptotic voltage is identical to the number of fluxons N enclosed in the junction.

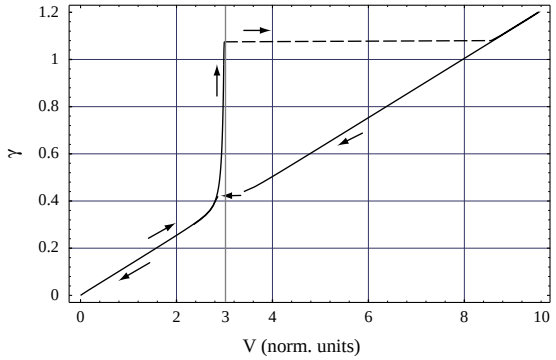

Figure 2.5: Numerically simulated annular Josephson junction IV curve. ($N = 3$, $\alpha = 0.1$, $\ell = 5$). Dashed lines indicate switching of the junctions state to and from the McCumber branch (see Sec. 1.4). Arrows show the hysteresis of the IV curve upon sweeping γ up and down again.

2.2.2 Linear junctions

In linear junctions fluxons interact with the boundaries of the system. This interaction strongly influences the dynamics of fluxons inside the junction. In long junctions three major regimes of fluxon motion can be observed.

- **Zero Field Steps (ZFSs).** If no external magnetic field is applied to a long Josephson junction and certain bias conditions are met, fluxons can be nucleated and give rise to ZFSs in the current-voltage characteristic of the junction. The applied bias current drives the fluxon, which is reflected at the boundaries with a change of its polarity (fluxon $\rightarrow$ antifluxon and vice versa). The fluxon dynamics are again reflected by the shape of the voltage step. Its resonant position is given by Eq. (2.21), where N now is the ZFS number ($N = 1, 2, 3, \ldots$). A detailed discussion of ZFSs can be found in [Ped82].

- **Fiske Steps (FS).** Fiske resonances arise, if a magnetic field exceeding a certain critical value is applied to a long linear junction. In the biased junction fluxons nucleate at one end and are annihilated at the other end of the junction. Upon the annihilation of the fluxon plasma waves are generated. These plasma waves resonate as cavity modes of the long junction, generating so called Fiske modes [Fis64]. The detailed physical mechanism of Fiske steps in long Josephson junctions is rather complex, but in relatively high magnetic fields FSs are described with a good accuracy by the Kulik theory [Kul67]. More recently, Fiske steps have been analyzed in [GJC94].

- **Flux–Flow Steps (FFSs).** At high magnetic fields the resonant Fiske states overlap with each other and the dynamics are purely determined by the flux–flow, i.e. a dense chain of fluxons moving unidirectionally through the junction.

As an example of the Fiske regime the simulated current voltage characteristic of a single long junction is shown in Fig. 2.6. The Fiske step positions (i.e. asymptotic voltages V_n^{FS}) are determined by the cavity

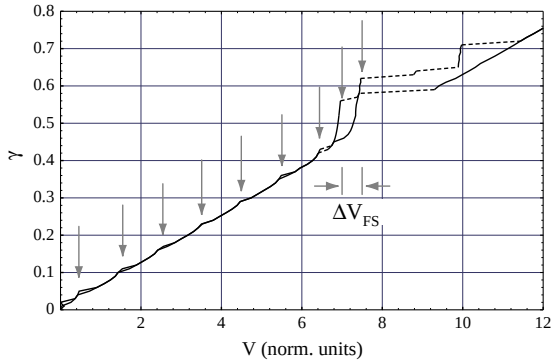

Figure 2.6: Simulated normalized current voltage characteristic of a long linear junction in the Fiske regime. Arrows indicate Fiske resonances.

modes of the junction

$$V_n^{FS} = \frac{n}{2}\Phi_0 \frac{c_0}{L} \ , \tag{2.23}$$

where $n = 1, 2, 3 \ldots$ is the index of the step. As in comparison to ZFSs the Fiske steps have a twice smaller spacing ΔV^{FS}. This can be easily understood by considering resonant modes of a cavity, the frequencies of which are given by the standard formula

$$\nu = n \frac{c_0}{2L} \ . \tag{2.24}$$

Using this equation and the ac Josephson equation, where $d\phi/dt = 2\pi\nu$ one immediately finds Eq. (2.23) for the asymptotic Fiske step voltages. The index of the most pronounced cavity resonances depends on the value of the applied external field H. In general, the higher H, the more stable are Fiske steps with larger index n. Experimentally Fiske steps can be observed easily. A convenient representation of Fiske modes in a long junction is recording a superposition of Fiske steps acquired at various values of the externally applied magnetic fields. An example of such a superposition of FSs is shown in Fig. 2.7. Using Eq. (2.23),

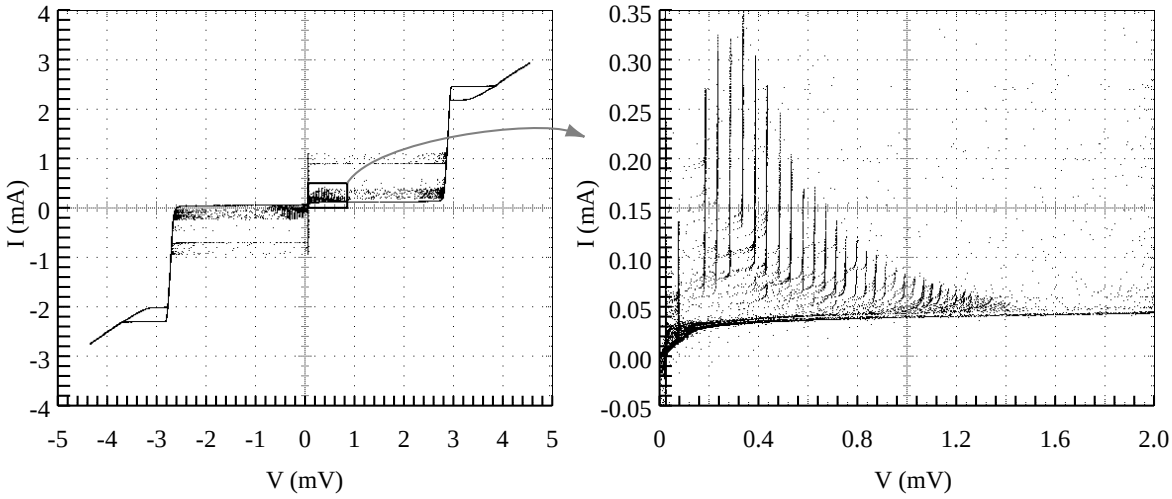

Figure 2.7: Storage oscilloscope traces of superimposed Fiske steps for a $L = 200\ \mu\mathrm{m}$ linear junction at various values of the externally applied magnetic field.

the propagation velocity of fluxons and related electrical properties [see Eq. (2.10)] can be determined from the Fiske step spacing.

At high magnetic fields a flux–flow step can be observed. Its limiting voltage can be tuned continuously by the magnetic field

$$V_{FFS} = H c_0 d' \ , \tag{2.25}$$

where d' is the magnetic thickness of the junction. In Fig. 2.7 the pure flux–flow regime is not observed, because the damping α of the plasma waves is too small in comparison to the normalized length $\ell = L/\lambda_J$ of the junction. A commonly quoted threshold for the existence of a flux–flow step is $\alpha\ell > 1$ [NEIY83, NEYI84, NEYI85].

A more detailed discussion of the different dynamical regimes can be found in the vast literature on long junctions. A good set of references on single junction dynamics is provided in the introduction of the review [PU95] and in [Par93].

2.3 Stacked long Josephson junctions

The theoretical model describing the dynamics of N–fold stacks of magnetically coupled long Josephson junctions was developed by Sakai, Bodin and Pedersen (SBP–model) [SBP93]. In the present work I apply their model to twofold stacks and extend it including the case of LJJ's with arbitrary parameters.

2.3.1 Geometry

In Josephson junction stacks individual junctions are integrated vertically on top of one another. In Figure 2.8 a twofold stack is shown. As in the case of single junctions the overlap geometry was used. The planar dimensions for both systems are comparable (see Sec. 2.1.1). As can be seen in Fig. 2.8 the Joseph-

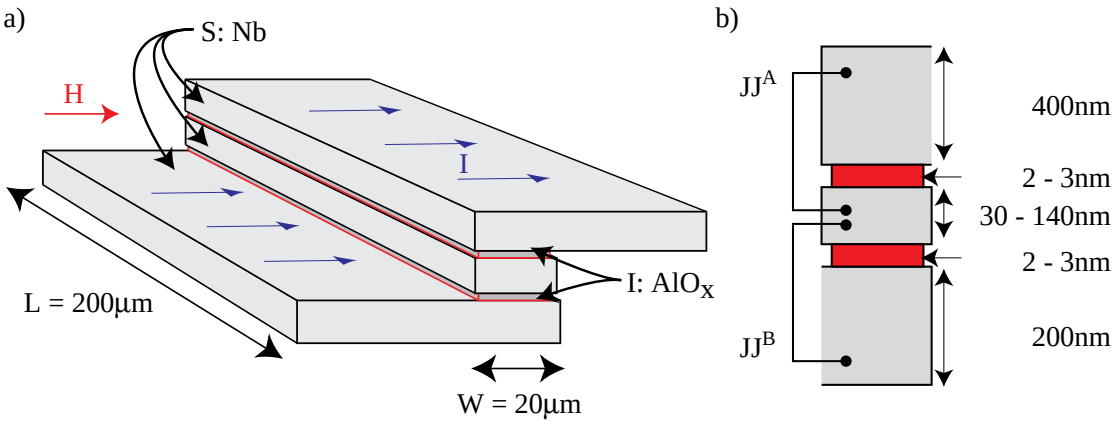

Figure 2.8: Geometry of a twofold stack. a) Typical planar dimensions. b) Typical layer thicknesses.

son junctions A and B share the common middle electrode of the stack. Through this middle electrode the Josephson junctions can interact and its thickness crucially determines the strength of the coupling between the junctions (see Sec. 2.3.2). Usually the top and bottom electrodes are by a number of times larger than the London penetration depth λ_L of the superconductor, whereas the middle electrode is of the order of λ_L or thinner. Again, a brief review of the fabrication technique can be found in Appendix A.

2.3.2 Sakai–Bodin–Pedersen model

Let us consider a twofold stack of Josephson junctions. The superconducting layers (S) are indexed from bottom to top by $i = 0, 1, 2$. For convenience two "ghost" S layers are introduced at the bottom ($i = -1$) and at the top ($i = 3$). The thickness of each S layer is denoted by t_i and its London penetration depth by λ_i. The thickness of each barrier between S layers i and $i-1$ is denoted by $d_{i,i-1}$ (see Fig. 2.9a and b). The orientation of the coordinate system can be inferred from Fig. 2.9, where the x–axes corresponds to the longer dimension of the junctions. The aim is now to find the wave equation for the phase differences $\phi_{0,1}$ and $\phi_{1,2}$ across the two junctions between the S layers $i = 0$, $i = 1$ and $i = 1$, $i = 2$ in the magnetically coupled stack. In the first part of the derivation the "ghost" layers will be considered as part of the stack for simplification, after which they will be abandoned in the second part.

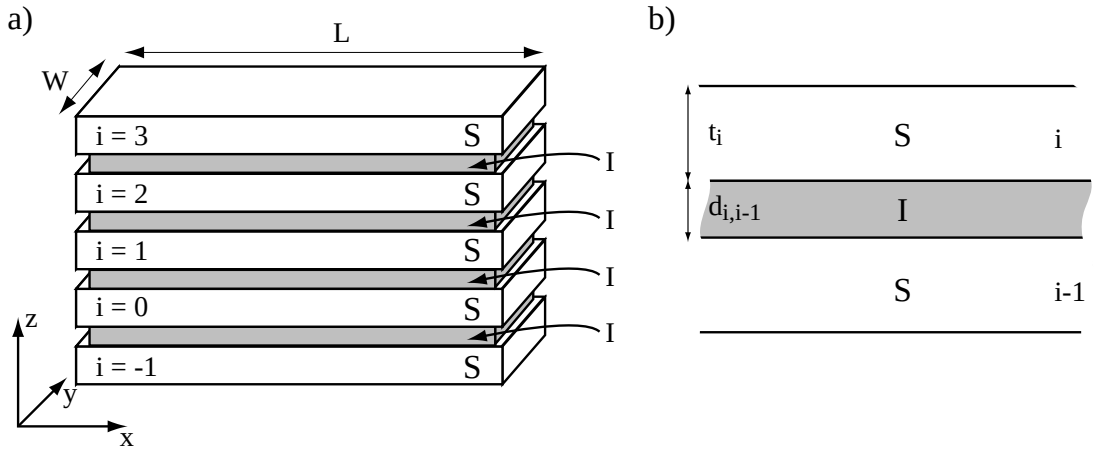

Figure 2.9: a) Sequence of superconducting (S) and isolating (I) layers in a stacked Josephson junction, including top and bottom "ghost" layers to simplify derivation. b) The layer thicknesses.

Derivation

Let us find the equation determining the phase difference $\phi_{i,i-1}$ between any two neighboring S layers along the x dimension. The gauge invariant phase difference is given by

$$\phi_{i,i-1}(x) = \theta_i - \theta_{i-1} + \frac{2e}{\hbar}\int \vec{A}_{i,i-1} d\vec{l}\,, \tag{2.26}$$

where θ_i is the superconducting phase in the i^{th} S layer. The phase difference is related to the vector potential $\vec{A}_{i,i-1}$, which determines the flux enclosed between two layers:

$$\Phi = \int B_{i,i-1} dS = \oint \vec{A}_{i,i-1} d\vec{l}\,. \tag{2.27}$$

Moreover the currents at the upper (U) or lower (L) surface of an S layer are determined by the gradient of the phase $\nabla\theta_i$ and the vector potential $\vec{A}_{i,i-1}$

$$j_i^{L,U} = -\frac{1}{2e\mu_0\lambda_i^2}\left(\nabla\theta_i + 2e\vec{A}_{i,i-1}\right). \tag{2.28}$$

Now the spatial variation of $\phi_{i,i-1}$ can be found by differentiation of Eq. (2.26) with respect to x and inserting (2.28) solved for the phase gradient and (2.27) for the magnetic flux density:

$$\partial_x\phi_{i,i-1} = \frac{2e}{\hbar} d_{i,i-1} B_{i,i-1} - \frac{2e\mu_0\lambda_i^2}{\hbar} j_i^L + \frac{2e\mu_0\lambda_{i-1}^2}{\hbar} j_{i-1}^U\,. \tag{2.29}$$

In a second step one can explicitly calculate the surface currents $j_i^{U,L}$ by taking into account the penetration of the magnetic field into the i^{th} S layer. One has to solve

$$\partial_{zz} B = \frac{1}{\lambda_J^2} B \tag{2.30}$$

together with the boundary conditions $B_{i,i-1}, B_{i+1,1}$ (see Fig. 2.10a). Together with the London–equation

$$\nabla \times \vec{H} = \vec{j} \tag{2.31}$$

the currents are found to be:

$$j_i^L = \frac{1}{\mu_0\lambda_i}\frac{B_{i,i-1}\cosh\left(\frac{t_i}{\lambda_i}\right) - B_{i+1,i}}{\sinh\left(\frac{t_i}{\lambda_i}\right)}\,, \tag{2.32}$$

$$j_i^U = \frac{1}{\mu_0\lambda_i}\frac{B_{i+1,i}\cosh\left(\frac{t_i}{\lambda_i}\right) - B_{i,i-1}}{\sinh\left(\frac{t_i}{\lambda_i}\right)}\,. \tag{2.33}$$

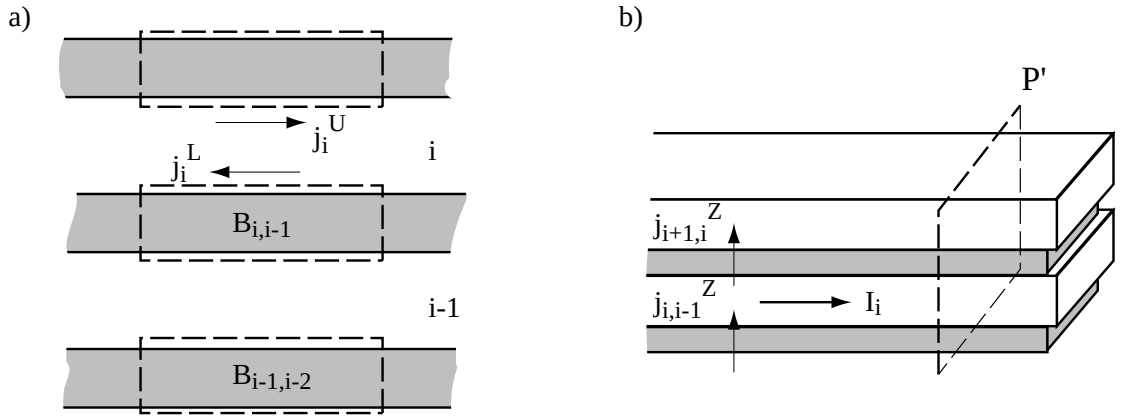

Figure 2.10: a) Magnetic induction in the isolating layers. b) Integration path for Eq. (2.38) and relation between tunnel currents and in–layer currents [see Eq. (2.41)]

Thus Eq. (2.29) can be expressed as follows by inserting the equations for the surface currents:

$$-\frac{\hbar}{2e}\partial_x\phi_{i,i-1} = d'_{i,i-1}B_{i,i-1} + s_i B_{i+1,i} + s_{i-1}B_{i-1,i-2} \ , \tag{2.34}$$

where we defined two new constants, the effective magnetic thickness

$$d'_{i,i-1} = d_{i,i-1} + \lambda_i \coth\left(\frac{t_i}{\lambda_i}\right) + \lambda_{i-1}\coth\left(\frac{t_{i-1}}{\lambda_{i-1}}\right) \ , \tag{2.35}$$

and a parameter describing the coupling

$$s_i = -\frac{\lambda_i}{\sinh\left(\frac{t_i}{\lambda_i}\right)} \ . \tag{2.36}$$

From Eq. (2.34) one can infer that the gradient of the phase difference in the $(i, i-1)$ junction is determined by the flux enclosed in the junction itself and in the neighboring junctions, which is the physical origin for the coupling. Obviously [Eq. (2.36)] the strength of the coupling is determined by the ratio of the S layer thickness to its London penetration depth, such that thinner layers lead to stronger coupling.

Equation (2.34) can be written in matrix form for the twofold stack

$$-\frac{\hbar}{2e}\partial_x\begin{pmatrix}\phi_{1,0}\\ \phi_{2,1}\end{pmatrix} = \begin{pmatrix} s_0 & d'_{1,0} & s_1 & 0\\ 0 & s_1 & d'_{2,1} & s_2\end{pmatrix}\begin{pmatrix} B_{0,-1}\\ B_{1,0}\\ B_{2,1}\\ B_{3,2}\end{pmatrix} \ , \tag{2.37}$$

where $B_{0,-1}$ and $B_{3,2}$ are the magnetic fields external to the stack which for a homogeneous applied field are given by $B_{0,-1} = B_{3,2} = B_{ext}$.

By considering $\nabla \times \vec{H} = \vec{j}$ for the path P' in Fig. 2.10b we can express the flux densities by the currents and the external fields giving rise to them

$$B_{i,i-1} = \frac{\mu_0}{W}\sum_{k=i}^{N} I_k + B_{ext} \ . \tag{2.38}$$

Using Eq. (2.38) we may rewrite Eq. (2.37) as

$$-\frac{\hbar}{2e}\partial_x\begin{pmatrix}\phi_{0,1}\\ \phi_{1,2}\end{pmatrix} = \begin{pmatrix} d'_{1,0} & d'_{1,0}+s_1\\ s_1 & d'_{2,1}+s_1\end{pmatrix}\begin{pmatrix} I_1\\ I_2\end{pmatrix} + B_{ext}\begin{pmatrix} d'_{1,0}+s_0+s_1\\ d'_{1,0}+s_1+s_2\end{pmatrix} \tag{2.39}$$

The next important step is to introduce the tunnel currents across the layers, which have already been discussed in Sec. 2.1.2 in a similar approach

$$\begin{aligned} j^z_{1,0} &= \frac{\hbar}{2e}C^*_{1,0}\partial_{tt}\phi_{1,0} + \frac{\hbar}{2e}\sigma_{1,0}\partial_t\phi_{1,0} + j_{c1,0}\sin\phi_{1,0}\,, \\ j^z_{2,1} &= \frac{\hbar}{2e}C^*_{2,1}\partial_{tt}\phi_{2,1} + \frac{\hbar}{2e}\sigma_{2,1}\partial_t\phi_{2,1} + j_{c2,1}\sin\phi_{2,1}\,. \end{aligned} \tag{2.40}$$

At this point it is also possible to include a uniform current density j_{ext} into Eqs. (2.40) which models the bias current in overlap type junctions.

The change of the current I_i in x direction is given by the difference in the tunnel current densities in z direction as can be inferred from Fig. 2.10b.

$$\begin{aligned} -\frac{1}{W}\partial_x I_i &= j^z_{i,i-1} - j^z_{i+1,i}\,\text{for (i = 1)}\,, \\ -\frac{1}{W}\partial_x I_i &= j^z_{i,i-1}\text{for (i = 2)}\,. \end{aligned} \tag{2.41}$$

Differentiating Eq. (2.39) with respect to x and introducing Eq. (2.41) leads to the general equation of phase for the twofold coupled Josephson stack

$$\frac{\hbar}{2e\mu_0}\partial_{xx}\begin{pmatrix}\phi_{0,1}\\ \phi_{1,2}\end{pmatrix} = \begin{pmatrix} d'_{1,0} & s_1 \\ s_1 & d'_{2,1}\end{pmatrix}\begin{pmatrix} j^z_{1,0}\\ j^z_{2,1}\end{pmatrix}\,. \tag{2.42}$$

Boundary conditions

As one can see the externally applied field vanished from the equations and does only appear in the boundary conditions at $x = 0$ and $x = L$ of the stack.

$$-\frac{\hbar}{2e}\partial_x\begin{pmatrix}\phi_{0,1}\\ \phi_{1,2}\end{pmatrix} = B_{ext}\begin{pmatrix} d'_{1,0}+s_0+s_1\\ d'_{1,0}+s_1+s_2\end{pmatrix} \tag{2.43}$$

Standard form

For the system of two coupled long Josephson junctions the matrix representation of the phases and currents is often dropped in favor of having two separate equations for each junction with a well defined coupling term. Additionally, I will now include the bias current density term as in [SUK+94]

$$\Delta j^z_{i,i-1} = j^z_{i,i-1} + j_{i,i-1_{ext}}\,, \tag{2.44}$$

where $j_{i,i-1_{ext}}$ allows for different bias currents for each junction of the stack. Evaluating

$$\frac{\hbar}{2e\mu_0}\partial_{xx}\begin{pmatrix}\phi_{0,1}\\ \phi_{1,2}\end{pmatrix} = \begin{pmatrix} d'_{1,0} & s_1 \\ s_1 & d'_{2,1}\end{pmatrix}\begin{pmatrix} \Delta j^z_{1,0}\\ \Delta j^z_{2,1}\end{pmatrix} \tag{2.45}$$

we can write down the phase difference equations as

$$\begin{aligned} \frac{\hbar}{2e\mu_0}\partial_{xx}\phi_{1,0} &= \left(d'_{1,0} - \frac{s_1^2}{d'_{2,1}}\right)\Delta j^z_{1,0} + \frac{s_1}{d'_{2,1}}\frac{\hbar}{2e\mu_0}\partial_{xx}\phi_{2,1} \\ \frac{\hbar}{2e\mu_0}\partial_{xx}\phi_{2,1} &= \left(d'_{2,1} - \frac{s_1^2}{d'_{1,0}}\right)\Delta j^z_{2,1} + \frac{s_1}{d'_{1,0}}\frac{\hbar}{2e\mu_0}\partial_{xx}\phi_{1,0} \end{aligned} \tag{2.46}$$

In the following the complicated subscript notation used in the derivation of the SBP model is dropped in favor of a shorter one, i.e. denoting the junction $(2,1)$ by (A) and junction $(1,0)$ by (B). The top

electrode will be denoted by the index A, the middle one by m and the bottom one by B. The indices of all quantities are changed accordingly. Using the notations already introduced in Sec. 2.1.2

$$\lambda_J^{A|B} = \sqrt{\frac{\Phi_0}{2\pi}\frac{1}{\mu_0 j_c^{A|B} d'^{A|B}}} \quad , \tag{2.47}$$

$$\omega_p^{A|B} = \sqrt{\frac{2\pi}{\Phi_0}\frac{j_c^{A|B}}{C^{*A|B}}} \quad , \tag{2.48}$$

$$\omega_c^{A|B} = \frac{2\pi}{\Phi_0} R^{*A|B} j_c^{A|B} \quad \left(\text{where } \mathrm{R^{*A|B}} = \frac{1}{\sigma^{\mathrm{A|B}}}\right) \quad , \tag{2.49}$$

the system of partial differential equations (PDE's) describing the dynamics of the stack is

$$\begin{array}{rcl} \frac{1}{1-S^2}\lambda_J^{A\,2}\phi^A_{xx} = & \sin\phi^A + \frac{1}{\omega_p^{A\,2}}\phi^A_{tt} + \frac{1}{\omega_c^A}\phi^A_t - & \frac{j^A_{ext}}{j^A_c} + \frac{S}{j^A_c(1-S^2)\sqrt{d'^A d'^B}}\frac{\Phi_0}{2\pi}\phi^B_{xx} \\ \frac{1}{1-S^2}\lambda_J^{B\,2}\phi^B_{xx} = & \sin\phi^B + \frac{1}{\omega_p^{B\,2}}\phi^B_{tt} + \frac{1}{\omega_c^B}\phi^B_t - & \frac{j^B_{ext}}{j^B_c} + \frac{S}{j^B_c(1-S^2)\sqrt{d'^A d'^B}}\frac{\Phi_0}{2\pi}\phi^A_{xx} \end{array} \quad , \tag{2.50}$$

where we introduced the dimensionless coupling parameter S $(-1 < S < 0)$ as

$$S = \frac{s_m}{\sqrt{d'^A d'^B}} = -\sqrt{\frac{\sinh\frac{t^A}{\lambda}}{\sinh\frac{t^A+t^m}{\lambda}}\frac{\sinh\frac{t^B}{\lambda}}{\sinh\frac{t^B+t^m}{\lambda}}} \quad . \tag{2.51}$$

In the expression for the magnetic thicknesses $d'^{A|B}$ of the corresponding Josephson junction I dropped the thickness of the insulator, due to its usually negligible contribution to the total value in low T_c applications:

$$d'^{A|B} = \lambda\left(\coth\frac{t^{A|B}}{\lambda} + \coth\frac{t^m}{\lambda}\right) \quad . \tag{2.52}$$

Each equation in the above system of PDE's resembles the usual sine–Gordon equation but includes an additional coupling term proportional to the second derivative of the phase in the neighboring junction. The spatial coordinate x and time t in the Eqs. (2.50) are given in conventional physical units.

2.3.3 Normalized equations

For the sake of simplicity we rewrite the primary system of PDE's (2.50) in dimensionless form normalizing all quantities to the parameters of junction A. Assuming that the spatial coordinate x is normalized by the Josephson penetration depth λ_J^A and time t is normalized by the inverse plasma frequency $1/\omega_p^A$ we can rewrite the set of equations (2.50) in the form

$$\begin{array}{rcl} \frac{1}{1-S^2}\phi^A_{\tilde{x}\tilde{x}} = & \sin\phi^A + & \phi^A_{\tilde{t}\tilde{t}} + \alpha^A\phi^A_{\tilde{t}} - \gamma + \sqrt{\frac{d'^A}{d'^B}}\frac{S}{1-S^2}\phi^B_{\tilde{x}\tilde{x}} \\ \frac{j_c^A}{j_c^B}\frac{d'^A}{d'^B}\frac{1}{1-S^2}\phi^B_{\tilde{x}\tilde{x}} = & \sin\phi^B + & \frac{j_c^A}{j_c^B}\frac{C^B}{C^A}\phi^B_{\tilde{t}\tilde{t}} + \frac{j_c^A}{j_c^B}\frac{R^A}{R^B}\alpha^A\phi^B_{\tilde{t}} - \frac{j_c^A}{j_c^B}\gamma + \frac{j_c^A}{j_c^B}\sqrt{\frac{d'^A}{d'^B}}\frac{S}{1-S^2}\phi^A_{\tilde{x}\tilde{x}} \end{array} \quad . \tag{2.53}$$

Here I introduced the new variables

$$\tilde{t} = \omega_p^A t, \quad \tilde{x} = x/\lambda_J^A, \quad \gamma = \frac{j_{ext}}{j_c^A}, \tag{2.54}$$

$$\alpha^{A|B} = \frac{\omega_p^{A|B}}{\omega_c^{A|B}} = \frac{1}{\sqrt{\beta_c^{A|B}}} = \frac{1}{R_N^{A|B}\sqrt{\frac{2\pi}{\Phi_0} j_c^{A|B} C^{A|B}}} \quad , \tag{2.55}$$

as discussed before in Sec. 2.1.3.

The coupled system of partial differential equations given in (2.53) is subsequently used to model the dynamics of fluxons in twofold stacked systems numerically (chapter 3) as well as analytically (chapter 4).

2.3.4 Boundary conditions

The normalized boundary conditions in the case of annular geometry can be written as

$$\begin{cases} \phi^{A|B}\Big|_{\tilde{x}=0} = \phi^{A|B}\Big|_{\tilde{x}=\ell} - 2\pi N^{A|B} \\ \phi^{A|B}_{\tilde{x}}\Big|_{\tilde{x}=0} = \phi^{A|B}_{\tilde{x}}\Big|_{\tilde{x}=\ell} \end{cases} , \tag{2.56}$$

where $\ell = L/\lambda_J^A$ with L being the junction length (circumference) and $N^{A|B}$ the number of fluxons enclosed in each junction.

For linear geometry the boundary conditions in non–normalized units can be found from Eq. (2.43)

$$\begin{cases} \phi^A_x\Big|_{x=0,L} = \frac{2\pi}{\Phi_0} H \Lambda^A \\ \phi^B_x\Big|_{x=0,L} = \frac{2\pi}{\Phi_0} H \Lambda^B \end{cases} , \tag{2.57}$$

where we introduced the new variable

$$\Lambda^{A|B} = \lambda \left(\tanh \frac{t^m}{2\lambda} + \tanh \frac{t^{A|B}}{2\lambda} \right) . \tag{2.58}$$

Normalizing the boundary conditions with respect to λ_J^A we can express Eq. (2.57) as

$$\begin{cases} \phi^A_{\tilde{x}}\Big|_{\tilde{x}=0,\ell} = \tilde{H} \\ \phi^B_{\tilde{x}}\Big|_{\tilde{x}=0,\ell} = \frac{\Lambda^B}{\Lambda^A} \tilde{H} \end{cases} , \tag{2.59}$$

where we introduced the normalized magnetic field

$$\tilde{H} = \frac{2\pi}{\Phi_0} \Lambda^A \lambda_J^A H = \frac{2H}{H_{c1}^A} . \tag{2.60}$$

The applied magnetic field is expressed in terms of the first critical field of the single uncoupled junction A:

$$H_{c1}^A = \frac{\Phi_0}{\pi \Lambda^A \lambda_J^A} = \sqrt{\frac{2\Phi_0 j_c^A}{\pi \lambda \mu_0}} \frac{\sqrt{\coth \frac{t^m}{\lambda} + \coth \frac{t^A}{\lambda}}}{\tanh \frac{t^m}{2\lambda} + \tanh \frac{t^A}{2\lambda}} . \tag{2.61}$$

The first critical field of a long Josephson junction is defined by the minimum magnetic field at which flux can penetrate into the junction from its boundary. A more detailed discussion of the field penetration into a twofold stack made of junctions with arbitrary parameters can be found in [GGU96].

2.4 Fluxon motion in twofold Josephson stacks

Having applied the SBP model to the twofold stack of arbitrary parameters, it is now possible to accurately model fluxon motion in this system, and hence get a better understanding of the complex dynamics. In this section I will point out some key features of stacked systems, which are relevant for understanding the treatments in later chapters, by discussing some results of numerical simulations carried out in this work. For a detailed review on fluxon dynamics in stacks I refer to [PU95] and the references therein, which cover theoretical aspects, numerical simulations as well as experimental measurements.

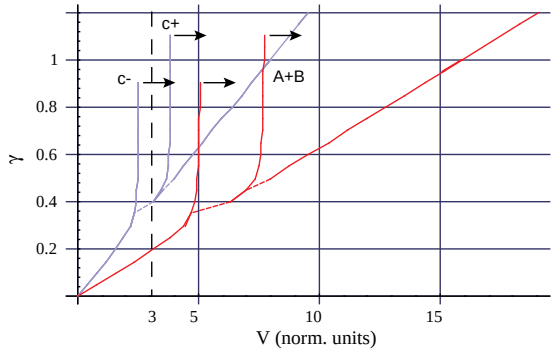

Figure 2.11: Simulated IV curve of an annular stack with 3 fluxons enclosed in each junction. Light curves correspond to the coinciding voltages across single junctions A and B, the dark curve corresponds to the summed voltage of both junctions.

2.4.1 Annular twofold stack

The major consequence of the coupling between two junctions is the appearance of two flux–flow branches in the IV characteristic of an annular stack containing the same number of fluxons in each junction. A numerically calculated example is shown in Fig. 2.11. This effect can be explained by considering small amplitude linear waves in the stack by linearly approximating the sine term in Eq. (2.53). In [Kle94, SUK+94] the linear wave dispersion relation of stacked systems in this regime is calculated and shown to split into m distinct branches, where m is the number of junctions comprising the stack. The splitting of the dispersion relation of the system into two branches is the physical origin for the two steps appearing in Fig. 2.11. The lower voltage mode corresponds to the case when fluxons in two junctions are moving at the low velocity (c_-), whereas the higher voltage branch corresponds to the high velocity (c_+) fluxon motion, i.e. there are two distinct modes at which fluxons can move in the junction. By considering the linear wave approach one can find the limiting velocities of the two modes assuming identical junction parameters

$$c_\pm = \frac{c_0}{\sqrt{1 \pm S}} \,, \tag{2.62}$$

where S ($-1 < S < 0$) is the coupling parameter (2.51) and c_0 is the Swihart velocity (2.10) of a single uncoupled junction. Equation (2.62) is only valid in this simple form if the junctions comprising the stack have identical magnetic thicknesses $d'^{A|B}$ and identical specific capacitances $C^{*A|B}$, i.e. if their Swihart velocities are identical in the uncoupled case. A more general expression for the Swihart velocities of the stack with arbitrary parameters can be found in [GGU96].

Using Eq. (2.21) with the modified Swihart velocities (2.62) one can determine the value of S, for example, from an experimentally acquired, IV curve and compare it to the coupling constant (2.51) calculated from geometrical parameters of the junction. A generally good agreement between these two values of S proves that the model derived in Sec. 2.3 is describing the coupling between two junctions appropriately [SUK+94].

In addition to the different propagation velocities of fluxons in $c_\pm$ modes, one can find further differences by numerically investigating the spatio–temporal distributions of electromagnetic fields in each individual junction of the stack. The magnetic field profiles of the system with the IV curve shown in Fig. 2.11 were acquired for two different bias points on each the lower voltage (Fig. 2.12a and Fig. 2.12c) and the higher voltage branch (Fig. 2.12b and Fig. 2.12d). As one can clearly see the field profile of junction B in the c_- mode is shifted by half a period with respect to the profile of junction A (see Fig. 2.12a,c). Representing fluxons by circulating current loops enclosing single flux quanta, the fluxons form a triangular array, as can be seen in Fig. 2.12e. Because of these features the c_- mode it is subsequently called out–of–phase mode. In contrast, the higher voltage mode is characterized by coinciding field profiles of the junctions (Fig. 2.12b and Fig. 2.12d), which therefore is called in–phase mode. In the circulating currents picture this mode can be visualized as in Fig. 2.12f. The experimental proof for the spatial configuration of

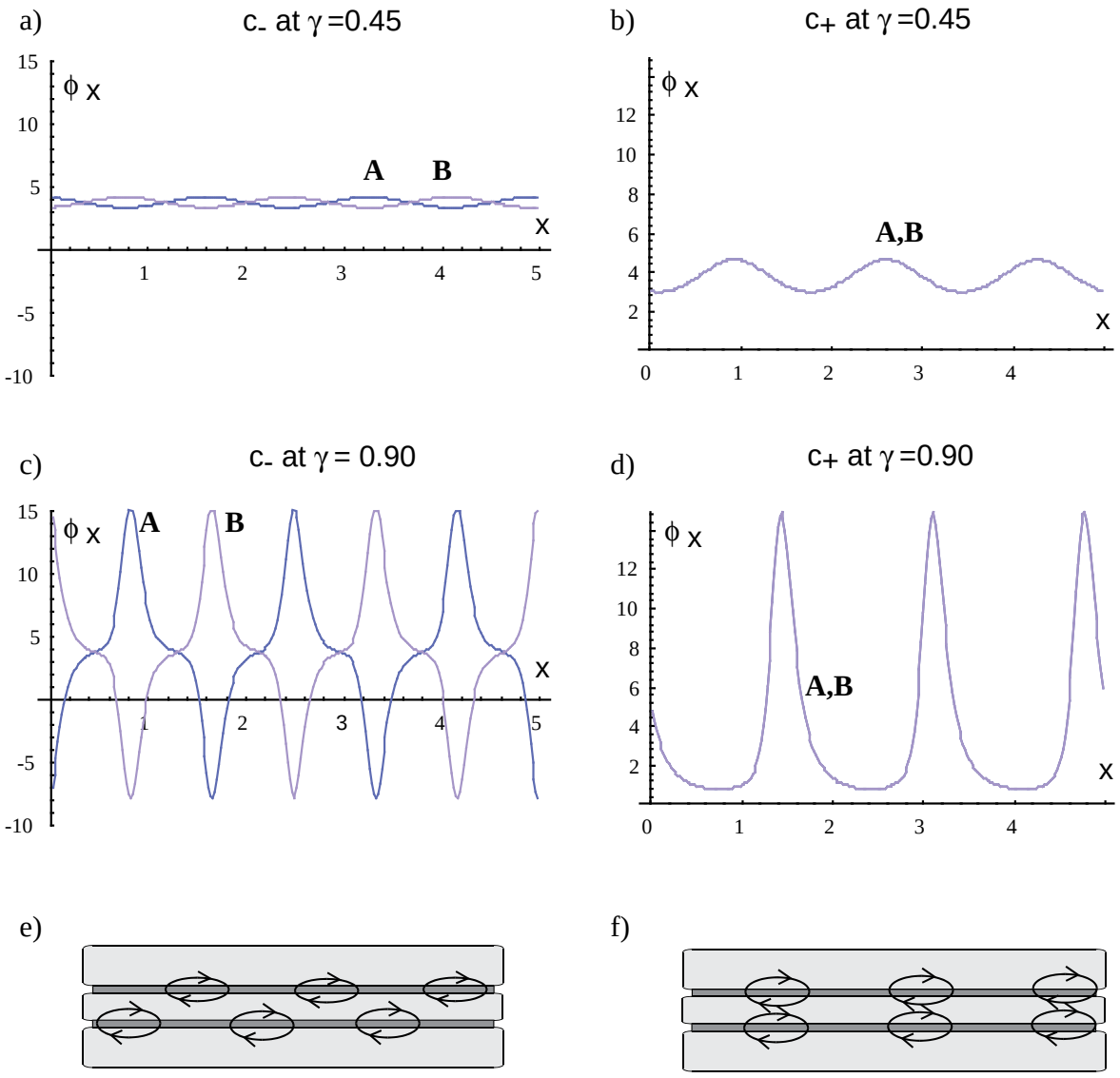

Figure 2.12: Profiles of the magnetic field $\phi_x^{A,B}$, are shown for bias points (see quoted value of γ) for the out–of–phase (a,c) and in–phase (b,d) branches of Fig. 2.11. Additionally fluxon configurations, visualized by circulating currents, are shown (e,f).

fluxons in these modes was accomplished by measurements of the phase-locked Fiske steps [UK96] and radiation measurements [SUIK96], which are discussed in Sec. 3.4.

2.4.2 Linear twofold stack

Because of the identical physical mechanisms linear systems show a behavior similar to annular stacks with respect to the coupling, as discussed before. In analogy the single junction linear modes described in Sec. 2.2.2 are seen as well in linear twofold stacks, but in two different regimes, i.e. at the low velocity c_- and at the high velocity c_+. As an example a simulated IV curve in the Fiske regime is shown in Fig. 2.13. Two different regions with different Fiske step spacings due to the different propagation velocities can be observed:

$$\Delta V_- \propto c_- = \frac{c_0}{\sqrt{1-S}}\,, \tag{2.63}$$

$$\Delta V_+ \propto c_+ = \frac{c_0}{\sqrt{1+S}}\,, \tag{2.64}$$

$$\Delta V_+ \geq \Delta V_-\,. \tag{2.65}$$

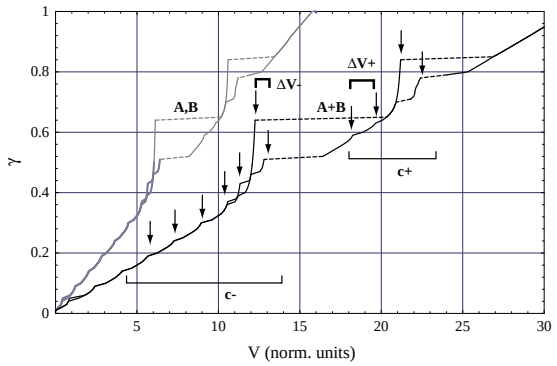

Figure 2.13: Simulated IV characteristic of a long Josephson junction stack showing two distinct sets of Fiske steps corresponding to $c_\pm$ modes; ($l = 5$, $\alpha = 0.1$, $H = 8.8$).

The two Fiske step spacings have also been experimentally observed in linear stacks and gave the first indication of the velocity splitting [UKC$^+$93]. Dc and ac measurements of stacked Josephson junctions are discussed in more detail in Sec. 3.4.

Chapter 3

Analysis of coherent radiation emission by two stacked Josephson flux–flow oscillators

The numerical and experimental investigation of ac oscillations in a system of two magnetically coupled long Josephson junctions is presented in this chapter. The time dependent synchronized voltage response in the flux–flow regime is analyzed for the case of in–phase and out–of–phase oscillations in the junctions, which were introduced in Sec. 2.4.1. A method to experimentally analyze the radiation from a stacked junction is presented and its results [SUIK96] are compared to the numerical predictions. Long Josephson junctions (LJJ's) operated in the flux–flow mode were found to be attractive for applications such as sub–mm wave band tunable local oscillators [KSSF93, KSF$^+$96]. The performance of such an oscillator is limited by the rf power available for pumping a nonlinear detector, e.g. an SIS mixer. It is known to be possible to achieve higher radiation power using an array of coherently operating devices. It had been predicted that the in–phase flux–flow mode multiplies the power of flux–flow oscillators [GJOS93, GJB93] whereas using the out–of–phase mode one can double the main radiation frequency of the oscillator [GKU96]. Both of these effects are systematically studied in simulations. The first three harmonics of ac voltage are investigated for both the in–phase and out–of–phase flux–flow modes and compared with those of a single LJJ. Moreover, the dependence of the ac voltages and its harmonic content on the spread of parameters such as damping and critical current density of the junctions is studied.

The radiated power of the LJJ stack operating in the in–phase single–fluxon mode was investigated theoretically by Grønbech–Jensen and Blackburn [GJB93]. They discussed only the total emitted power, though for oscillator applications it is very important to know its spectral distribution. In addition, the power emitted by the stack was compared in [GJB93] with the power of the single coupled LJJ of the same stack whereas in practice its is more appropriate to compare it with the power of the single uncoupled LJJ with the same parameters. Below I will point out that this difference is crucial. In [GJB93] stacked LJJ's are described by the model identical to the one discussed in Sec.2.3.2, but with the magnetic coupling parameter $S > 0$ ($\Delta > 0$ in the reference). The inversion of the sign of the coupling parameter S [GJB93] with respect to that derived for stacked junctions ($S < 0$), results in the "hyperradiance" – effect, which is physically irrelevant. In this chapter I will discuss enhanced superradiance for in–phase locked LJJ stacks and propose an explanation different from the one of [GJB93].

3.1 Modeling

Experimentally, rf power available from a single long Josephson junction or a stack of these is investigated by coupling the electromagnetic field at the edge of the junction into a microstripline and detecting either on–chip or off–chip (for details see Sec. 3.4). Modeling this experimental procedure I simulated the electromagnetic fields in the stack of Josephson junctions and analyzed its temporal evolution at the edge of the system (see Fig. 3.1). The spectral distribution of the ac oscillations at the edge of the stack was analyzed using Fourier transformation techniques. The junction dynamics are numerically calculated

using the model by Sakai, Bodin and Petersen discussed in Sec. 2.3.2.

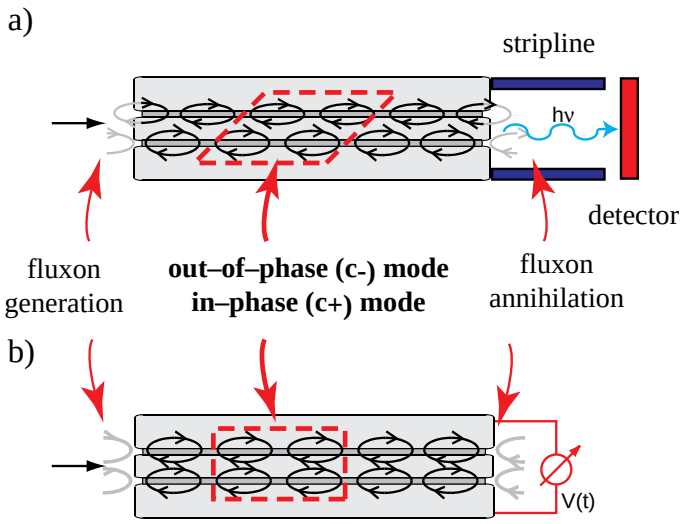

Figure 3.1: (a) In a typical experiment, the radiation from a stack of Josephson junctions is coupled into a microstrip line at the edge of the oscillator. (b) In simulations, the electromagnetic fields are calculated at the edge of the junction.

To simplify the already complex system, any loading effects from the coupling circuits are excluded from the simulations in order to separate features of the stack from those induced by the coupling. Nevertheless in a later stage the analysis could easily be extended in that direction. Loading effects can be simulated by modifying the boundary conditions of the stack as presented in [SCP96], for example.

For a conventional linear LJJ with $\ell\alpha < 1$ the ac voltage at the junction edge is rather complicated due to the superposition of fluxon oscillations with cavity resonances (Fiske steps) of the junction (see Sec. 2.2.2). For very long junctions ($\ell\alpha > 1$) used in non–resonant practical oscillators [KSF$^+$96], only the flux–flow voltage itself is important. In order to save simulation time and simultaneously avoid cavity resonances we carried out most simulations with relatively short junctions ($\ell = 5$) of annular geometry, which intrinsically show flux–flow behavior. An example of a twofold stack of this geometry containing out of phase locked fluxons (represented by circulating currents) is shown in Fig. 3.2.

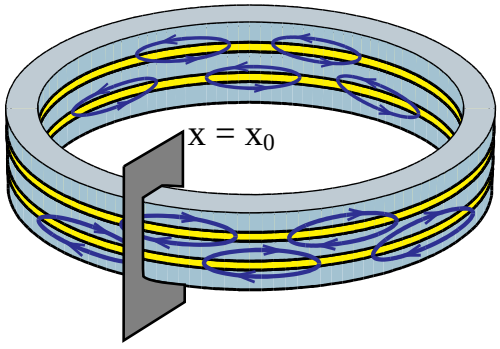

Figure 3.2: In simulations, the time dependent voltage is calculated in an arbitrarily chosen point $x = x_0$ of an annular stacked junction. The sketch shows a twofold stack with fluxons moving out of phase.

To simplify the notation, I rewrote Eqs. (2.53) using the notations $R = R^{*A}/R^{*B}$, $J = j_c^A/j_c^B$, $C = C^{*A}/C^{*B}$ and $D' = \frac{d'^A}{d'^B}$ being the measures of the differences in junction parameters which can be

investigated

$$\begin{array}{rcccccc} \frac{1}{1-S^2}\phi^A_{\tilde{x}\tilde{x}} = & \sin\phi^A + & \phi^A_{\tilde{t}\tilde{t}} + & \alpha^A\phi^A_{\tilde{t}} - & \gamma + & \sqrt{D'}\frac{S}{1-S^2}\phi^B_{\tilde{x}\tilde{x}} \\ D'\frac{1}{1-S^2}\phi^B_{\tilde{x}\tilde{x}} = & \frac{1}{J}\sin\phi^B + & \frac{1}{C}\phi^B_{\tilde{t}\tilde{t}} + & R\alpha^A\phi^B_{\tilde{t}} - & \gamma + & \sqrt{D'}\frac{S}{1-S^2}\phi^A_{\tilde{x}\tilde{x}} \end{array} \quad . \tag{3.1}$$

The influence of the ratio of the quasiparticle resistivities R, which determines the difference in the damping parameters of the individual junctions, on the dynamics of the stack will be investigated in detail. The system will as well be examined with respect to the influence of J, i.e. the ratio of critical currents, which appears in Eq. (3.1) as a scaling factor of the nonlinearity . The influence of C on the system is not considered because it has been experimentally found that the junction capacitances are constant in most cases. Only geometrically identical junctions are considered, such that D' which only depends on geometrical factors is always identical to 1.

3.2 Numerical procedure

First the discretization scheme of the coupled perturbed sine–Gordon system is laid out. Then the method for simulating the dynamics of the stack is explained. Finally I discuss the Fourier transformation technique used to do spectral analysis of the ac oscillations.

3.2.1 Discretization

The set of PDEs (3.1) has to be discretized for numerical solution on a computer.[1] Simple finite difference schemes are employed. The specific methods used to discretize different parts of the equations are pointed out below. The discretization in space and time is done on the grid shown in Fig. 3.3, from which one can extract the indices of steps in time and space.

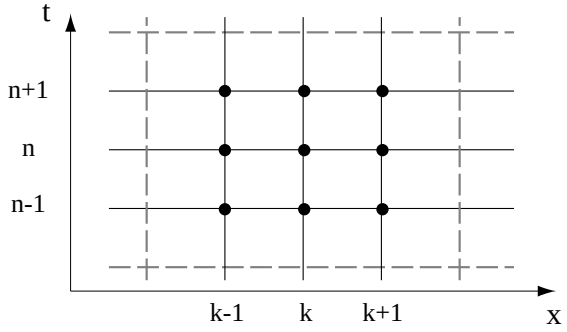

Figure 3.3: Discretized coordinates. n is the index in time and k is the index in space.

The first time derivative is discretized using a simple symmetric three point finite difference method

$$\phi^{i\,(n)}_{\tilde{t}(k)} = \frac{\phi^{i\,(n+1)}_{(k)} - \phi^{i\,(n-1)}_{(k)}}{2\Delta t} \, , \tag{3.2}$$

and the second time derivative using a symmetric four point method

$$\phi^{i\ (n)}_{\tilde{t}\tilde{t}(k)} = \frac{\phi^{i\,(n+1)}_{(k)} - 2\phi^{i\,(n)}_{(k)} + \phi^{i\,(n-1)}_{(k)}}{\Delta t^2} \, . \tag{3.3}$$

The second spatial derivatives are calculated by the following five point finite difference scheme

$$\phi^{i\ (n)}_{\tilde{x}\tilde{x}(k)} = \frac{1}{12\Delta x^2}\left[16\left(\phi^{i\,(n)}_{(k-1)} + \phi^{i\,(n)}_{(k+1)}\right) - 30\phi^{i\,(n)}_{(k)} - \left(\phi^{i\,(n)}_{(k-2)} + \phi^{i\,(n)}_{(k+2)}\right)\right] \, . \tag{3.4}$$

[1] Initially, discretization methods and parts of the algorithmic structure of the original code by P. Bodin [SBP93] were utilized.

Further information on different discretization schemes can be found in [KM90], for example.

Inserting the difference expressions quoted above into the set of PDEs (3.1) and solving for $\phi^{i\,(n+1)}_{(k)}$ yields an expression for the phase in each of the junctions in dependence on phases at earlier time and space coordinates only. Therefore the finite difference equations

$$\begin{aligned}
\phi^{A\,(n+1)}_{(k)} &= \frac{1}{\frac{1}{\Delta t^2}+\frac{\alpha}{2\Delta t}}\left[\frac{1}{1-S^2}\phi^{A\;(n)}_{\bar{x}\bar{x}(k)} - \sqrt{D}\frac{S}{1-S^2}\phi^{B\;(n)}_{\bar{x}\bar{x}(k)} - \sin\left(\phi^{A\,(n)}_{(k)}\right)\right. \\
&\quad \left. + \frac{2}{\Delta t^2}\phi^{A\,(n)}_{(k)} + \left(\frac{\alpha}{2\Delta t} - \frac{1}{\Delta t^2}\right)\phi^{A\,(n-1)}_{(k)} + \gamma\right] \qquad (3.5)\\
\phi^{B\,(n+1)}_{(k)} &= \frac{1}{\frac{1}{C\Delta t^2}+\frac{R\alpha}{2\Delta t}}\left[D\frac{1}{1-S^2}\phi^{B\;(n)}_{\bar{x}\bar{x}(k)} - \sqrt{D}\frac{S}{1-S^2}\phi^{A\;(n)}_{\bar{x}\bar{x}(k)} - \frac{1}{J}\sin\left(\phi^{B\,(n)}_{(k)}\right)\right. \\
&\quad \left. + \frac{2}{C\Delta t^2}\phi^{B\,(n)}_{(k)} + \left(\frac{R\alpha}{2\Delta t} - \frac{1}{C\Delta t^2}\right)\phi^{B\,(n-1)}_{(k)} + \gamma\right] \qquad (3.6)
\end{aligned}$$

derived from Eq. (3.1) are called explicit. If the β–term (see Sec. 2.1.2), which includes mixed spatial and temporal derivatives, was contained in the simulation, an implicit scheme would be needed. Because implicit finite difference methods are much more time consuming to solve on a computer, we considered to neglect the β term.

Discretized boundary conditions

At the boundaries Eqs. (3.5) and (3.6) have to be solved in agreement with the conditions (2.56) or (2.57). Therefore one has to recalculate the finite difference expressions for the spatial derivatives accordingly. Doing this, a discrete linear grid in the range of $[0 \ldots K]$ with $K+1$ steps is assumed, i.e. 0 is the index of the first cell and K the index of the last cell.

Annular boundary conditions. For the annular boundary conditions the values of ϕ have to be corrected with respect to the number of fluxons enclosed in the junction to give a continuous equation for the phase. At the left edge

$$\begin{aligned}
\phi^{i\;(n)}_{\bar{x}\bar{x}(0)} &= \frac{1}{12\Delta x^2}\left[16\left(\phi^{i\,(n)}_{(K)} - 2\pi N + \phi^{i\,(n)}_{(1)}\right) - 30\phi^{i\,(n)}_{(0)} - \left(\phi^{i\,(n)}_{(K-1)} - 2\pi N + \phi^{i\,(n)}_{(2)}\right)\right], \qquad (3.7)\\
\phi^{i\;(n)}_{\bar{x}\bar{x}(1)} &= \frac{1}{12\Delta x^2}\left[16\left(\phi^{i\,(n)}_{(0)} + \phi^{i\,(n)}_{(2)}\right) - 30\phi^{i\,(n)}_{(1)} - \left(\phi^{i\,(n)}_{(K)} - 2\pi N + \phi^{i\,(n)}_{(3)}\right)\right] \qquad (3.8)
\end{aligned}$$

is found and at the right edge:

$$\begin{aligned}
\phi^{i\;(n)}_{\bar{x}\bar{x}(K)} &= \frac{1}{12\Delta x^2}\left[16\left(\phi^{i\,(n)}_{(K-1)} + \phi^{i\,(n)}_{(0)} + 2\pi N\right) - 30\phi^{i\,(K)}_{(0)} - \left(\phi^{i\,(n)}_{(K-2)} + \phi^{i\,(n)}_{(1)} + 2\pi N\right)\right] \qquad (3.9)\\
\phi^{i\;(n)}_{\bar{x}\bar{x}(K-1)} &= \frac{1}{12\Delta x^2}\left[16\left(\phi^{i\,(n)}_{(K-2)} + \phi^{i\,(n)}_{(K)}\right) - 30\phi^{i\,(n)}_{(K-1)} - \left(\phi^{i\,(n)}_{(K-3)} + \phi^{i\,(n)}_{(0)} + 2\pi N\right)\right]. \qquad (3.10)
\end{aligned}$$

Linear boundary conditions In the linear geometry the boundary conditions are simulated by introducing two ghost cells. The values of the phase derivative at the boundaries are determined by the externally applied magnetic field according to Eq. (2.57), which in the finite difference form is given by

$$\phi^{(n)}_{(k+1)} - \phi^{(n)}_{(k)} = \tilde{H}\Delta x\,. \qquad (3.11)$$

Using the three point difference scheme for the second spatial derivative

$$\phi^{i\;(n)}_{\bar{x}\bar{x}(k)} = \frac{\phi^{i\,(n)}_{(k+1)} - 2\phi^{i\,(n)}_{(k)} + \phi^{i\,(n)}_{(k-1)}}{\Delta x^2} \qquad (3.12)$$

we get two expressions for cell 0 and cell K

$$\phi^{i}_{\tilde{x}\tilde{x}\,(0)}{}^{(n)} = \frac{\phi^{i\,(n)}_{(1)} - \phi^{i\,(n)}_{(0)} - \tilde{H}\Delta x}{\Delta x^2} \tag{3.13}$$

$$\phi^{i}_{\tilde{x}\tilde{x}\,(K)}{}^{(n)} = \frac{\tilde{H}\Delta x - \phi^{i\,(n)}_{(K)} + \phi^{i\,(n)}_{(K-1)}}{\Delta x^2}\,, \tag{3.14}$$

where $\Lambda_B/\Lambda_A\tilde{H}$ has to be used for $i = B$ instead of $\tilde{H}$ for $i = A$ in order to take care of the normalization introduced in Sec. 2.3.4.

3.2.2 Numerical stability and simulation technique

Numerical stability of finite difference methods for solving highly nonlinear systems like the perturbed sine–Gordon equation is difficult to determine analytically. Therefore the stability was checked by doubling and dividing in half the spatial and temporal discretization steps $\Delta\tilde{x}$ and $\Delta\tilde{t}$ and checking the influence on the phase distribution (i.e. the fluxon profiles) both in real space and in Fourier space. The possibility to analyze Fourier spectra has proven to be a sensitive tool to check for numerical stability. Stable solutions, independent of the discretization of the system, were achieved for

$$\Delta\tilde{x} = 0.02 \tag{3.15}$$

and

$$\Delta\tilde{t} = \frac{1}{4}\Delta\tilde{x} = 0.005 \tag{3.16}$$

The solutions of the coupled PSGE system are analyzed in the range of $0 \leq \gamma \leq 2$. At $\gamma = 0$ the simulations are started with the initial phase distribution of the static case. Additionally it is possible to provide a wide range of artificially prepared or previously saved initial conditions to force the system into a given state (see appendix D for details on the capabilities of the simulation code). Then in each sequential point of the IV curve the initial conditions are taken from the stationary state achieved in the previous point. Stationary states were reached by subsequently prolonging the time interval over which the voltage was averaged until the difference from the previous interval was less than 0.01 normalized voltage units. In resonant states this limit was always met after less than 100 normalized time units. All dc voltages are calculated in normalized units by spatially and temporally averaging the phase differences according to

$$V = \langle \partial\phi/\partial t \rangle\,. \tag{3.17}$$

This is simply a normalized form of the ac Josephson equation (1.3).

After a stationary state is reached the phase distribution of the system can be extracted to calculate any physical quantities depending on it.

3.2.3 Fourier transforms

Ac voltages are analyzed by simulating the time dependence of the local normalized voltages $V^{A|B}(t) \equiv \phi_t^{A|B}$ at an arbitrarily chosen point $x = x_0$ for annular geometry and at the edge $x = L$ of the stack for linear geometry (see Fig. 3.2 and Fig. 3.1). To perform spectral analysis of the radiated power, the calculated $V(t)$ signal was Fourier transformed using an FFT algorithm. As the time dependent voltage signals simulated are essentially periodic in nature and any source of noise is excluded from the system, their spectra are discrete and each single harmonic displays zero linewidth. Because of this particular feature windowing techniques have to be used in the numerical Fourier analysis. This very important issue is addressed in detail in appendix B, because large errors in amplitudes can occur, if data is Fourier transformed carelessly.

The FFT transforms were performed using 4096 data points acquired at a normalized rate of

$$1/\delta\tilde{t} = 40 \ , \tag{3.18}$$

where $\delta\tilde{t}$ is the time step between subsequently sampled points. This choice provided a maximum normalized Nyquist frequency of

$$\tilde{\nu}_{max} = 20 \ , \tag{3.19}$$

which avoided aliasing effects in the spectra. To enhance the amplitude resolution of the obtained spectra a peak broadening technique with a Gaussian window function was employed (see appendix B). The chosen window function provided a peak amplitude resolution better than 1% and still kept sufficient frequency resolution.

Additionally a small program capable of automatically analyzing the spectra was developed. The program can detect peaks in the spectra using various criteria and extract their frequencies and powers, which simplified the data analysis substantially.

3.2.4 Computational aspects

The compiled C-code performing all necessary computations and the input and output (I/O) of data was tested and run on a variety of computer systems including a Pentium PC, an Apple Macintosh, an HP 9000 712/80, KFA's central IBM PPC cluster and a CRAY supercomputer. For the Fast Fourier Transform a Fortran NAG library routine was used.

The main fraction of computer time was needed to calculated the temporal evolution of the spatially discrete formulae (3.5) and (3.6). Typically 250 steps in space along the length of the junction were calculated. With $\alpha = 0.1$ 40 normalized time units were needed to let the system equilibrate into a stable state after a parameter was changed (typically, the bias current by $\Delta\gamma = 0.05$). Calculation of a typical spectrum required data acquisition for as long as 100 normalized time units. One normalized time unit corresponds to 200 iterations in time being calculated. One time unit required about half a second of calculation time on our HP workstation. During this time the values of Eqs. (3.5) and (3.5) where calculated about $5\ 10^4$ times each. All other computational aspects including FFT, I/O and data manipulation needed a negligible fraction of the total computational power. Most calculations have been conveniently performed in batch mode on our HP workstation dedicated to this project. The larger computer systems were used, when immediate results were required.

3.3 Numerical results

A series of simulations of annular stacks in both in–phase and out–of–phase flux–flow modes were performed. The main interest was to analyze the influence of the parameter spread (such as damping $\alpha^A \neq \alpha^B$ and critical current density $j_c^A \neq j_c^B$) on the in phase and out of phase locking of junctions. In addition, similar runs for single uncoupled LJJ's were carried out for comparison. Results presented here are based on the following set of parameters of the JJ's: the length is $L = 5\lambda_J^A$ ($\ell = 5$), the number of fluxons trapped in each JJ is $N^A = 3$ and $N^B = 3$. In annular stacks the number of fluxons is preserved due to the periodic boundary conditions, whereas, in linear stacks it is determined by the applied magnetic field H. Unless specified different, the coupling parameter was always chosen to be $S = -0.4$, which accounts for a moderate coupling. The damping parameter α^A was set to 0.1. The dynamics of the single uncoupled JJ with parameters being equal to those of JJ^A were simulated by setting $S = 0$. In this case, the coupling term disappears from Eqs. (2.53) and one obtains two independent perturbed sine–Gordon equations.

In Fig. 3.4 the current–voltage characteristics $\gamma(V)$ (IVC's) are shown for a single annular junction and for an annular stack of identical junctions. The asymptotic voltage of the single uncoupled junction (SUJ) shown by the dashed line is determined by $V_0 = N\bar{c}_0 2\pi/L$, where N is the number of fluxons and $\bar{c}_0$ is the Swihart velocity of the junction. In normalized units $\bar{c}_0$ is equal to unity. In the stack with

$S \neq 0$ $\bar{c}_0$ splits into two different velocities, $\bar{c}_+$ and $\bar{c}_-$. One can infer the corresponding limiting voltages of the stack from the IVC (solid line) shown in Fig. 3.4. The lower asymptotic dc voltage of the single coupled junction (SCJ) is given by $V_- = N\bar{c}_- 2\pi/L$. The characteristic propagation velocity in the $\bar{c}_-$ (out–of–phase) mode is [PUPS94, SBP93]:

$$\bar{c}_- = \frac{\bar{c}_0}{\sqrt{1-S}} < \bar{c}_0 \, . \tag{3.20}$$

The asymptotic dc voltage $V_+ = N\bar{c}_+ 2\pi/L$ corresponds to the high velocity $\bar{c}_+$ (in–phase) mode of fluxon motion and is characterized by the limiting velocity [PUPS94, SBP93]:

$$\bar{c}_+ = \frac{\bar{c}_0}{\sqrt{1+S}} > \bar{c}_0 \, . \tag{3.21}$$

The dc voltage across the junction is given by the "0^{th} harmonic" V_0 of the voltage $V(t)$. V_0 is proportional to the fundamental frequency of the fluxon oscillations through the Josephson relation. In the subsequent sections I analyze the harmonic content of these voltage oscillations.

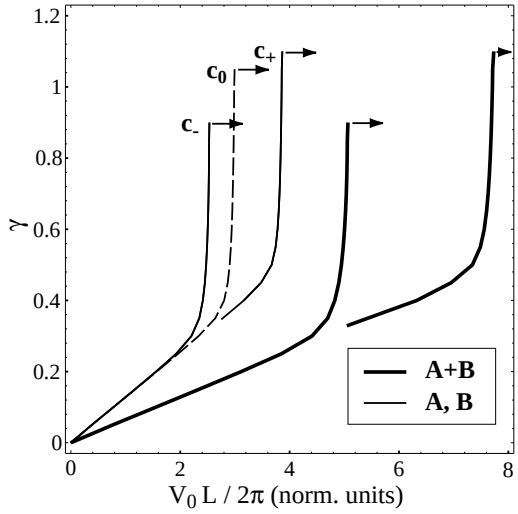

Figure 3.4: I–V characteristics of a single uncoupled junction (dashed line) and a stack of two identical coupled junctions (solid lines). Thick solid lines show the total voltage across the stack $V_0^\Sigma = V_0^A + V_0^B$. (*note: All voltages are multiplied by $L/2\pi$, such that the limiting voltages are proportional to $N/\sqrt{1 \pm S}$.*)

Note on discreteness in γ. *Due to the increased computational power needed to calculate Fourier transforms, the simulations were limited to a discretization step in the bias current of $\Delta\gamma = 0.05$. The γ vs. V points presented subsequently were interpolated linearly to enhance readability of the plots, which therefore have a ragged appearance in a few cases.*

3.3.1 Single uncoupled junction (SUJ)

In this section the characteristics of single junctions are presented in detail in order to facilitate later discussion of stacked junction properties. The simulated dc IV characteristics $V_0(\gamma)$ of the single-layer annular uncoupled LJJ are shown in Fig. 3.5 by the solid line. The vertical part of this IVC, called flux–flow resonance, is due to relativistic behavior of the fluxons that takes place when their velocity u approaches the Swihart velocity $\bar{c}_0$. The asymptotic voltage of the resonance $V = 2\pi N\bar{c}_0/L$ corresponds to $u = \bar{c}_0$. For applications, a working point on the IV curve which guarantees the highest possible radiation power and

narrow linewidth [KSF+96] has to be chosen at the flux–flow resonance, i.e. close to the asymptotic voltage. The spectrum $V(\nu)$ of the ac voltage at the bias point M (see Fig. 3.5) is shown in Fig. 3.6. Since no sources of noise are included in the simulations, the spectrum is discrete and should display zero linewidth for all harmonics. The finite power between the harmonics is a result of the Gaussian window employed here. The maxima of the Gaussian peaks correspond to the harmonic amplitudes (see appendix B for a detailed discussion of windowing techniques). The time dependent voltage signal $V(t)$ is shown as an inset. The amplitudes of all harmonics apparently decrease exponentially with their order k, whereas the dc voltage ($k = 0$) is fixed by the Josephson relation. The exponential decay of the harmonic amplitudes is an intrinsic feature of the solutions to the unperturbed sine–Gordon equation.

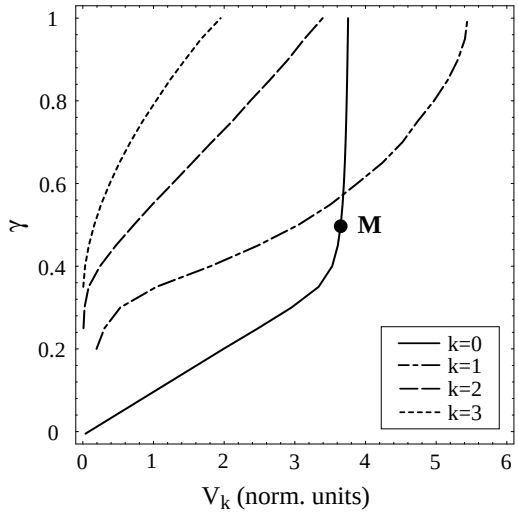

Figure 3.5: Dc voltage V_0 (solid line) and amplitudes of the first three harmonics V_1, V_2 and V_3 (dash–dotted lines) vs. normalized bias current γ for a single uncoupled annular LJJ.

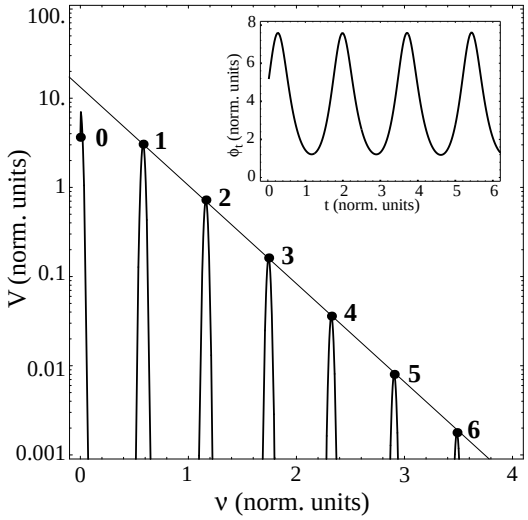

Figure 3.6: The voltage spectrum of the single uncoupled annular LJJ at the bias point M ($\gamma = 0.5$) shown in Fig. 3.5. The integer numbers are indexing the order k of the harmonics. The solid line follows the exponential decay of harmonic amplitudes for $k \geq 1$. In the inset the voltage $V(t)$ at $x = x_0$ is shown.

When moving the working point M (Fig. 3.5) upwards to the top of the resonance, the fluxon voltage

pulses are narrowing due to relativistic Lorentz–contraction. Accordingly, the amplitudes of all harmonics in Fig. 3.6 are increasing. The dependence of the the lowest three harmonic voltage amplitudes V_1, V_2 and V_3 (dash–dotted lines) on γ is shown in Fig. 3.5 . Thus, the curves in Fig. 3.5 account for the IVC's of the first four ($0^{\rm th}$, $1^{\rm st}$, $2^{\rm nd}$ and $3^{\rm rd}$) spectral components of the voltage oscillations in the LJJ. I stress that the spectrum has a high second and third harmonic content near $\gamma = 1$. This is due to the strongly anharmonic voltage oscillations of the fluxons moving close to the limiting velocity. These harmonic amplitudes are reference values for later comparison to amplitudes of the stacked system.

In a recent work V. Koshelets et al. compared their measurements of radiation from a single long Josephson junction operated in flux–flow mode [KSF$^+$97] to our numerical work. They measured the dependence of the emitted power of the first harmonic of the Josephson radiation in dependence on the bias current using a on-chip detection scheme similar to the one discussed in more detail in Sec. 3.4. Good qualitative agreement was found between our numerical predictions and the measurements in [KSF$^+$97].

Influence of the damping parameter. Figure 3.7 shows the dependence of the amplitudes V_0 and V_1 on γ for different values of the damping parameter α. The slope $\Delta I/\Delta U \propto 1/R_N$ of the IVC at low γ is proportional to the damping parameter α as expected. The simulated IVC's for different values of α are in good agreement with the theoretical model by Marcus and Imry [MI80]:

$$\gamma = \frac{4\alpha}{\pi}\frac{E(k)}{k}\frac{1}{\sqrt{1-u^2}} \ , \tag{3.22}$$

where the modulus k of $E(k)$ is given by the equation

$$\xi = \frac{L}{N\lambda_J} = 2kK(k)\sqrt{1-u^2} \ . \tag{3.23}$$

$K(k)$ and $E(k)$ are the complete elliptic integrals of the first and second kind and ξ is the fluxon spacing in the junction. Equation (3.22) was also used to fit experimental data of multi fluxon steps in annular junctions in [UDH$^+$92] and good agreement was found.[2]

The first harmonic amplitude V_1 (Fig. 3.7) decreases with increasing α, as expected. In Fig. 3.8 one can recognize in more detail the dependence of V_1 on α for different fixed values of γ. V_1 decreases linearly with increasing α in a range of γ relatively close to unity. For lower driving currents the dependence is nonlinear. Linear extrapolation of $V_1(\alpha)$ in the range $\alpha < 0.075$ results in a limiting first harmonic amplitude at $V_1 \approx 8$ in the limit of $\alpha \to 0$. This feature is rather important, because it allows us to extrapolate the data simulated for $\alpha \approx 0.1$ to values of $\alpha < 0.01$ that are more relevant for typical experiments.

Influence of the critical current density. To evaluate the influence of spread in critical currents in the coupled system we simulated also the influence of variation in j_c on the ac voltage in SUJ's. This was done by choosing $S = 0$ and $J \neq 1$ in Eqs. (3.1) and analyzing the voltages in JJ^B. Since $j_c^B = j_c^A/J$, the effective critical current in JJ^B differs from JJ^A by a factor of $1/J$. The dc voltage and the first three harmonics are shown in Fig. 3.9. For each value of J the characteristics are plotted up to the current at which the junction switches from the flux–flow resonance to higher voltages (McCumber branch). One observes that this switching current scales with $1/J$ as expected from Eqs. (3.1). Moreover the fluxons move at higher speeds for lower j_c at the same γ. The dependence of the first harmonic amplitude on $1/J$ at different values of driving current is presented in Fig. 3.10. We note that the voltage amplitude only weakly depends on $1/J$ at constant values of driving current $\gamma \geq 0.3$ in the studied range $0.5 < J < 2.0$. At very low bias currents $\gamma \ll 0.3$ (i.e. the static case) the values of first harmonic amplitude obviously scale with J. This can be understood as well from the perturbation calculation presented in Sec. C.1.2 by

[2] Due to an error in Eq. (2) of [UDH$^+$92] the fits presented in Fig. 3a of the reference show some discrepancy between theoretical and experimental data. Using the correct Eqs. (3.22) and (3.23) instead, results in excellent agreement.

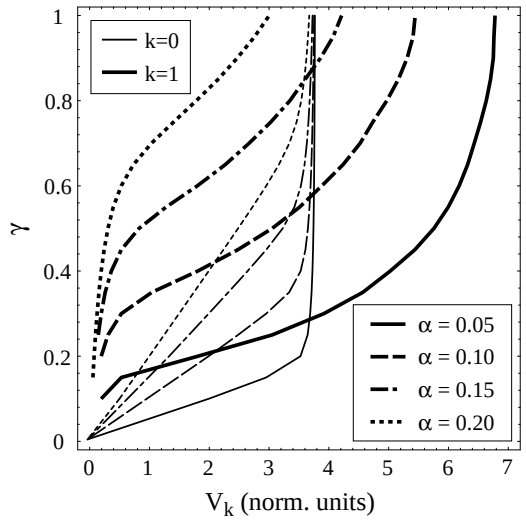

Figure 3.7: Dc voltage V_0 and the first harmonic amplitude V_1 *vs.* bias current γ for a single uncoupled annular LJJ with damping parameters $\alpha = 0.05, 0.10,\ 0.15$ and 0.20.

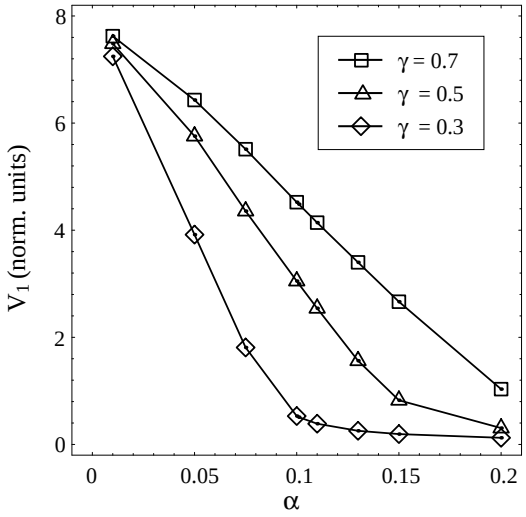

Figure 3.8: The amplitude of the first harmonic V_1 at constant levels of γ *vs.* damping parameter α for a single uncoupled annular LJJ.

considering the case $S = 0$. For large $1/J$ the amplitudes increase with the switching current. In higher harmonics, the junction with lower j_c exhibits larger amplitudes at the same driving current, because the fluxons in this junction reach the limiting velocity at lower normalized driving current, as can be seen from the dc I–V characteristics in Fig. 3.9.

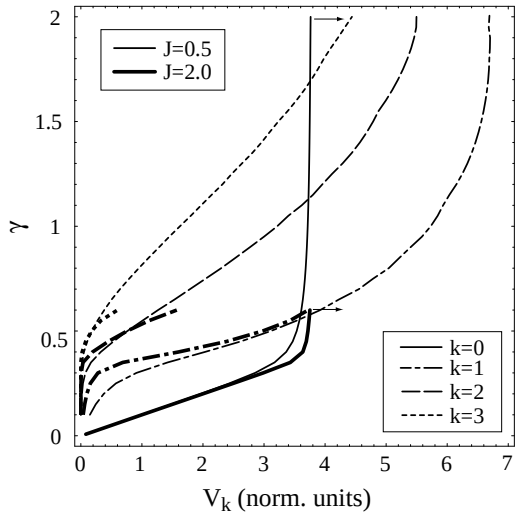

Figure 3.9: The dc voltage V_0 and the first three harmonic amplitudes V_1, V_2 and V_3 *vs.* normalized bias current γ for the single uncoupled annular JJ^B with $\alpha = 0.1$ and critical current parameters $J = j_c^A/j_c^B = 0.50$ and 2.00. Arrows indicate switching to higher voltages.

3.3.2 Out–of–phase mode

The qualitative features of the time dependent dynamics of symmetric stacks for both the in–phase and out–of–phase modes have been investigated earlier in [PUPS94]. Later the idea of doubling the frequency of Josephson radiation using a stacked flux–flow oscillator operating in the out–of–phase mode was proposed [GKU96]. Here the harmonic content of voltage oscillationsn is examined in detail.

In the flux–flow resonance, the voltage oscillations $V^A(t)$ in JJ$^{\mathrm{A}}$ and $V^B(t)$ in JJ$^{\mathrm{B}}$ at an arbitrary point $x = x_0$ of the stack are periodic in time. Thus, $V^A(t)$ and $V^B(t)$ can be expanded into Fourier series:

$$V^A(t) = \sum_{k=0}^{\infty} V_k^A \cos(\omega^A k t + \varphi_k^A) \,, \tag{3.24}$$

$$V^B(t) = \sum_{k=0}^{\infty} V_k^B \cos(\omega^B k t + \varphi_k^B) \,, \tag{3.25}$$

where $V_k^{A|B}$ are the amplitudes and $\varphi_k^{A|B}$ the phases of the k$^{\mathrm{th}}$ harmonics. The fundamental angular Josephson frequencies are given by $\omega^{A|B}$.

If the junctions are frequency locked, their fundamental angular frequencies are identical $\omega^A = \omega^B = \omega$. Accordingly, the sum of the two voltages can be expressed as

$$V^\Sigma(t) = \sum_{k=0}^{\infty} |V_k^\Sigma| \cos(\omega k t + \vartheta_k) \,, \tag{3.26}$$

where

$$|V_k^\Sigma|^2 = {V_k^A}^2 + {V_k^B}^2 + 2 V_k^A V_k^B cos(\Delta\varphi_k) \tag{3.27}$$

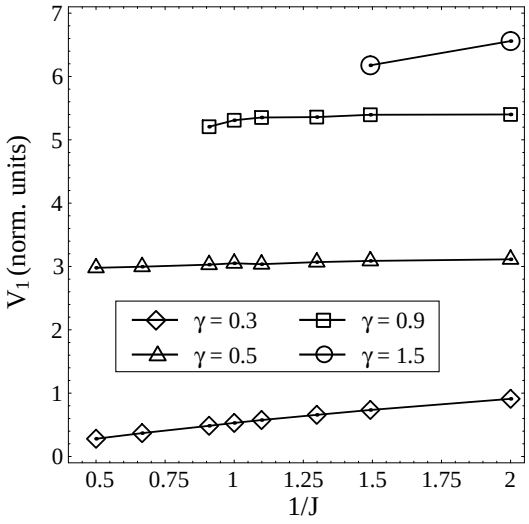

Figure 3.10: The amplitudes of the first harmonic V_1 at constant γ *vs.* $1/J = j_c^B/j_c^A$ for the single uncoupled annular JJ^B ($\alpha = 0.1$).

is the square of the total amplitude of the k$^{\text{th}}$ harmonic, depending on the respective junction harmonic amplitudes V_k^A and V_k^B and their phase difference $\Delta\varphi_k = \varphi_k^B - \varphi_k^A$. The initial phase ϑ_k fixes the phase relation between the harmonics of the total voltage. ϑ_k is not important to determine the harmonic content of the signal, but necessary to reconstruct the waveform.

Identical junction parameters

First, for the sake of simplicity, I assume that the junctions have identical properties so that $V_k^A = V_k^B = V_k$ and $\varphi_k^A = \varphi_k^B = \varphi_k$. In out–of–phase mode the voltage $V^B(t)$ is shifted in time relative to $V^A(t)$ by one half of the fundamental period $T = 2\pi/\omega$:

$$V^A(t) = \sum_{k=0}^{\infty} V_k \cos(\omega k t + \varphi_k) \; , \tag{3.28}$$

$$V^B(t) = \sum_{k=0}^{\infty} V_k \cos[\omega k (t + T/2) + \varphi_k] = \sum_{k=0}^{\infty} V_k \cos(\omega k t + \varphi_k + \pi k) \; . \tag{3.29}$$

With $\Delta\varphi = \pi k$ and Eq. (3.27) the total amplitudes V_k^Σ can be calculated as:

$$|V_k^\Sigma|^2 = {V_k}^2 + {V_k}^2 + 2{V_k}^2 \cos(k\pi) = \begin{cases} 0 & , \quad k = 1, 3, 5, \ldots \\ 4{V_k}^2 & , \quad k = 2, 4, 6, \ldots \end{cases} \; . \tag{3.30}$$

As a result all odd harmonics cancel and the amplitudes of all even harmonics become twice as large as the amplitudes in a *single coupled junction* (SCJ) of the stack. The resulting voltage can be expressed as:

$$V^\Sigma(t) = \sum_{k=0}^{\infty} 2V_{2k} \cos(2\omega k t + \vartheta_k) \; . \tag{3.31}$$

Thus one would expect an enhanced yield at the second harmonic.

In Fig. 3.11 the voltages $V^A(t), V^B(t)$ and $V^\Sigma(t)$ of a stack with equal junction parameters at $\gamma = 0.5$ are plotted versus time. One recognizes, that $V^\Sigma(t)$ is governed by a small amplitude oscillation at twice the fundamental Josephson frequency of the stack. The corresponding spectrum of the stack biased at $\gamma =$

0.7 is shown in Fig. 3.12. We note that all odd harmonics of the total voltage V^{Σ} attain zero amplitudes, in agreement with Eq. (3.30). The amplitudes of all even harmonics are doubled with respect to the SCJ, but they are much smaller than those of the SUJ. The second harmonic amplitudes of a single uncoupled junction (dashed line), a single coupled junction (solid line) and the stack (thick solid line) in dependence on the bias current γ are shown in Fig. 3.13. Apparently, the second harmonic of the SCJ is very much smaller than the second harmonic of the SUJ. This result deserves a more detailed discussion.

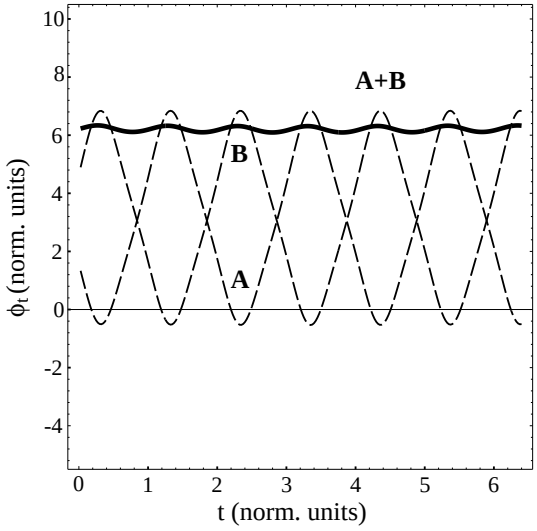

Figure 3.11: The time dependent voltages $V^A(x_0,t), V^B(x_0,t)$ and $V^{\Sigma}(x_0,t)$ at an arbitrarily chosen coordinate x_0 in a stack with equal junction parameters at $\gamma = 0.5$.

Let us compare the spectra shown in Fig. 3.6 and Fig. 3.12 in more detail. It can be noted easily that the odd harmonic amplitudes of the SUJ are smaller than the SCJ ones. In contrast, the even harmonics in the spectrum of the SCJ are considerably suppressed in comparison to the SUJ. This feature is related to the magnetic coupling between the junctions. Qualitatively, the mechanism responsible for this phenomenon is the following. Due to the coupling, the fluxons moving in JJ$^{\mathrm{A}}$, with magnetic field profile $\overline{\phi}_x^A(x)$, create the image profile $\tilde{\phi}_x^A(x)$ in JJ$^{\mathrm{B}}$. An example of such an image for $N^A = 3$ and $N^B = 0$ is shown in Fig. 3.14. We note that the field profiles are almost identical except for the constant component and the inverted polarity of the profile B. Fourier analysis of the profiles in the master and the image junction has shown that the harmonic content (for $k \geq 1$) of the two profiles is almost equivalent for $S = -0.4$ and $\gamma \geq 0.3$. Thus, for coupling constants $|S| \geq 0.4$, in case of $N^B = 0$, we can approximately express the image profile in junction B induced by junction A as

$$\tilde{\phi}_x^A(x) \approx \mathrm{const} - \epsilon \bar{\phi}_x^A(x) \,, \tag{3.32}$$

where ϵ is a constant close to but always less than unity. Now, supposing the existence of fluxons also in JJ$^{\mathrm{B}}$, we obtain in zeroth order approximation

$$\phi_x^B(x) \approx \bar{\phi}_x^B(x) + \tilde{\phi}_x^A(x) \approx \bar{\phi}_x^B(x) - \epsilon \bar{\phi}_x^A(x) + \mathrm{const} \tag{3.33}$$

and a similar expression for $\phi_x^A(x)$. Taking into account the phase difference in the out–of–phase mode $\bar{\phi}_x^B(x) = \bar{\phi}_x^A(x - uT/2)$ and using the Fourier series expansion of $\bar{\phi}_x^A$ one can easily compute the harmonic amplitudes and get expressions similar to Eqs. (3.28)–(3.31). As a result all odd harmonics of $\phi_x^B(x)$ increase by a factor of $1+\epsilon$. In contrast all even harmonics of $\phi_x^B(x)$ obtain very small amplitudes of the order of $1-\epsilon$ in comparison to the SUJ. Due to the fact that $\phi^{A|B}(x,t)$ describes traveling waves with the argument $(kx - ut)$, one obtains $V^{A|B}(t) \propto H^{A|B}(x)$, thus the above treatment is applicable to the time

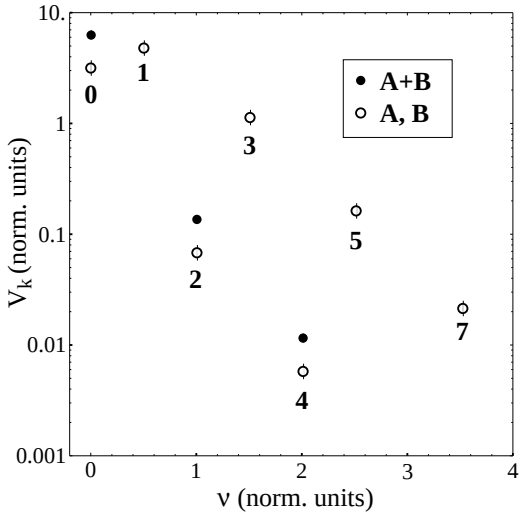

Figure 3.12: Spectrum of the voltage oscillations with harmonic amplitudes shown by open circles ($V_k^{A,B}$) and small solid circles (total voltage V_k^{Σ}) at $\gamma = 0.7$. Numbers indicate the harmonic index k.

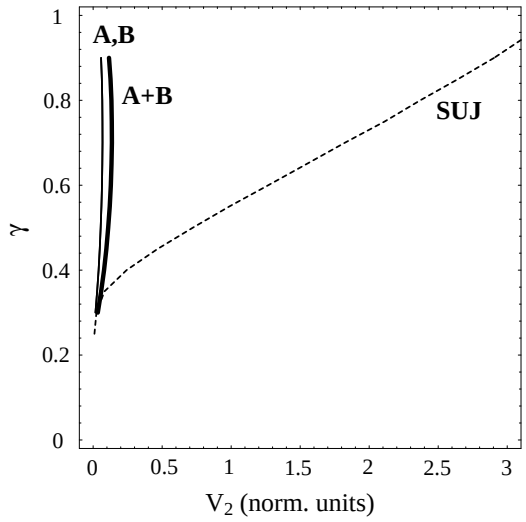

Figure 3.13: The amplitudes of the second harmonic V_2 *vs.* bias current γ of the stack of identical junctions synchronized in out–of–phase mode. The dashed line shows V_2 from Fig. 3.5 of the single uncoupled junction (SUJ) for comparison.

dependent voltages as well. The above considerations do well explain the features of the time dependent voltage signal $V^{\Sigma}(t)$ in Fig. 3.11 and the voltage spectrum $V(\nu)$ presented in Fig. 3.12.

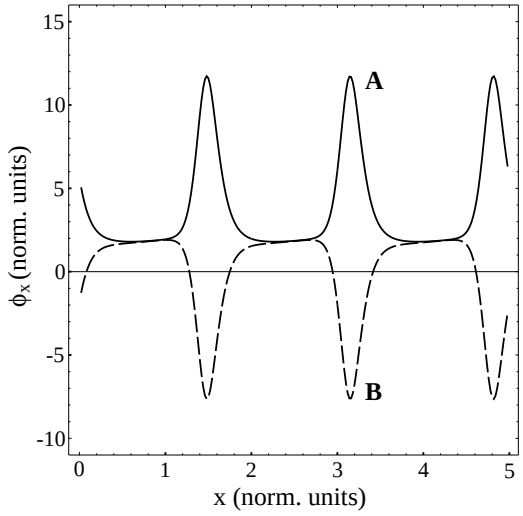

Figure 3.14: Magnetic field profiles of the two junctions in the out-of-phase mode biased at $\gamma = 0.7$. There are three fluxons trapped in JJ^A, JJ^B contains no net flux.

Quantitatively, one would have to solve the self consistent problem for the magnetic field distribution. The analytical expression for the image profiles, derived in [KM88] using the perturbation technique, is proportional to S for $|S| \ll 0.1$. Consequently, all spectral components of the image profiles are proportional S in that range. I have found from numerical simulations of the image profiles that for $|S| \geq 0.2$ all harmonic amplitudes are constrained by $0.9\, V_k^A < V_k^B < V_k^A$ at $\gamma \geq 0.3$. This implies that the factor ϵ introduced above is always larger than 0.9. Therefore, the above considerations are appropriate for all experimentally relevant coupling parameters.

In conclusion one can state that for equal junction parameters all harmonics (except the dc amplitude V_0) of a SCJ in the out–of–phase flux–flow mode are much smaller in amplitude than the corresponding harmonics of a SUJ. For odd harmonics this phenomenon can be explained by the out–of–phase voltage summation and for even harmonics by the out–of–phase magnetic coupling.

Spread in junction parameters

Simulations of stacks with different junction parameters were analyzed in detail. It is important to note that in case of large differences in parameters the mutual phase locking can be difficult or even impossible to achieve. The locking behavior of twofold stacks with a spread in quasiparticle resistances is investigated numerically and theoretically in chapter 4. In simulations one can “artificially” lock the junctions in some parameter range by choosing appropriate initial conditions, which extends the locking range as in comparison to experiment. In experiment, phase locking can be facilitated by using an independent magnetic field control for each junction, as demonstrated in [GKU96].

The main effect observed in simulations of the out–of–phase flux–flow mode for different junction parameters is, that the odd harmonics of the total voltage $V^{\Sigma}(t)$ attain non zero amplitudes. The even harmonic amplitudes become smaller than in the case of equal parameters. This can be explained by considering the general equation (3.27) and allowing different harmonic amplitudes $V_k^{A|B}$ and phases $\varphi_k^{A|B}$. The resulting amplitudes in the out–of–phase mode are then given by:

$$|V_k^{\Sigma}|^2 \quad = \quad {V_k^A}^2 + {V_k^B}^2 + 2V_k^A V_k^B \cos(k\pi + \delta\varphi)$$

$$= \begin{cases} {V_k^A}^2 + {V_k^B}^2 - 2V_k^A V_k^B \cos(\delta\varphi_k) & , \quad k = 1,3,5,\ldots \\ {V_k^A}^2 + {V_k^B}^2 + 2V_k^A V_k^B \cos(\delta\varphi_k) & , \quad k = 2,4,6,\ldots \end{cases} , \tag{3.34}$$

where

$$\delta\varphi_k = \Delta\varphi_k - k\pi \; . \tag{3.35}$$

Thus, the total voltage is determined by the different harmonic amplitudes of $V^{A|B}(t)$ and the phase shifts between them. For identical junctions $\delta\varphi_k$ vanishes.

Spread in damping Simulations of the out–of–phase mode were performed for various $R \neq 1$, i.e. different damping coefficients of the two junctions [see Eq. (3.1)]. The current range at which the phase locking of the junctions takes place is strongly dependent on the ratio of damping parameters of the junctions. A more detailed analysis of this dependence is presented in chapter 4 and in [GWMU96]. The data presented here refer to the phase locked states on the flux–flow resonances.

In general, a spread in damping coefficients leads to an additional decrease of the second harmonic amplitude of the stack. There are two contributions to be considered. First, the fluxon velocity in the coupled system decreases at a given γ, if the damping parameter in JJ^B is increased. This contribution is found to be rather small. Second, additional phase shifts $\Delta\varphi_k$ occur between harmonics of the SCJ's. As an example I discuss the case $R = 1.5$. Figure 3.15 displays V_2^A, V_2^B and V_2^Σ in dependence on γ, the sum of the first harmonics V_1^Σ is shown for comparison. The harmonic amplitudes of each single junction in the stack are identical (see Fig. 3.15). In general, it was found that the SCJ harmonics are almost identical in two junctions for any R examined. Hence, the very small value of V_2^Σ has to be the result of an additional phase shift $\delta\varphi_2$ between V_2^A and V_2^B as given by Eq. (3.35). In the example given in the inset of Fig. 3.15 the phase shift assumes a value $\delta\varphi_2 \geq \pi/2$, such that $V_2^\Sigma \ll V_2^{A,B}$. The phase in the first harmonic $\delta\varphi_1$ is shifted as well. As a result, the first harmonic amplitude is even larger than the second in this case (see Fig. 3.15).

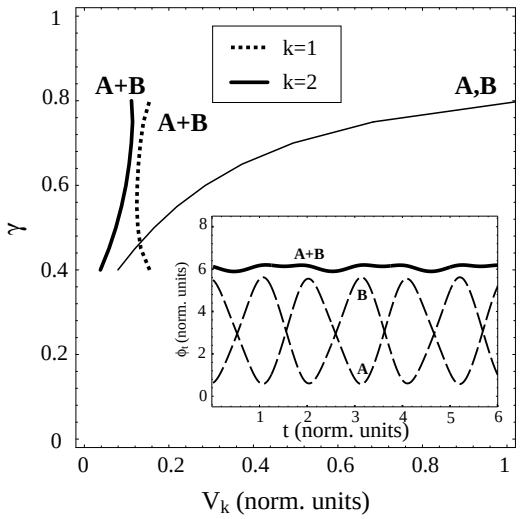

Figure 3.15: Solid lines show V_2^A,V_2^B (thin line) and V_2^Σ (thick line) as a function of γ. V_1^Σ (dotted line) is plotted for reference. The voltage profiles $V^A(x_0,t), V^B(x_0,t)$ and $V^\Sigma(x_0,t)$ at $\gamma = 0.5$ are shown in the inset.

Spread in critical current density The effect of different critical currents of the two junctions on the out–of–phase mode was investigated for $0.5 < J = j_c^A/j_c^B < 2.0$ with the fixed coupling strength $S = -0.4$. The calculations for $J \neq 1$ have shown features similar to the behavior for $R \neq 1$ discussed

above. In Fig. 3.16 the time dependent voltage profiles $V^{A,B}(t)$ and $V^{\Sigma}(t)$ are plotted for $j_c^A = 2j_c^B$. Apparently, the amplitudes of the oscillations in each junction are almost identical at this bias current. The Fourier components at the fundamental frequency V_1^A, V_1^B and V_1^{Σ} are shown in Fig. 3.17. The data are plotted for $J = j_c^A/j_c^B = 1$ and $J = j_c^A/j_c^B = 2$ in dependence on γ. The harmonic amplitudes of the fluxon oscillations in each single junction for $J = 1$ are equal, as expected. We found from simulations that for $J = 2$ and for all other values of J investigated the ratio of the harmonic amplitudes at resonant voltages is almost equal to unity

$$\frac{V_1^A}{V_1^B} \approx 1 \ . \tag{3.36}$$

At low bias currents this ratio agrees with the value expected from the perturbation theory. In Sec. C.1.2 a perturbation calculation of the ratio of the first harmonic amplitudes of a twofold stack is presented in the dense fluxon chain approximation. This calculation was conducted to ascertain the results of the numerical simulations. Indeed, an initial error in the numerical code was detected by comparison of theoretical and numerical results. For details and a discussion see Sec. C.1.2.

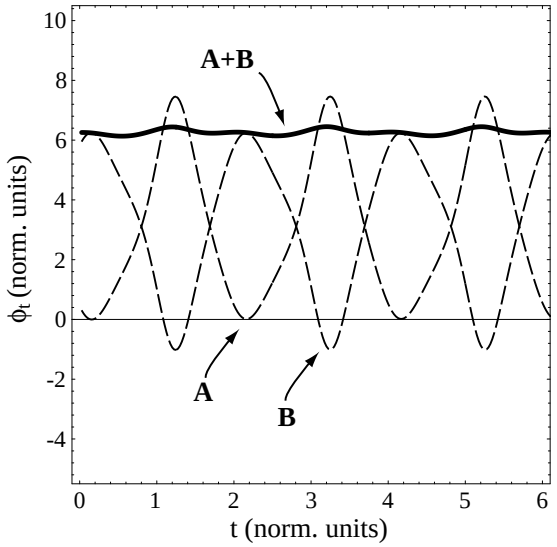

Figure 3.16: The evolution of $V^{A,B}(x_0,t)$ and $V^{\Sigma}(x_0,t)$ in time for $J = j_c^A/j_c^B = 2$ at $\gamma = 0.5$.

In order to discuss Fig. 3.17 in more detail, Eq. (3.34) is considered for $k = 1$. Accordingly, the first harmonic amplitude V_1^{Σ} is given by

$$|V_1^{\Sigma}|^2 = {V_1^A}^2 + {V_1^B}^2 - 2V_1^A V_1^B \cos(\delta\varphi_1) \ . \tag{3.37}$$

Exact out–of–phase addition of the first harmonic of the two junctions $V_1^{\Sigma} = V_1^A - V_1^B$ takes place for $\delta\varphi_1 = 0$. Thus, for junctions with equal critical currents, $V_1^A = V_1^B$ and the sum of the voltages is $V_1^{\Sigma} = 0$ (see Fig. 3.17) . In the case $J \neq 1$, the harmonics V_1^A and V_1^B differ from one another by less than 5 percent. Additionally $\delta\varphi_1$ may attain non zero values. We found that $\delta\varphi_1 \leq 5°$ for $0.5 < J < 2.0$ by solving Eq. (3.37) for $\delta\varphi_1$ and using the simulated values of V_1^A, V_1^B and V_1^{Σ}. Thus, $V_1^{\Sigma} \approx |V_1^A - V_1^B|$ can be applied to all simulated values of J.

Similarly, the second harmonic amplitude V_2^{Σ} is given by

$$|V_2^{\Sigma}|^2 = {V_2^A}^2 + {V_2^B}^2 + 2V_2^A V_2^B \cos(\delta\varphi_2) \ . \tag{3.38}$$

Numerical simulations reveal that only for $J = 1$ the second harmonic voltages of the two junctions add up in phase ($\delta\varphi_2 = 0$) in the full current range. As observed also for $R \neq 1$, $\delta\varphi_2$ may attain non zero

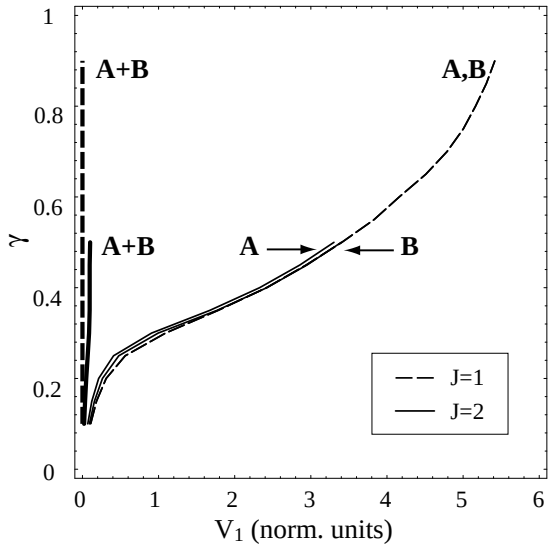

Figure 3.17: The first harmonic amplitudes $V_1^{A,B}$ and V_1^{Σ} plotted *vs.* γ for $J = 2$ (solid lines) and $J = 1$ (dashed lines).

values for a spread in critical currents. For $J = 1.10$ a transition from $\delta\varphi_2 \approx 0$ at $\gamma \approx 0.3$ to $\delta\varphi_2 \approx \pi$ at $\gamma \approx 0.8$ was observed while increasing bias current. For larger spread ($J \geq 1.30$) the second harmonic amplitudes are out of phase ($\delta\varphi_2 \approx \pi$) in the full range of the locked state stability, i.e. $V_2^{\Sigma} \approx |V_2^A - V_2^B|$. An example is given in Fig. 3.18 for $J = 2$ (solid lines). The second harmonic amplitude is suppressed substantially by the occurring shifts $\delta\varphi_2$ which are induced by the spread in critical currents J.

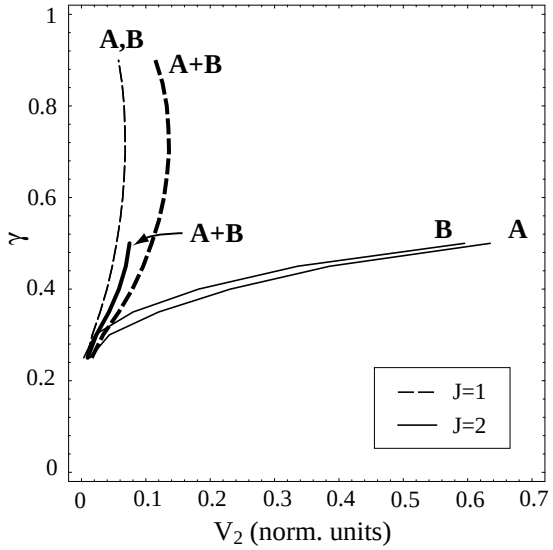

Figure 3.18: The second harmonic amplitudes $V_2^{A,B}$ and V_2^{Σ} plotted *vs.* γ for $J = 1$ (dashed lines) and $J = 2$ (solid lines).

The presented results suggest that stacked flux–flow oscillators operating in out–of–phase mode do not possess any advantages over single uncoupled LJJ oscillators. We note, however, that our model neglects the surface losses (β-term) and the nonlinearity of the quasiparticle conductivity α at high frequencies. A correction to the model with $\alpha = const$ could be including a damping term $\alpha^{A|B}(x,t)$ depending on the

amplitude of the local time dependent voltage $V^{A|B}(x,t)$. However, such an extension of the model is not very likely to lead to an increase of harmonic amplitudes since the damping increases with frequency. We found this effect in preliminary simulations with nonlinear quasiparticle losses.

3.3.3 In–phase mode

For equal JJ parameters, the phases of two junctions biased in the in–phase mode are identical $\phi^A(x) = \phi^B(x)$ [PUPS94, SBP93]. An analysis using magnetic images equivalent to that of the out–of–phase mode can be applied here as well. In Fig. 3.19 the magnetic image in JJ^B induced by fluxons in JJ^A is shown. In zeroth order approximation, its amplitude obeys the relation $\tilde{\phi}_x^A \approx \epsilon\bar{\phi}_x^A - \text{const}$, where $0 < \epsilon < 1$. Accordingly, the profile $\phi_x^B(x)$ in JJ^B is given by

$$\phi_x^B(x) \approx \bar{\phi}_x^B(x) + \tilde{\phi}_x^A(x) \approx \bar{\phi}_x^B(x) + \epsilon\bar{\phi}_x^A(x) - \text{const}\,. \tag{3.39}$$

The summation of the fluxon and the image profile is less accurate than in the out–of–phase case due to the high amplitudes of both $\bar{\phi}_x^B(x)$ and $\tilde{\phi}_x^A(x)$. The identical voltages of individual junctions add up in the in–phase state which results in an increase of the amplitudes of all harmonics. As an example, the voltage profiles $V^A(t)$ and $V^B(t)$ of equal amplitudes shown in Fig. 3.20 add up in phase to the voltage profile $V^\Sigma(t)$ of a larger amplitude.

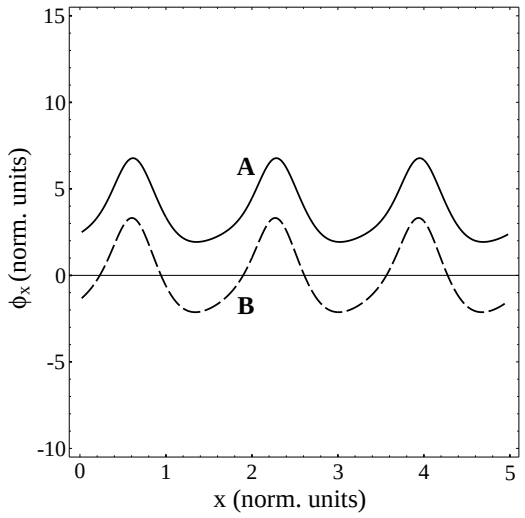

Figure 3.19: Normalized magnetic field profiles of junctions A and B at $\gamma = 0.7$ in the in–phase mode for $N^A = 3$ and $N^B = 0$ with coupling constant $S = -0.4$.

Expanding the voltage oscillations in each single junction into a Fourier series and summing the voltages for the in–phase mode, the amplitudes of the resulting signal can be expressed as [see Eqs. (3.24) –(3.27)]:

$$|V_k^\Sigma|^2 = {V_k^A}^2 + {V_k^B}^2 + 2V_k^A V_k^B \cos(\delta\varphi_k)\,, \tag{3.40}$$

where

$$\delta\varphi_k = \varphi_k^A - \varphi_k^B\,. \tag{3.41}$$

Here $\delta\varphi_k$ is the deviation from exact phase matching of each harmonic.

Identical junction parameters

The simulated dependence of V_1^Σ, V_2^Σ and V_3^Σ on γ for the stack of two identical junctions is shown in Fig. 3.21. For comparison, the SUJ amplitudes V_1, V_2 and V_3 are plotted as well. $V_1^\Sigma(\gamma)$ is nearly equal

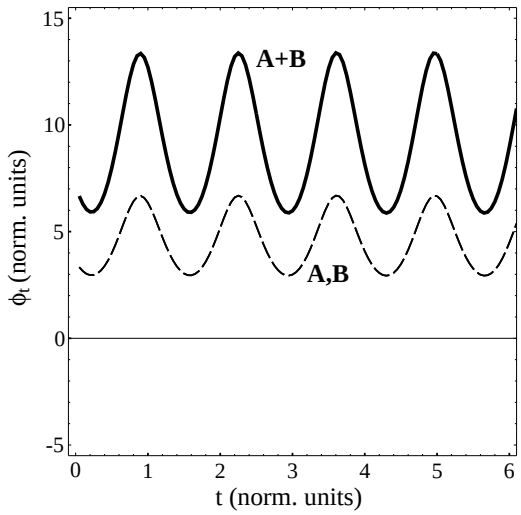

Figure 3.20: The time dependent voltages $V^A(x_0,t), V^B(x_0,t)$ and $V^\Sigma(x_0,t)$ at $\gamma = 0.5$ in in–phase mode.

to the first harmonic amplitude $V_1(\gamma)$ of the SUJ at $\gamma \approx 0.45$ and becomes approximately by 2.2 times larger than $V_1(\gamma)$ at $\gamma = 1$. The amplitude of the second harmonic V_2^Σ of the stack is equal to V_2 of SUJ at $\gamma \approx 0.6$ and becomes $V_2^\Sigma \approx 1.6\, V_2$ at $\gamma = 1$. Finally, the amplitudes of the third harmonic are approximately equal in the SUJ and the stack. We like to emphasize, that at the top of the resonance the first harmonic amplitude V_1^Σ is by more than a factor of two larger than V_1, i.e. the radiation power is larger by a factor greater than four. We suppose that this over–superradiant effect is due to the redistribution of power between high and low harmonics for SCJ's as compared with SUJ's.

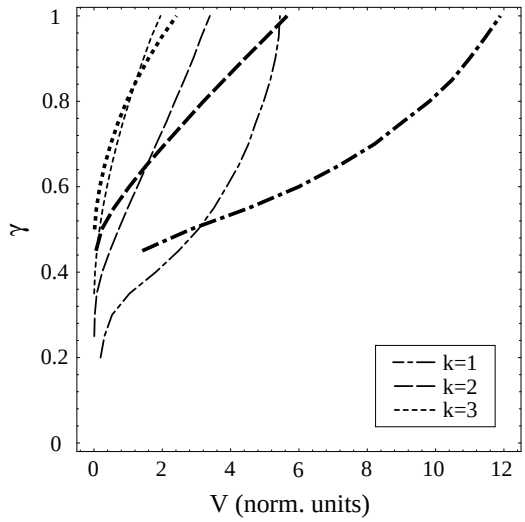

Figure 3.21: V_1, V_2 and V_3 of a stack of identical junctions (thick lines) and of the SUJ (thin lines) *vs.* bias current γ in the in–phase flux–flow mode.

In addition to the gain in amplitudes, in the in–phase mode we have an increase in frequency $\omega_1^+ = \omega_1^0/\sqrt{1+S} > \omega_1^0$ of all harmonics due to the higher propagation velocity in the c_+ mode. The increase in frequency is determined by the Josephson relation with the dc voltage of the SCJ (see Fig. 3.4). For $S = -0.4$, the voltage is by factor of $1/\sqrt{1+S} \approx 1.3$ larger due to the enhanced Swihart velocity

$\bar{c}_+ > \bar{c}_0$.

Spread in junction parameters

Spread in damping. The dependence of the first harmonic amplitude on the spread in quasiparticle resistances $R = R^{*A}/R^{*B}$ of the two coupled junctions is plotted in Fig. 3.22. In the studied parameter range, the amplitude V_1^Σ at constant current γ decreases linearly with increasing R. As the amplitudes in JJ^B decrease with respect to JJ^A due to larger damping, the total amplitude V_1^Σ of the coupled system decreases as well. In contrast, for $R^A < R^B$ the amplitude V_1^Σ increases.

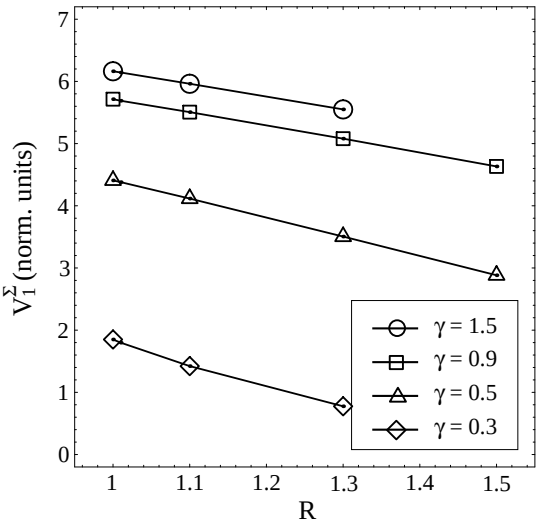

Figure 3.22: V_1^Σ at fixed bias values γ *vs.* the ratio of quasiparticle resistances $R = R^A/R^B$ for the in–phase flux–flow mode.

In the case of large spread ($R \geq 1.2$), the in–phase locked state was found to be impossible to achieve by cycling (with increasing and decreasing γ) through the hysteretic IVC. It can be argued that the junctions do not lock in phase anymore because the fluxon velocities in the two junctions considerably differ from each other at constant γ. Nevertheless, in simulations phase locking can still be achieved by using the appropriate initial conditions. Thus, the limited stability range is a disadvantage of the in–phase mode as compared with the out–of–phase mode. By increasing the coupling parameter S one can achieve more stable locking even for a larger spread. A more detailed discussion of the dependence of the locking range on the damping and the coupling can be found in chapter 4.

Spread in critical current density. Simulations of the in–phase mode with $J \neq 1$ revealed a similar behavior of voltage amplitudes [Eq. (3.36)] as discussed above for the out–of–phase mode. The voltage profiles $V^A(t), V^B(t)$ and $V^\Sigma(t)$ for $J = 2$ are illustrated in Fig. 3.23. The amplitudes V_1^A, V_1^B and V_1^Σ are plotted in Fig. 3.24 for $J = 2$, data for $J = 1$ are also shown as a reference. We note that the upper delocking current of the stack is reduced due to the twice lower critical current of JJ^B. In general, the upper delocking current j_{max} in the in–phase mode always assumes a value between the single junction critical currents j_c^A and j_c^B. Thus, for $J > 1$ the j_{max} is decreased, whereas for $J < 1$ the j_{max} is increased. As can be seen in Fig. 3.24, the dependence of V_1^Σ on the bias current γ is almost identical for the two values of $J = 1$ and $J = 2$. Hence the only substantial change in harmonic amplitudes arises from the modified locking range of the stack. This behavior was observed for all values of J where $0.5 \leq J \leq 2$. Figure 3.25 illustrates the dependence of V_1^Σ on the spread in critical currents J at constant γ. The qualitative behavior

is very similar to that of single junctions. For $J < 1$ we naturally observed an additional increase in V_1^{Σ} mainly due to the enhanced j_{max} of the stack.

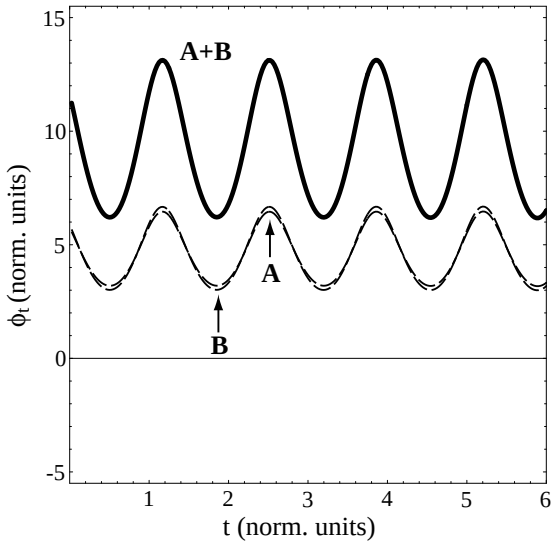

Figure 3.23: The temporal evolution of $V^{A,B}(t)$ and $V^{\Sigma}(t)$ in the in–phase flux–flow mode at $\gamma = 0.5$ is plotted for $J = j_c^A/j_c^B = 2$.

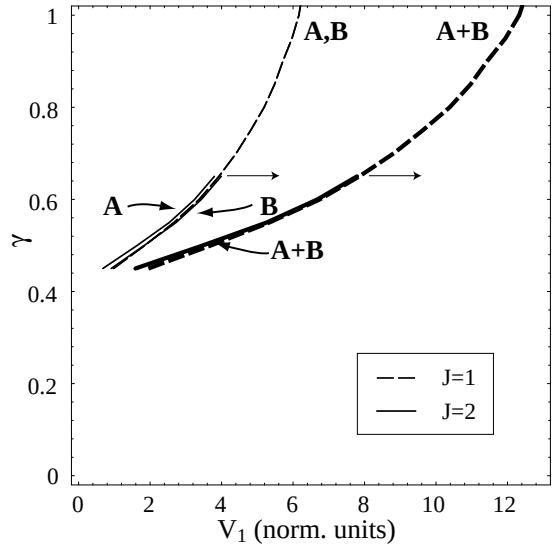

Figure 3.24: The first harmonic amplitudes of each single junction ($V_1^{A,B}$) and of the stack (V_1^{Σ}) are plotted as a function of γ for $J = 1$ (dashed lines) and $J = 2$ (solid lines).

In contrast to the out–of–phase mode, no substantial phase shifts $\delta\varphi_k$ that would influence the harmonic content of $V^{\Sigma}(t)$, were found in the in–phase mode. As a consequence, all higher harmonics add in phase, which results in a doubling of SCJ amplitudes. In comparison to the SUJ, some gain of the stacked oscillator in in–phase mode can be observed for V_2^{Σ} and V_3^{Σ} as well (see Fig. 3.21).

The use of LJJ stacks operating in the in–phase flux–flow mode is promising for applications since it increases the amplitudes of all harmonics. The comparison of the total voltage spectrum across the stack with the voltage spectrum of a SUJ shows that due to the in–phase summation and the magnetic coupling the first harmonic will be enhanced by more than a factor of two. Lower harmonics show an increase in

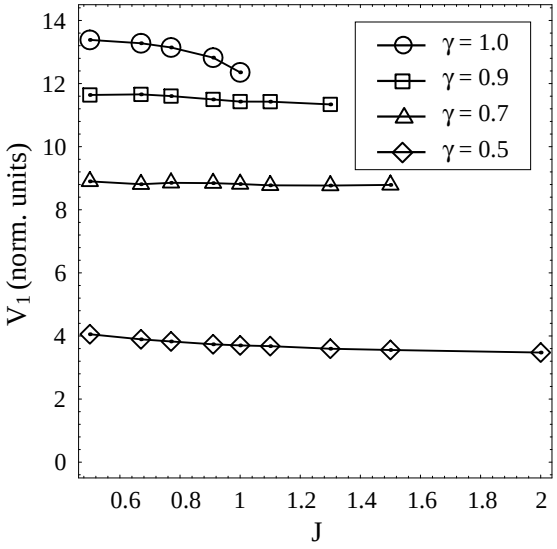

Figure 3.25: V_1^{Σ} as a function of the parameter J at constant levels of γ.

amplitude by a factor between two and one and the gain is decreasing with the order of the harmonic. The dependence of the gain in the first harmonic amplitude on the spread in critical currents is rather weak, whereas a spread in quasiparticle resistances leads to a decrease in gain.

3.3.4 Summary

The ac voltage spectra of double–barrier stacked LJJ's in in–phase and out–of–phase flux–flow modes have been studied in detail. In the frame of the theoretical model with frequency independent damping and absence of surface current losses, the out–of phase flux–flow mode is found to be not feasible for oscillator applications due to low power of all harmonics. In Fig. 3.26 the maximum values of the first and second harmonic amplitudes V_1 and V_2 in the out–of phase and the in–phase mode are plotted for spread in damping parameters (a), identical junctions (b) and spread in critical currents (c). For comparison the amplitudes of the SUJ with parameters identical to junction A of the stack are shown. Obviously, the out–of–phase harmonic amplitudes are by more than one order of magnitude smaller than the respective in–phase or SUJ values. Instead, the in–phase flux–flow mode is found to be of high interest for applications

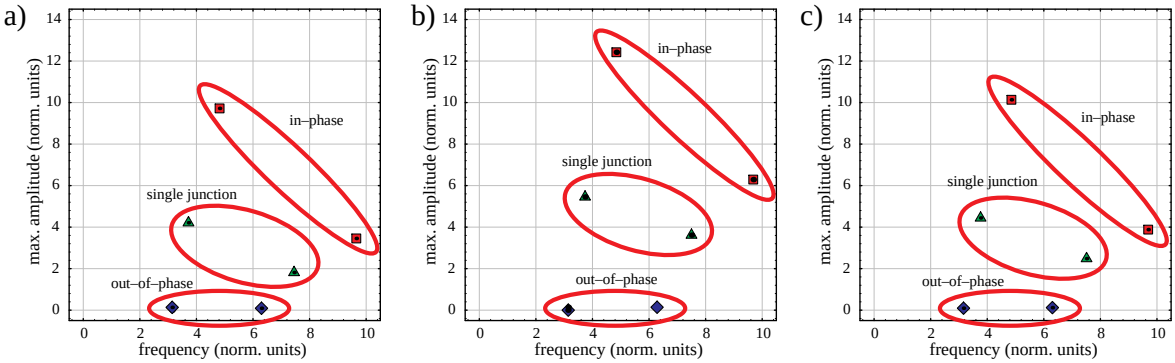

Figure 3.26: Maximum values of the harmonic amplitudes V_1 and V_2, for $R = 1.5$ (a), for identical junctions (b) and for $J = 1.5$ (c). Out–of–phase amplitudes are indicated by diamonds, in–phase amplitudes by squares and SUJ amplitudes by triangles.

that require enhanced power and frequency yield. Though the in–phase amplitudes are decreased for

spread in junction parameters (see Fig.3.26), they still possess advantages over single junctions as long as the phase locking can be achieved.

The harmonic content of radiation from a twofold coupled stack is governed by the magnetic coupling between junctions, which is inducing magnetic images, and the phase dependent summation of single junction voltages. I have pointed out the important features of the voltage spectra of the stack in in–phase and out–of–phase modes taking into account differences in the junctions critical currents and quasiparticle resistances.

The in–phase flux–flow mode provides the possibility to obtain larger power for various harmonics in Josephson radiation. This mode has limited stability and is less robust than the out–of–phase mode with respect to the parameter spread. In experiment it may be stabilized by an accurate tuning to achieve locking [GKU96]. According to the simulations, the in–phase flux–flow mode can be obtained reliably even with rather large spread in critical currents of the junctions. For $\alpha > 0.1$ a spread in damping coefficients of about 10% can be tolerated. These conditions can be satisfied by modern Nb/AlO_x technology. Reliability of in–phase locking can be enhanced, by increasing the coupling parameter S, i.e. reducing the thickness of the middle superconducting electrode.

The numerically obtained results are compared with experimental measurements in the next section.

3.4 On-chip radiation detection

The detailed numerical analysis presented in the previous sections of this chapter was stimulated by the possibility to experimentally investigate the radiation from stacked long Josephson junctions. The work on both the experimental and the numerical investigation of radiation from stacked long Josephson junctions was conducted during the end of 1995 and the first half of 1996. On the experimental side our group at KFA collaborated with the Institute of Radio Engineering and Electronics (IREE) of the Russian Academy of Science in Moscow. The aim was to experimentally investigate the radiation emitted by twofold stacks using a broad band on-chip detector, to allow measurements at the first and second harmonics of the Josephson frequency. The results of the experimental work are published in [SUIK96].

In this section I briefly review some aspects of the on-chip detection scheme, discuss some of my own measurements on this system and compare the results of [SUIK96] to my numerical work.

3.4.1 Samples and experimental technique

To accurately determine the radiation characteristics of a stacked long flux–flow oscillator a detector with a high cut-off frequency and a broad bandwidth is required. These features are important to observe radiation in a wide range of bias conditions of the oscillator and at the same time to detect not only the fundamental harmonic, but higher order harmonics as well. The above requirements are difficult to meet with off-chip detection schemes. Efficient off–chip broad band coupling of the radiation from the oscillator to the detector is difficult to achieve with standard technology (e.g. waveguides). Therefore Shitov et al. designed an SIS Josephson detector coupled by a microwave circuit to a stacked Josephson junction, taking advantage of their experience building mm– and sub–mm band receivers using SIS mixers. In this section I briefly summarize the main features of the detector system and microwave circuitry. A detailed discussion of all aspects including references to earlier work on this topic can be found in [SUIK96].

Chip design

A schematic layout of the stacked junction including the microwave circuitry and the SIS detector is shown in Fig. 3.27. The top and bottom electrodes and the junction areas are indicated by different shades of gray. On the left hand side the twofold stacked oscillator and on the right hand side the SIS detector, each indicated by arrows, are shown. The oscillator is coupled to the detector using a microstripline including

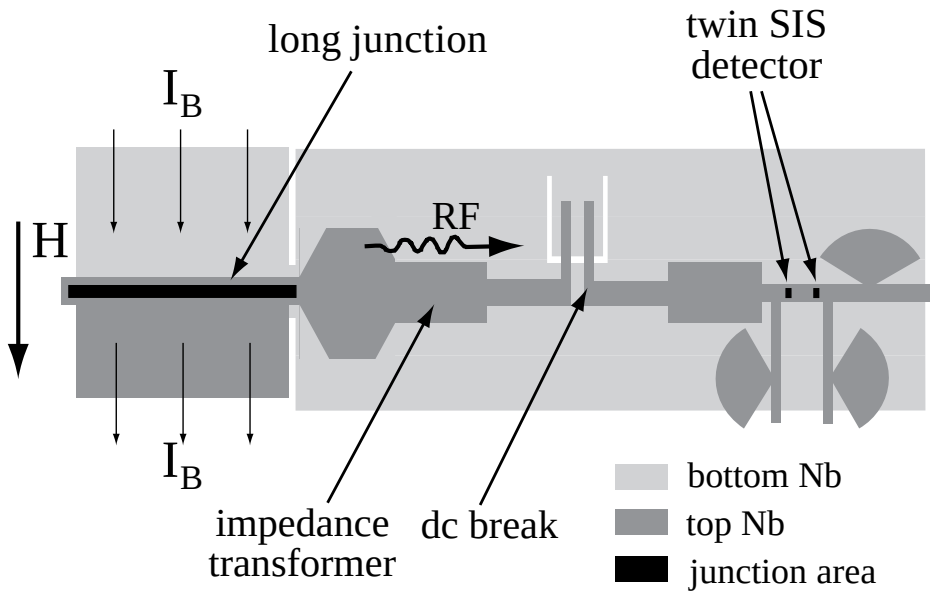

Figure 3.27: Design of oscillator and detector coupled on chip by microwave circuitry.

an impedance transformer and a dc break. The impedance transformer is necessary to correct for the impedance mismatch between the oscillator and the detector. The dc break decouples the dc bias currents of the detector and oscillator, ideally without affecting the rf coupling via the stripline. On the right hand side the detector is surrounded by three radial stubs which act as low pass filters to avoid the leakage of rf power through the bias lines of the detector. All elements are specifically designed to provide a broad band homogeneous coupling between the oscillator and the detector. The bandpass of the coupling circuit shown in Fig. 3.28 was calculated and numerically optimized by S. Shitov. In the range between 150 and 450 GHz the coupling is about -4 db with a flatness of about 1 db.

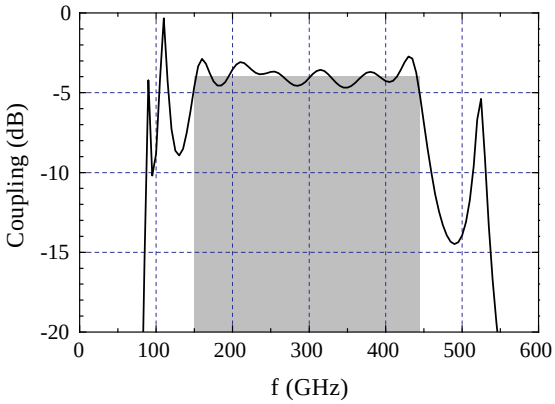

Figure 3.28: Coupling showing the losses between the oscillator and the detector in dB vs. frequency, i.e. bandpass of the coupling circuit.

Experimental technique

To measure the radiation from the stacked long Josephson junction oscillator, the chip containing both the oscillator and the detector is mounted on a sample holder and bonded, such that the detector and the oscillator can be biased individually. The dc voltage drop across each junction is measured using a 4 point technique to avoid contact resistances. To apply a homogeneous magnetic field in the junction plane of the oscillator the sample holder is placed into a cylindrical superconducting coil and aligned in parallel to its

axes. To shield the sample (including the coil) from external electromagnetic fields a cylindrical cryoperm screen is used. Subsequently the chip is immersed into a liquid helium cryostat using a dip stick. By applying an external magnetic field and a bias current to the stacked junction it can be set into a dynamic state in which it emits radiation. If the frequency of the emitted radiation is within the transmission range of the microwave stripline, it can be coupled to the detector. As a result, photon assisted tunneling (PAT) steps can be observed on the IV curve of the detector. By analyzing the width and the height of such steps, the frequency and the power of the emitted radiation can be determined. A concise explanation of the origin of photon assisted tunneling steps can be found in [Sol72]. The basics of the Tien-Gordon theory, which allows for a quantitative calculation of the pumped IV characteristics of the detector, and a variety of references to early experimental results can be found in [Sol72] as well.

Outline of evaluation of pumped detector characteristics

Only a brief outline of the evaluation technique for pumped IV curves of a small SIS detector junction shall be presented here. As an example in Fig. 3.29 three experimentally measured IV curves of the idle (a) and pumped [i.e. irradiated by the stacked oscillator] detector (b,c) junction are shown for two different states of the oscillator. These IV curves can be approximated using the Tien–Gordon [Sol72] expansion

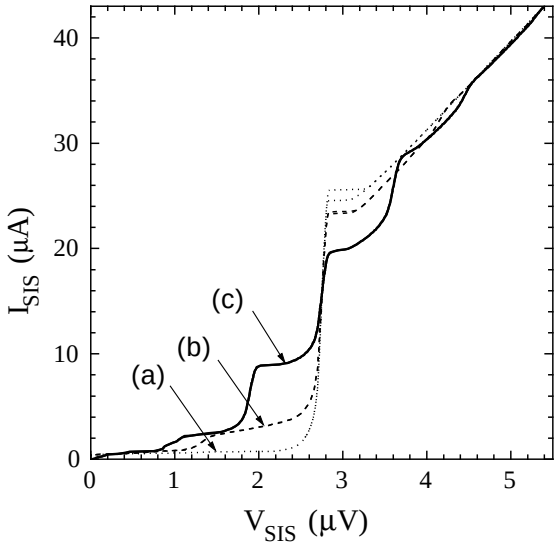

Figure 3.29: IV curves of unpumped (a) and pumped (b,c) SIS detector.

$$I = \sum_{n=-\infty}^{\infty} J_n^2(\alpha) I_0(eV + n\hbar\omega) \; , \tag{3.42}$$

where J_n is the n^{th} order Bessel function of the first kind, $I_0(V)$ is the unpumped IV characteristic and α is given by

$$\alpha = \frac{eV_\omega}{\hbar\omega} \; . \tag{3.43}$$

V_ω is the amplitude of incident radiation. Thus knowing the unpumped IV characteristic $I_0(V)$ one can fit Eq. (3.42) to the pumped IV curve using the free parameters α and ω. Finally the power of the radiation can be evaluated, if the impedance of the junction is known.[3]

[3]The full evaluation procedure developed by S. Shitov uses some extensions to this model, to predict the real power more accurately. For an extended review of SIS junctions used as detectors and mixers see [TF85].

3.4.2 Measurements

6 wafers, containing 6 chips each, were fabricated by N. Iosad at KFA. The chips were made with different middle electrode thicknesses of the stacked oscillator, to investigate different coupling regimes. The yield of working systems was comparatively low. This had numerous reasons. The main reason is related to the fact that the three elements, i.e. the stacked oscillator, the SIS detector and the rf coupling circuit, simultaneously have to have good characteristics to end up with an well performing system. Below I briefly discuss the main reasons for poorly performing elements of the system.

- **Flux–flow oscillator.** A well performing oscillator with pronounced regions of in–phase and out–of–phase locking (see Sec. 2.4) is required to identify its oscillation mode using the dc IV characteristics. Bad performance of the oscillator (e.g. no phase locked regions observable, unstable steps etc.) is most often caused by too large differences in the critical currents or subgap resistances of the comprising junctions (see Sec. 3.3).

- **Detector.** The very small (area $< 1\ \mu\mathrm{m}^2$) and high resistive ($R \approx 100\ \Omega$) detector junction is very sensitive in fabrication and in later use. The detector can easily be destroyed by to high bias currents ($I_c < 20\,\mu\mathrm{A}$) or static discharges upon mounting or connecting the detector to measurement equipment. Moreover, the detector junction is very sensitive to thermally induced stress between the layers of the structure. As a consequence superconducting shorts were observed frequently in initially working detector junctions after thermocycling. A number of detectors showed a small subgap resistance (i.e. a too high quasiparticle current below the gap voltage) in the unpumped state, which makes fitting of the pumped IV curves to the Tien–Gordon theory difficult or even impossible.

- **Coupling circuit.** The performance of the coupling circuit could only be evaluated in cases, when the oscillator and the detector were performing reliably. Some chips displayed poor coupling between the oscillator and the detector, presumably due to deviations from the designed value of the impedance. As a consequence the PAT steps on the detector could not be analyzed due to their small amplitudes.

As a result most measurements of this set of chips were not feasible for detailed systematic evaluation. Nevertheless, photon assisted tunneling steps could be observed and dc measurements of stacked flux–flow oscillators have been performed. Altogether, 12 chips were tested in my work. From the prepared series only two chips performed well enough to do systematic measurements. The measurements of one of them performed by A. Ustinov [SUIK96] are presented, discussed and compared to my numerical simulations in the next section.

3.4.3 Results

In Fig. 3.30 a superposition of the dc IV characteristics of the flux–flow oscillator in a range of magnetic fields is shown. A more detailed discussion of these characteristics is needed to understand the results of radiation measurements presented subsequently.

First the characteristic in Fig. 3.30 can be subdivided into two parts: a) $V < V_g^A$ and b) $V > V_g^A$, where V_g^A is is the gap voltage of the junction with lower j_c. Below V_g^A phase locked states of the coupled oscillators are possible. Above V_g^A one junction is switched to the gap state, while the other one is not, such that no phase locked states can be observed. In the voltage range $V < V_g^A$, one can clearly distinguish different regimes of oscillations in the junction. In this range two families of Fiske steps (FS_- and FS_+) with different spacings are observed. This is clearly an indication of the two different modes existing in the junction (see Sec. 2.4). The flux–flow (FF) regime is also indicated in Fig. 3.30. At voltages above V_g^A, FS_- steps of one junction are observed.

To measure the radiation from the stacked FFO a fixed magnetic field H is adjusted, such that the generated radiation has sufficient power for PAT steps to be observed on the detector and its frequency is

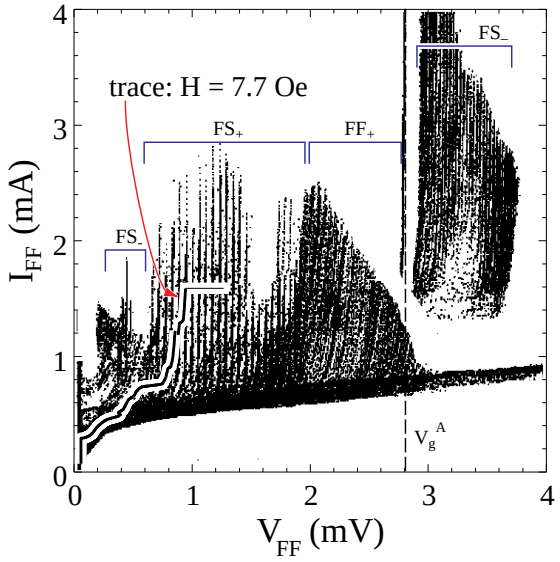

Figure 3.30: Storage oscilloscope traces of FFO characteristics in a range of magnetic fields. Different oscillation regimes are indicated.

in accordance with the limitations quoted above. In Fig. 3.30 the IV curve of the oscillator at $H = 7.7$ Oe is emphasized. At this value of H the power and the frequency of the radiation emitted by the stack were measured at different bias points. In Fig. 3.31 an enlarged version of this IVC is shown. Bias points at which measurements were performed are indicated by hollow and solid circles indexed with a number. Additionally, the dc voltage range at which radiation of the first and second harmonic frequencies can

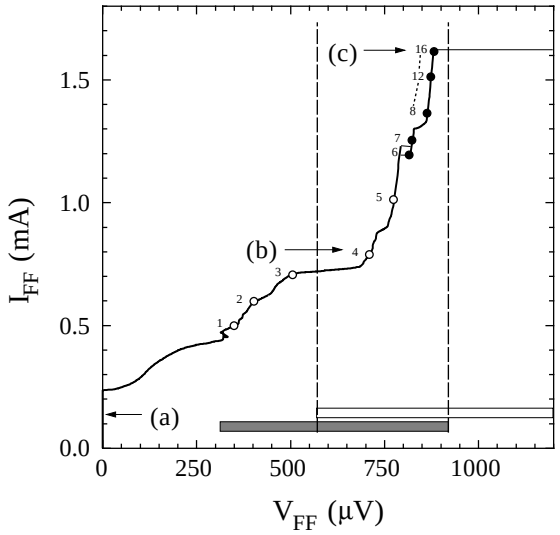

Figure 3.31: IV curve of FFO at magnetic field $H = 7.7$ Oe. Bias points at which measurements of the emitted radiation were performed are indicated by circles and indexed by a number. The white and gray bar mark the respective voltage regions at which the first and second harmonic radiation can be detected. Their overlap is indicated by vertical dashed lines.

be observed is marked in Fig. 3.31 according to the bandwidth limitations of the coupling circuit. The voltage ranges, indicated by bars, are calculated using the ac Josephson relation and assuming an effective bandwidth from 150 to 450 GHz. As a result first and second harmonic radiation could only be observed simultaneously in a rather limited voltage range between the two dashed lines in Fig. 3.31.

The IV curves of the detector junction corresponding to the bias points (a), (b) and (c) of the oscillator

(see Fig. 3.31) are shown in Fig. 3.29. From these curves and similar plots at other bias currents the power and the frequency of the emitted radiation was determined using the Tien-Gordon theory. Upon fitting the pumped IVCs to the model only the power of the predominant frequency was determined, even though the radiation may have some additional harmonic content. In Fig. 3.32 the acquired frequencies are plotted versus the dc voltage drop across the oscillator. Obviously the predominant frequencies show two different dependencies on the dc voltage. At low bias currents and voltages (hollow circles) high frequencies according to the second harmonic of the Josephson frequency are detected. At high bias currents and voltages (solid circles) lower frequencies according to the first harmonic are detected. This is

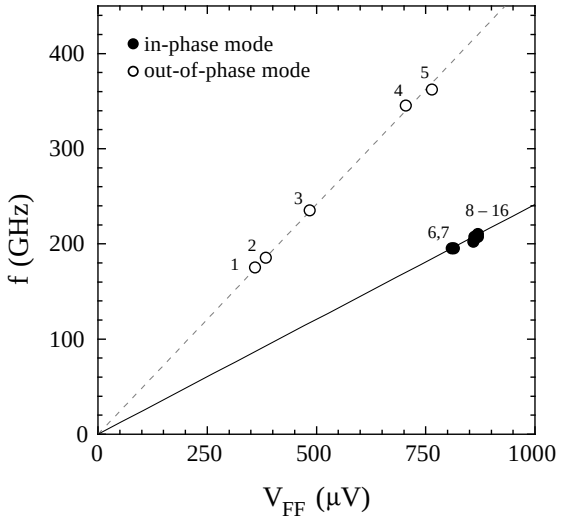

Figure 3.32: Measured frequency vs. dc voltage drop across oscillator. Lines show theoretical dependence of the Josephson frequency on the voltage for the first and second harmonic. Indices of data points are in accordance with the indices in Fig. 3.31.

a clear indication for in–phase and out–of–phase locking of fluxons in the stacked oscillator. The result is in agreement with the numerical observations presented earlier in this chapter. In simulations it has been shown that odd harmonics are completely suppressed in the lower voltage out–of–phase coupled modes. At higher voltages the coupled oscillators can be synchronized in phase and the predominant power is detected at the fundamental frequency.

Power levels P determined from the pumped IVCs are presented in Fig. 3.33. Apparently the power detected from in–phase modes is substantially larger than the power detected from out–of–phase–modes. However, one has to take into account the different bias levels under which the respective states are stable, which may account for part of the differences. In Fig. 3.34 the voltage amplitudes $V_i \propto \sqrt{P}$ are plotted vs. the normalized bias currents I/I_c in order to give a representation of data which is similar to the one used in numerical simulations (see Figs. 3.13 and 3.21, for example).

Most important, it can be noted that out–of–phase amplitudes are much larger relative to in–phase amplitudes than expected from the numerical simulations, which predict almost vanishing out–of–phase amplitudes. This may have a number of reasons:

- Data measured in this experiment is not acquired in the flux–flow mode of the oscillator, but in the Fiske mode.[4] In the Fiske regime some deviation from the numerical results for the flux–flow regime may appear.

- The normalized bias currents at which steps have been observed experimentally are much lower than the ones investigated numerically. In simulations the stability of oscillatory modes is probably

[4]In practical oscillator applications Josephson junctions are always used in FF mode, because only this mode provides a continuously tunable radiation frequency (see Sec. 2.2.2). In experiment the FF regime could not be investigated due to a too low cut off frequency of the coupling circuit.

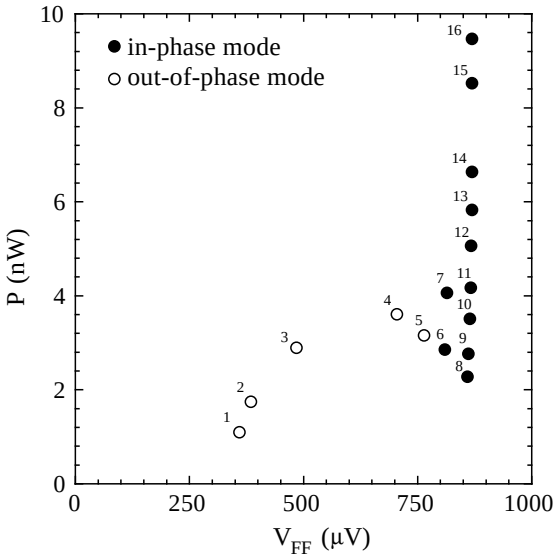

Figure 3.33: Detected power of radiation in dependence on voltage across the oscillator. Again indices correspond to bias points in Fig. 3.31.

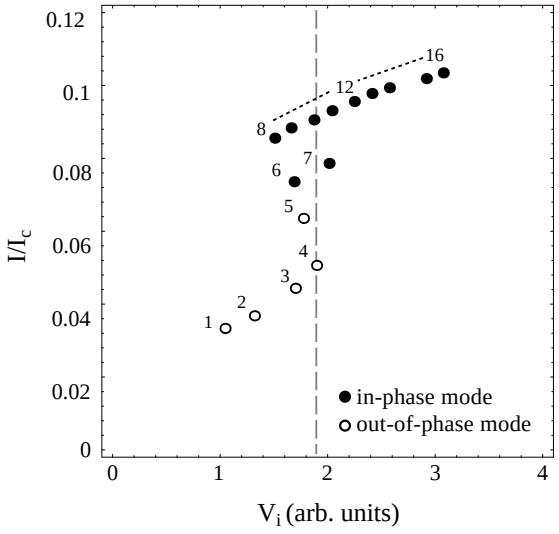

Figure 3.34: Amplitude of radiation (arbitrary units) in dependence on normalized bias current. The maximum power detected in the out–of–phase mode is indicated by a dashed line.

largely overestimated, because only ideally homogeneous junctions are considered and no noise is present.

- Loading effects from the coupling circuit and the detector can have a substantial influence on the dynamics of the oscillator. These effects were not considered in the simulations.

- The bandpass of the coupling circuit was only determined by numerical analysis. No "true" performance of the bandpass is known. Therefore the measured power cannot be corrected to the "true" power of the oscillator by taking into account the coupling circuit characteristics.

3.4.4 Conclusions

The experimental investigation of radiation from a twofold stacked oscillator has shown that it actually operates in two different modes with two different radiation characteristics, as seen in numerical simulations. The out–of-phase mode is characterized by its dominant radiation frequency at the second harmonic and the in–phase mode by its frequency at the first harmonic, which is in agreement with the numerical simulations. The experimentally observed power in the out–of–phase mode is substantially larger in comparison to the detected in–phase power, than expected from numerical simulations. Possible reasons for this are discussed at the end of the previous section. The absolute value of the total power detected from our stack in any accessible mode is still by one to two orders of magnitudes smaller than the maximum power detected with similar schemes from a single oscillator in flux–flow mode [KSF$^+$97]. Even if the differences in critical current densities of our chip in comparison to the chip used in [KSF$^+$97] are taken into account, the maximum power achieved with a single oscillator is by a factor of 4 larger than that of our twofold stack. However, we note that by now no statistics over more than 2 samples is available for this type of stacked devices

From an experimental point of view, the coupling of the oscillator to the detector has to be extended to higher frequencies to allow true flux–flow operation to be observed from the oscillator. There are limitations in the performance of Nb based coupling circuits, because losses strongly increase for frequencies above $\nu = \Delta_{sc}/2h$. Alternatively, the $\alpha\ell$–parameter of the junctions has to be increased in order to make flux–flow states stable at lower voltages.

From the point of view of numerical simulations of stacked FF oscillators for real devices, one has to take into account the β–term losses and the interaction of the oscillator with the coupling circuit and other elements of the device. However, his will render the dynamics of the system even more complex than in the case considered in this work. Moreover, the parameters of the system simulated would have to be chosen closer to real system parameters, which in most cases would make calculations more time consuming to perform.

Finally one may conclude, that stacked oscillators in principle provide the possibility to get enhanced output power, when operating in the in-phase locked regime. But for application of these oscillators in real devices the issues of fabricating junctions with as identical parameters as possible and the design of broad band coupling circuits for their analysis have to be addressed in more detail.

Chapter 4

Delocking of flux–flow states in dc–driven magnetically coupled Josephson junctions

In chapter 3 "Coherent radiation emission by two stacked Josephson flux–flow oscillators" the influence of differences in junction parameters of the stack is investigated in detail. In the discussion of the various effects only phase locked states were taken into account. Still, the phase locked current range of such a system strongly depends on the spread in individual junction parameters of the stack. A complicated and interesting locking behavior of this system was observed first in numerical simulations and further stimulated interest in finding a model to explain the behavior of the system.

In this chapter the dependence of the phase locked current range of two magnetically coupled annular Josephson junctions in flux–flow mode on the spread in quasiparticle resistivities (i.e. damping parameters) is investigated numerically and theoretically. The analytical model describing the coupled system was developed by B. Malomed after stimulating discussions of my numerical results.[1] The theoretical model was verified and applied to the simulated data in a joint work between E. Goldobin and me. The results of this work [GWMU96] are accepted for publication in Physics Letters A. At the end of this chapter a method for experimental observation of the phenomena discussed is proposed. Finally a conclusion is given.

A similar locking/delocking problem has already been considered, both theoretically and experimentally, in [BMP$^+$95] for junctions with identical dissipation constants but different bias currents. In another recent work [GJBS96], synchronization and desynchronization of two JJs operating in flux-flow regimes in relatively short linear coupled junctions was considered from the viewpoint of the Fiske-step theory. For the single fluxon case, the analytical and numerical analysis of delocking was accomplished in [GJOS93] for the case of different Swihart velocities of Josephson junctions. Due to the small value of the coupling parameter $|S| \equiv |\Delta| = 0.05$ in [GJOS93], the authors gave an incorrect interpretation of the delocked state. In the delocked state fluxons in the stack move with velocities $\bar{c}_-$ and $\bar{c}_+$ that characterize the whole system [GGU96] rather than with velocities $\bar{c}_1$ and $\bar{c}_2$ that characterize uncoupled Josephson junctions. Having small Δ, $\bar{c}_1$ is very close to $\bar{c}_-$ and $\bar{c}_2$ is very close to $\bar{c}_+$.

4.1 Modeling and numerics

The analysis of magnetically coupled annular Josephson junctions (JJ's) presented in this chapter is carried out for stacked junctions of identical geometry and identical electrical properties, but different dissipation constants. In contrast to the study presented in [BMP$^+$95] the two junctions comprising the stack are biased in series by the same homogeneous current. This situation is relevant for a typical experiment, where the stack is biased by a common current. The electrodynamics of this system are again well described by the Sakai, Bodin, Pedersen model discussed in detail in section 2.3.2. The system of equations governing the

[1] B. Malomed visited our group at KFA in march 1996.

dynamics of the stack according to the above assumptions can be written as

$$\begin{array}{rrrrrr} \frac{1}{1-S^2}\phi^A_{\bar{x}\bar{x}} = & \sin\phi^A + & \phi^A_{\bar{t}\bar{t}} + & \alpha^A\phi^A_{\bar{t}} - & \gamma + & \frac{S}{1-S^2}\phi^B_{\bar{x}\bar{x}} \\ \frac{1}{1-S^2}\phi^B_{\bar{x}\bar{x}} = & \sin\phi^B + & \phi^B_{\bar{t}\bar{t}} + & R\alpha^A\phi^B_{\bar{t}} - & \gamma + & \frac{S}{1-S^2}\phi^A_{\bar{x}\bar{x}} \end{array} \quad , \tag{4.1}$$

where $R\alpha^A = \alpha^B$ is the effective dissipation constant of the bottom junction. To investigate the phase synchronization in the present model, $L = 5$, $\alpha^A = 0.1$, and the periodic boundary conditions

$$\begin{cases} \phi^{A,B}\Big|_{x=0} = \phi^{A,B}\Big|_{x=L} - 2\pi N^{A,B} \\ \phi^{A,B}_x\Big|_{x=0} = \phi^{A,B}_x\Big|_{x=L} \end{cases} \tag{4.2}$$

were chosen. The periodic boundary conditions allow to neglect Fiske resonances in the system, thus, concentrating the attention on the flux-flow regimes. The number of fluxons N is preserved during simulations due to the boundary conditions (4.2). N defines the fluxon density in each JJ and is equivalent to the applied external magnetic field in the case of linear geometry. Equal fluxon densities $N_A = N_B = N$ were chosen for both junctions.

Numerically the system of Eqs. (4.1) was solved according to the discretization scheme presented in section 3.2. A typical numerically acquired current–voltage characteristic is presented in Fig. 4.1 for $\alpha^A = 0.1$, $\alpha^B = 0.15$ and $S = -0.5$ for three enclosed fluxons in each junction in the normalized bias current range $\gamma = 0.0 \ldots 0.7$. In the plot the voltage drop across each junction (black line, junction A and gray line, junction B) is shown together with the voltage across both junctions (thick line).

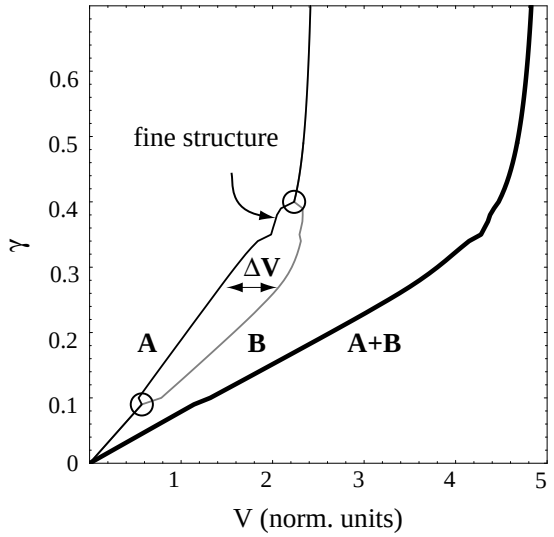

Figure 4.1: IV characteristic for $0.0 \leq \gamma \leq 0.7$, displaying locked and unlocked regions together with the two unlocking/relocking points indicated by the small circles. A and B are indices of the respective junctions. ($\alpha^A = 0.1$, $\alpha^B = 0.15$, $S = -0.5$)

In usual experiments only the total voltage can be measured, because electrical contact is only provided to the top and bottom electrodes. Nevertheless, in numerical simulations it is possible to obtain data of each single junction, because the phases $\phi^{A,B}$ are calculated separately. A proposal for measurements to confirm the simulated data shown in Fig. 4.1 is discussed in Sec. 4.5.

The region in which the two voltages V^A and V^B coincide in Fig. 4.1 corresponds to the voltage locked state when both fluxon chains move with the same velocity. In the delocked regions the difference in dc voltage ΔV between the two junctions is a measure of the difference in their velocity. In this state the two chains slide one along another. Thus a good indicator for the locked state is the difference in voltage between the junctions $\Delta V = V^B - V^A$. In Fig. 4.2 ΔV is plotted in dependence on γ for the same parameters as in Fig. 4.1. The locking and delocking points (γ_i, V_i) are found numerically by determining

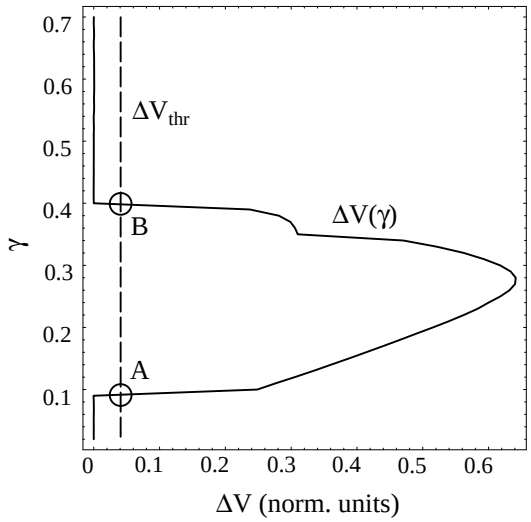

Figure 4.2: $\Delta V(\gamma)$ for the parameters quoted in Fig. 4.1 and the delocking threshold ΔV_{thr}. A and B mark the decoupling and recoupling points, respectively.

the intersection between a threshold voltage $\Delta V_{thr} = 0.0025$ and $\Delta V(\gamma)$ as shown in Fig.4.2. It is rather important to note that the total voltage across the stack (thick line in Fig. 4.1) shows almost no variation between locked and delocked states. From the fine structure on the characteristic (see arrow) one can infer details about fluxon interactions. A more detailed description on the features of the IV curve can be found in the next section.

4.2 Characteristic locking/delocking features

The numerically obtained IV characteristic of Fig. 4.1 is shown in more detail in Fig. 4.3. The current is proportional to γ, and the average voltage is proportional to the fluxon velocity. One can see that the junctions are locked at zero driving current. This can be easily understood. In a static state, the fluxons in the two junctions repel each other (coupling Force F_Δ) and form a triangular array, which corresponds to the locked state. Applying a small bias current, one makes the fluxon array move as a whole. With increase of the bias current and the corresponding velocity, the difference of the friction forces acting upon the two chains also increases. Beyond the decoupling point the coupling force between the chains can no longer compensate this difference.

The decoupling point is marked by A in Fig. 4.3. After decoupling, the chains are sliding relative to each other. However, with further increase of the bias current, the motion of the decoupled chains becomes relativistic, i.e. their velocities approach the limiting (Swihart) velocity $\bar{c}_-$. The velocities get closer again, thus the friction force difference gets small, and, finally, the locked state is recovered (point B in Fig. 4.3). This explanation of the delocking and relocking is a qualitative interpretation which will be justified by the analytical calculations presented in the next section.

The simulated IV curve in Fig. 4.3 demonstrates a small-scale hysteresis around the delocking and relocking points. This hysteresis is not explained by the theoretical model to be presented in Sec. 4.3, because the model only considers transitions from the locked to delocked states. The hysteresis might be due to the different dynamics of the system upon relocking of phases. A more detailed discussion of these small scale effects is omitted in the current work.

In Fig. 4.3 one can also see an interesting feature on IV curve close to the hysteresis region between points B and C marked as “collisions” [Gol]. This is a mode which is different from viscous sliding of two fluxon chains relative to each other. The fluxon chains become less dense in the region near the resonance and single fluxon-fluxon collisions start to be important. The fluxon moving with higher velocity in one JJ

collides with the slower fluxon from the other JJ. A part of the kinetic energy is transferred from the fast fluxon to the slow one which results in a change of velocities of fluxon chains as a whole. This change of velocities can be seen as the above mentioned feature in the IV curve. These collisions can be observed by simulating a long ($\ell = 20$) stack with one fluxon in each JJ and different damping parameters. Depending on parameters, the collision region may appear in the I-V curve.

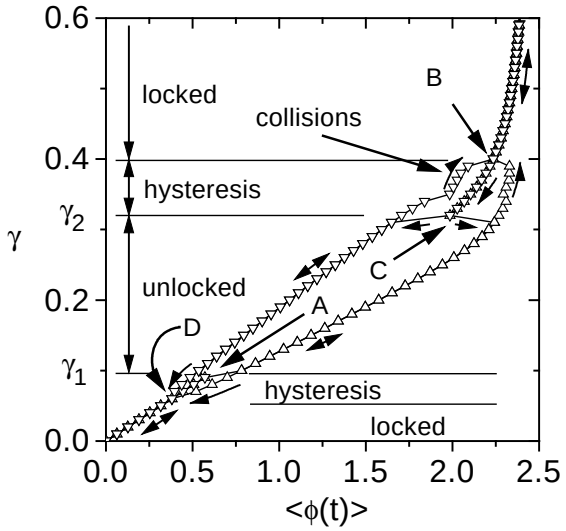

Figure 4.3: IV curve of the annular stacked JJ with delocking region. The parameters of the system are: $\Delta = 0.5$, $\alpha^A/\alpha^B = 1.5$, $N = 3$, $L = 5$. A and C are delocking points, B and D are relocking points.

4.3 Theoretical model

Analytically the PSGE system 4.1 can be solved in the approximation of large fluxon density using the well established perturbation theory for the PSGE. A similar analytical approach was already considered in [BMP+95] which will be extended to the relativistic case, because the most important effect, i.e. the decoupling of the fluxon chains in the junctions, mainly takes place in the relativistic region. The comparison of analytical results with numerical simulations shows that the model only provides satisfactory agreement in its general relativistic form. First Eqs. (4.1) are simplified to

$$\begin{aligned} \phi^A_{\bar{x}\bar{x}} - \phi^A_{\bar{t}\bar{t}} - \sin\phi^A &= -\gamma + \alpha^A \phi^A_{\bar{t}} - \Delta\phi^B_{\bar{x}\bar{x}} \\ \phi^B_{\bar{x}\bar{x}} - \phi^B_{\bar{t}\bar{t}} - \sin\phi^B &= -\gamma + \alpha^B \phi^B_{\bar{t}} - \Delta\phi^A_{\bar{x}\bar{x}} \end{aligned} \tag{4.3}$$

by renormalising the spatial coordinate as

$$\bar{x} = (1 - S^2)\tilde{x} \tag{4.4}$$

and rewriting the coupling term $S = -\Delta$ with $\Delta > 0$ as done in most of the literature concerning perturbation theory of coupled sine–Gordon systems. The sign of the bias current term γ is arbitrarily chosen negative.

Solely the case of two fluxon chains locked in out-of-phase mode is considered here. The system of equations (4.4) will be solved for cases, when multiple fluxons are enclosed in the junction. This situation corresponds to the flux–flow regime, i.e. multi–soliton solutions have to be used in the perturbation approach. The exact multi–soliton solutions on finite rings found by Kulik [Kul67] are complicated in comparison to the dense fluxon chain approximation. Therefore the latter is used in this calculation. Neglecting the perturbation terms at the r.h.s. of Eqs. (4.4), one can derive the solution for $\phi^{A,B}$ in the high fluxon density limit, when the mean magnetic field $H \equiv \overline{\phi^A_x} = \overline{\phi^B_x}$ is a large parameter. This is a standard

approximation to the solution of Eqs. (4.3), which is discussed briefly in appendix C. The solution can be conveniently represented by the expansion

$$\phi^{A,B} = (x - ut - \xi_{A,B})H - \frac{\sin\left[(x - ut - \xi_{A,B})H\right]}{H^2\left(1 - u^2\right)}, \tag{4.5}$$

where u ($0 < u < 1$) is the fluxon chain velocity. u is normalized to the modified Swihart velocity $\bar{c}_- = \bar{c}_0/\sqrt{1+\Delta}$, i.e. the maximum fluxon propagation velocity in that mode. It is assumed to be the identical for both JJ's, i.e. we consider the phase locked case. ξ_A and ξ_B are arbitrary constants representing the collective coordinate of the fluxon chain in each junction. In the limit of dense fluxon chains the dynamics is completely determined by this single coordinate of the rigid chain.

As in [BMP+95], each fluxon chain is now considered as an effective particle with the single degree of freedom ξ_A or ξ_B, for which equations of motion have to be found. The momentum of each "particle" is

$$P_{A,B} = -\int_0^L \phi_x^{A,B}\phi_t^{A,B}\,dx = H^2 uL, \tag{4.6}$$

L being the length of the junction.[2] L and H are related according to the periodic boundary condition, $HL = 2\pi N$, where N is the number of the flux quanta trapped in the annular junction, i.e. H is quantized.

Now, the equation of motion can be found by equating the time derivative of the momentum and the net force applied to the particle according to Newtons laws. In the model, we have three forces acting on the "particles": friction F_α, driving F_γ, and coupling F_Δ forces. First of all, it is straightforward to find the friction force by considering the appropriate term of equation (4.3). Using the expression for the momentum (4.6) with the unperturbed solution in the dense fluxon chain approximation one finds

$$F_\alpha^{A,B} = -\alpha^{A,B}P_{A,B} = -\alpha^{A,B}H^2 uL\ . \tag{4.7}$$

The driving force is given by

$$F_\gamma = \gamma HL. \tag{4.8}$$

Next, the simplest way to calculate the coupling force F_Δ is using the coupling Hamiltonian H_Δ which generates the coupling terms in the Eqs. (4.3):

$$H_\Delta = -\Delta\int_0^L \phi_x^A\phi_x^B\,dx. \tag{4.9}$$

Substituting the approximation (4.5) into (4.9), one obtains

$$H_\Delta = -\frac{1}{2}L\Delta\frac{\cos\left[(\xi_A - \xi_B)H\right]}{H^2\left(1-u^2\right)^2}. \tag{4.10}$$

Finally, the coupling force F_Δ acting on each "particle" can be obtained from (4.10) as

$$F_\Delta = -\frac{\partial H_\Delta}{\partial \xi_{A,B}} = \frac{1}{2}L\Delta\frac{\sin\left[(\xi_A - \xi_B)H\right]}{H\left(1-u^2\right)^2}. \tag{4.11}$$

To get a stationary solution corresponding to a constant velocity u, we insert the expressions (4.7), (4.8), and (4.11) into the Newton's equations of motion for the two "particles"

$$\frac{dP_{A,B}}{dt} = F_\gamma^{A,B} - F_\alpha^{A,B} \pm F_\Delta. \tag{4.12}$$

[2]The expression for the momentum P can be found by using Noether's theorem. A very general derivation of P from quantum field theory is presented in [BS83, BS59].

and consider $dP_{A,B}/dt = 0$. By adding or subtracting the equation of motion of each "particle" from one another we find the two equations solving our problem

$$\gamma = \frac{1}{2}\left(\alpha^A + \alpha^B\right) H u, \tag{4.13}$$

$$\Delta \frac{\sin\left[(\xi_A - \xi_B)H\right]}{H\left(1-u^2\right)^2} = \left(\alpha^A - \alpha^B\right) H^2 u. \tag{4.14}$$

From a formal point of view, a solution to these equations exists provided that it produces $|\sin\left[(\xi_A - \xi_B)H\right]| \leq 1$. Physically, the point $|\sin\left[(\xi_A - \xi_B)H\right]| = 1$ implies the cease of existence of a coupled state of the two fluxon chains, i.e. delocking. Eliminating the velocity u from Eqs. (4.13) and (4.14), we finally arrive at an inequality which determines the value of the bias current density at which the system is locked:

$$\frac{\alpha^A - \alpha^B}{\alpha^A + \alpha^B}\,\gamma - \frac{\Delta}{2H^2\left[1 - \frac{4\gamma^2}{H^2\left(\alpha^A+\alpha^B\right)^2}\right]^2} \leq 0. \tag{4.15}$$

Taking the equal sign in (4.15) one gets the expression for the critical value of γ when the system switches from the locked to the unlocked state (delocking) corresponding to points A and C in Fig. 4.3. It is possible to solve the fifth-degree algebraic Eq. (4.15) numerically to find the solutions. In the next section, the prediction for the critical values of γ following from this equation is compared with results of direct numerical simulations of Eqs. (4.3). It will be shown that, depending on the parameters, Eq. (4.15) may have two physically relevant solutions, which determine the delocking points. This implies that the two fluxon chains remain locked at either very small or very large values of bias current, whereas they are delocked at an intermediate current range.

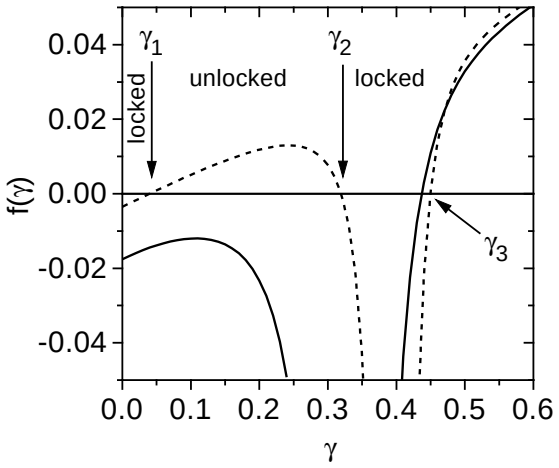

Figure 4.4: Typical behavior of the function $f(\gamma)$ (4.15). Continuous curve: strong coupling with $\Delta = 0.5$ (1 root), no delocking region. Dashed curve: weak coupling with $\Delta = 0.1$ (3 roots), delocking region is present. Other parameters: $\alpha^A = 0.12$, $\alpha^B = 0.1$, $N = 3$

4.4 Results

I have performed a series of simulations for different fluxon densities (with $N = 3, 5$, and 10 trapped fluxons in a $L = 5$ length annular junction), different coupling strengths ($\Delta = 0.1, 0.2, 0.3, 0.5$), and various ratios of the damping coefficients α^A/α^B in the two junctions (from 1 up to 1.5). The data has been acquired numerically according to the procedure described in Sec. 4.1 and then compared to results from the numerical solution of Eq. (4.15).

According to the theoretical treatment, the delocking points A and C can be regarded as zeros of the function $f(\gamma)$, defined as the l.h.s. of (4.15). Fig. 4.4 shows a typical behavior of the function $f(\gamma)$ for weak ($\Delta = 0.1$) and strong ($\Delta = 0.5$) coupling. One can see that $f(\gamma)$ has either 1 or 3 roots. The range of γ, where $f(\gamma) < 0$, corresponds to the locked state, while the region between the first two roots (for $\Delta = 0.1$) corresponds to the delocked chains. The function $f(\gamma)$ also has a third root, which corresponds to the delocking at very high γ. This root is not relevant because the dense fluxon chain approximation does not work very close to the top of the flux-flow step. Indeed, due to the relativistic contraction, the fluxon size reduces and the chain becomes sparse. As a result the numerical simulations show poor agreement between the top of the step obtained numerically and the value given by the third root of $f(\gamma)$. The numerically obtained locking range is much wider than it is predicted by the third root of $f(\gamma)$. If the coupling Δ is large enough, the function $f(\gamma)$ has only one root, which corresponds to completely locked fluxon chains at all values of γ.

The simulation results for $N = 3$ are shown in Fig. 4.5. The analytical curves for the same parameter set are shown in this figure as well. Excellent agreement between the analytical curves and the simulations for both delocking points is found. The simulated and analytical data for the case $N = 5$ are displayed in Fig. 4.6, which shows good agreement as well. One can note that for α^A/α^B close to 1.5 and large γ a

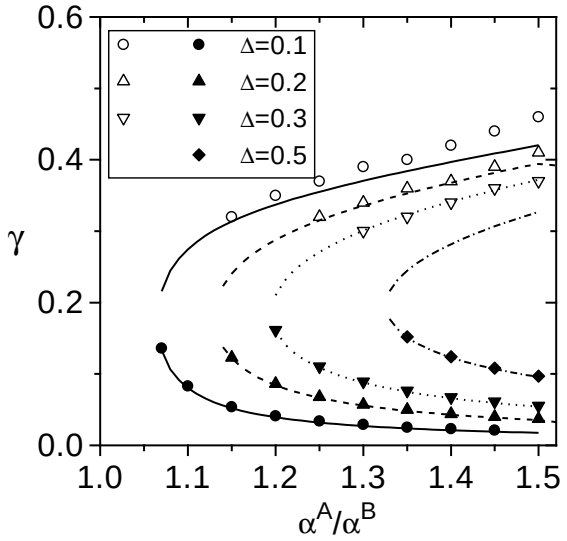

Figure 4.5: Numerically found dependence of delocking points on the ratio of the damping parameters α^A/α^B for different coupling strengths (symbols), and comparison with analytical prediction (curves). Each junction contains $N = 3$ fluxons.

small deviation of the analytical model from the simulation results takes place. This results from the fact that the fluxon chains are not very dense in this region due to relativistic contraction of the fluxon size. In any case, simulations give a wider locked region than the analytical model.

For $N = 10$ and relatively high damping parameters $\alpha \geq 0.1$ the flux–flow resonances reach the relativistic limiting velocity only at normalized bias currents $\gamma \geq 1.0$. This situation is physically irrelevant because the fluxon dynamics cease to exist at current densities above the critical current density j_c of the junction. Moreover, the adequate model to describe the high bias range should include the surface losses (β–term).

4.4.1 Critical value of coupling parameter

Using equation (4.15), one can find a critical value of the coupling parameter $\Delta^\star$ [Gol] so that the junctions never delock for a given set of damping parameters, if $\Delta > \Delta^\star$. In this case, the function $f(\gamma)$ defined above [as the l.h.s of Eq. (4.15)] has only one root (see Fig. 4.4). If $\Delta < \Delta^\star$, a delocking region exists,

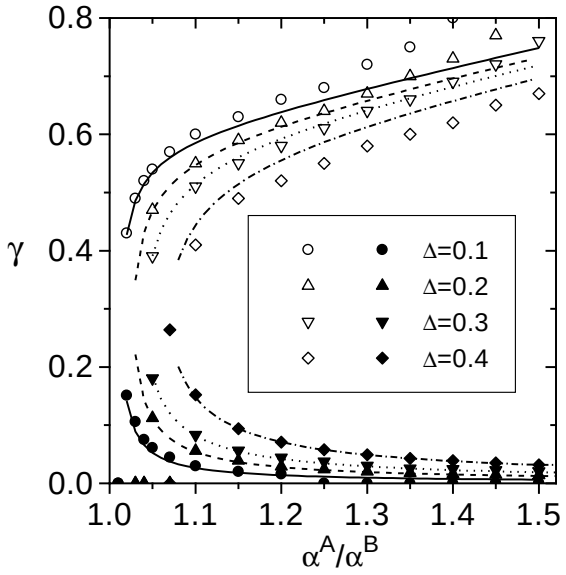

Figure 4.6: The same as in Fig. 4.5 but for $N = 5$.

and $f(\gamma)$ has 3 roots (see Fig. 4.4). At $\Delta = \Delta^\star$ the two smallest roots coincide, so that, at some value of $\gamma = \gamma^\star$, $f(\gamma^\star) = 0$ and $f'(\gamma^\star) = 0$ simultaneously. Solving these equations, one obtains the following relation for the critical coupling parameter:

$$\Delta^\star\sqrt{1+\Delta^\star} = \frac{16}{125}\sqrt{5}H^3|\alpha^A - \alpha^B| \approx 0.286H^3|\alpha^A - \alpha^B| \,. \tag{4.16}$$

Using Eqs. (4.16), one can easily evaluate the minimum value of the coupling parameter $\Delta^\star$ required to avoid delocking in the system for given values of α^A, α^B and magnetic field (fluxon density) H. Since the locking range in numerical simulations is wider than the one found from theory, the junctions should always be phase locked at $\Delta > \Delta^\star$.

4.5 Proposal for an experiment

The key to an experimental investigation of the phase locking of two magnetically coupled stacked Josephson junctions is the possibility to measure the dc voltage across each junction separately. This requires an electrical contact to the middle (common) electrode of the stack. Reliably working stacks of this kind are difficult to fabricate due to technological reasons. Recently N. Thyssen succeeded in fabricating first annular twofold stacked samples with contacts to all electrodes. Preliminary measurements of these structures are presented in chapter 5. The quality and parameters of the junctions produced so far do not allow yet for the quantitative investigation of the effects described in this chapter.

4.6 Conclusion

In this chapter it is demonstrated that Eq. (4.15) derived by B. Malomed and E. Goldobin using perturbation theory yields a very good approximation for the two delocking points on the I-V curves of two magnetically coupled annular Josephson junctions. Thus it is possible to estimate the phase locked region of a twofold stack depending on the parameters of the individual Josephson junctions comprising the stack. The acquired results are useful, when designing stacked flux–flow oscillators that are to operate as radiation sources in a coherent mode. Moreover, it seems to be possible to investigate similar locking/delocking problems, e.g. for differences in parameters other than α, with a similar approach.

Chapter 5

Experiments with annular long Josephson junctions

The first measurements of soliton dynamics in annular long Josephson junctions [DDKP85] have been successfully conducted already in 1985. Recently this type of junctions has again stimulated a lot of experimental, theoretical and numerical work. Annular junctions are favorable in comparison to linear junctions, if fluxon dynamics are to be observed without any disturbing influence from interaction with the boundaries. The annular junction is frequently used as a model system for long linear junctions in flux–flow mode. This approach was also used in chapters 3 and 4 of this work.

Here I present the first ever measurements of *stacked* annular Josephson junctions with trapped fluxons. As an introduction, measurements of single layer annular junctions are discussed. Then the main concepts of the investigation of fluxons in annular Josephson junction stacks are pointed out and first measurement results are presented.

5.1 Single junctions

Single annular Josephson junctions have regained increased interest recently [Ust96, UT96, MM96, MSM96, VKT$^+$96, KVL$^+$96, LDL$^+$95], because trapping of fluxons in high quality junctions became possible. Therefore a number of effects involving measurements of fluxon steps in this type of junctions were investigated in detail. In this section annular junctions produced by N. Thyssen at KFA are characterized and trapping of fluxons is presented.

5.1.1 Geometry

A number of annular Josephson junctions of different dimensions were examined. All junctions measured originate from the same wafer, hence they have very similar electrical properties.

The thicknesses of the superconducting and isolating layers, which determine the dynamic properties of the junctions, are defined in the fabrication process (see appendix A). The thicknesses determined from gauged sputtering rates are $d_b = 105\,\mathrm{nm}$ for the bottom superconducting niobium electrode, $d_i = 5\,\mathrm{nm}$ for the Al/AlO$_x$ tunnel barrier layer and $d_t = 155\,\mathrm{nm}$ for the top superconducting niobium electrode (see Fig. 5.1b). Junctions of two different planar dimensions were examined. Their geometries are determined by the inner and outer diameters D_i, D_o (see Fig. 5.1a) from which, the width $W = (D_o - D_i)/2$, and the area $A = \pi(D_o^2 - D_i^2)/4$ of the junctions can be calculated. The dimensions of the junctions are given in Tab. 5.1.

To analyze the dynamics of a fluxon propagating in an annular junction of finite width it is crucial to know its effective length L_{eff}. The effective lengths is one of the parameters that determine the asymptotic voltage of the fluxon step. One might guess that the effective length $L_k = 2\pi r_k$ is determined by the inner r_i, the outer r_o, the middle r_m or some other effective radius r_{eff} of the junction. This question

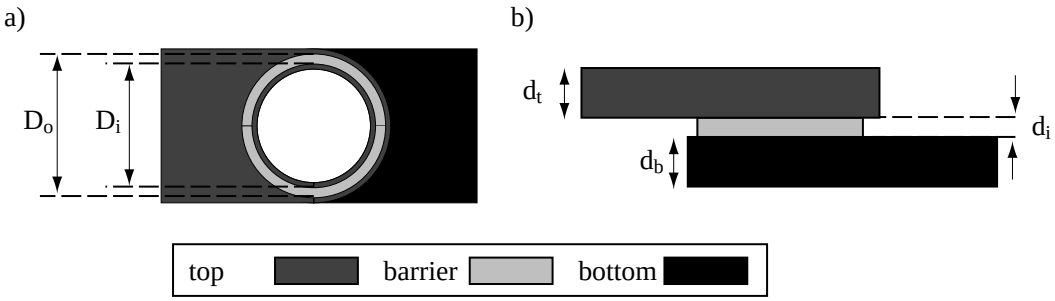

Figure 5.1: Single junction geometry in top (a) and side (b) view.

Table 5.1: Annular junction dimensions

chip/junction	D_i/μm	D_o/μm	L_m/μm	d/μm	A/cm^2
ANN1.1.1.1/BL	122	142	415	10	$5.15\,10^{-5}$
ANN1.1.1.1/TR	185	195	597	5	$2.98\,10^{-5}$

is important as can be seen in Fig. 5.2, where I plotted the IV curve of a ZFS in a 200 μm long linear junction in comparison to a fluxon step in the junction *ANN1.1.1.1/BL*. The fluxon step voltage scale was normalized to the linear junction step voltage as

$$V_{\mathrm{norm}} = \frac{L}{L_i} V \ , \tag{5.1}$$

taking into account L_i, L_m or L_o respectively. As one can see the differences are substantial.

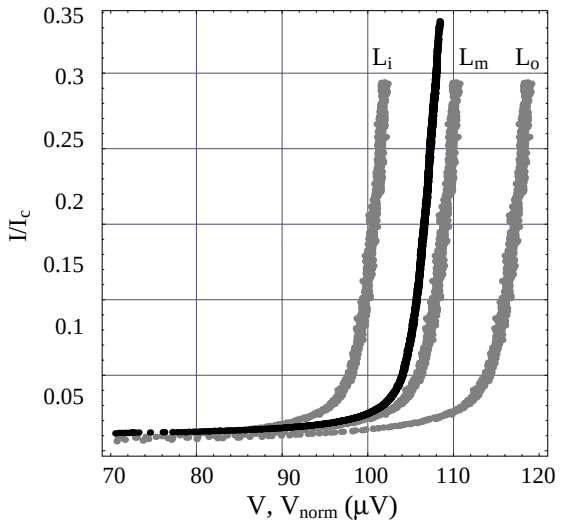

Figure 5.2: Measured IV curve of linear junction (black dots) and of small annular junction *ANN1.1.1.1/BL* (gray dots). The current is normalized to the individual junction critical current. Annular junction voltages are normalized with respect to their effective lengths L_i, L_m and L_o.

Currently the question of the effective radius is addressed experimentally and theoretically in a joint work [KWTU] of our group with V. Kurin. In this investigation the two–dimensional sine–Gordon equation is solved in cylindrical coordinates using a perturbation approach to find the effective length. The analytical result has been compared to measurements of linear and annular junctions of different dimensions [KWTU] and suggests, that $L_m = 2\pi r_m$ is a rather good approximation to L_{eff}. Therefore L_m is used as the effective length for the rest of this chapter. A more detailed discussion including the full perturbation expression for L_{eff} will be published elsewhere.

5.1.2 Junction Parameters

In this section the characteristic parameters of the junction *ANN1.1.1.1/BL* mentioned in Tab.5.1 are pointed out. The measurements were conducted with the larger junction *ANN1.1.1.1/TR* as well and showed only minor quantitative differences which originate from the size of the junction.

Electrical parameters

From the dc current voltage characteristics (Fig. 5.3) of the junction *ANN1.1.1.1/BL* the basic parameters j_c (critical current density), V_g (gap voltage) and R_n (normal resistance) can be determined. The measure-

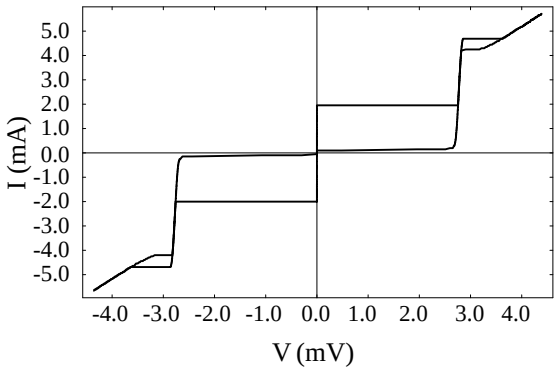

Figure 5.3: IV curve of junction *ANN1.1.1.1/BL* at $T = 4.2$ K with no flux trapped

ments were performed at liquid helium temperature ($T = 4.2$ K). All electrical quantities stated below have to be understood as approximate. The true values of certain parameters, e.g. the critical current, can only be estimated, in spite of the very accurate experimental measurements, as explained later. They are presented to get an idea about the characteristic quantities of typical junctions. In quantitative measurements, more attention has to be taken to estimate statistical and systematic errors. The above quantities are approximately related by

$$V_g = I_c R_n \; . \tag{5.2}$$

Drawing the resistive line into Fig. 5.3 one can determine the resistance of the junction from the slope to

$$R_n \approx 0.76\,\Omega \; . \tag{5.3}$$

The intersection of the resistive line with the rising current at the gap, can be used to define the gap voltage

$$V_g \approx 2.81\,\mathrm{mV} \; . \tag{5.4}$$

The critical current density of a Josephson junction is defined as the maximum zero voltage current density. In extended junctions, like the annular one examined here, self field effects [BP82, VDT81] may suppress the maximum zero voltage current. Therefore the critical current of the junctions is commonly estimated from the current rise ΔI_g at the gap voltage, as defined in Fig. 5.4. The effective critical current of the junction is estimated from the relation,

$$I_c^{eff} = \chi\, \Delta I_g \;\; , \tag{5.5}$$

where $\chi \approx 0.7$. From an experimental point of view, the determination of the true critical current density using a small junction, not affected by self field effects, on the same chip would have been favorable. Unfortunately this possibility was not provided on our chips with annular junctions. The critical current density for *ANN1.1.1.1/BL* determined from Eq. (5.5) with $\chi = 0.7$ is

$$j_c \approx 57\,\mathrm{Acm}^{-2} \; . \tag{5.6}$$

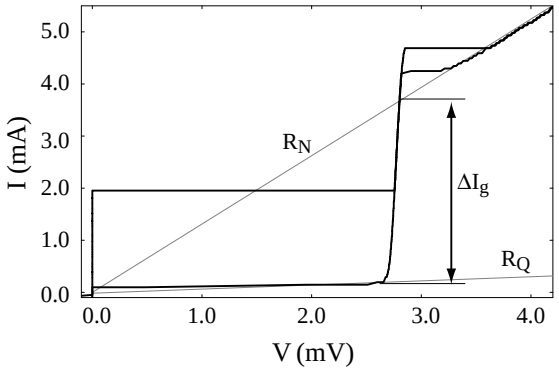

Figure 5.4: IV curve of junction *ANN1.1.1.1/BL*. Gray curves are indicating respectively the normal (R_N) and sub–gap resistance (R_Q).

Using the actual layer thicknesses and the London penetration depth $\lambda_L \approx 90\,\mathrm{nm}$ at 4.2 K, the Josephson length λ_J and the normalized length $\ell = L_{eff}/\lambda_J$ of the junction can be calculated:

$$\lambda_J \approx 47\,\mu\mathrm{m} \tag{5.7}$$

$$\ell \approx 8.8\,. \tag{5.8}$$

Junction homogeneity

The homogeneity of an extended Josephson junction can be judged qualitatively by analyzing the dependence of the critical current on the externally applied magnetic field. The pattern reflects the geometry of the junction and the current distribution within the junction in a very sensitive but complex way.[1] If the pattern is symmetric with respect to both polarities of the critical current and the magnetic field, the magnetic field penetrates symmetrically with respect to the middle of the junction. The $I_c(H)$ pattern of the junction *ANN1.1.1.1/BL* is presented in Fig. 5.5. In this and in all subsequent $I_c(H)$ measurements the magnetic field was applied in parallel to the wiring of the junction as indicated in the inset of Fig. 5.5. Also a coil current of $I_H = 1$ mA corresponds to a field of $H = 0.4$ gauss in all measurements. The pattern is very symmetric and regular, hence the junction can be considered as almost ideally homogeneous. A detailed study of $I_c(H)$ patterns in annular junctions was recently published in [MMS, MM96].

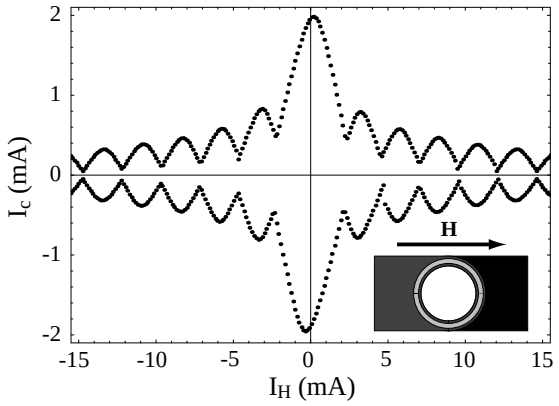

Figure 5.5: $I_c(H)$ pattern of junction *ANN1.1.1.1/BL* for both polarities of the applied external magnetic field and the critical current. $I_H = 1$ mA corresponds to $H = 0.4$ gauss. The direction of the applied magnetic field with respect to the leads is shown in the inset.

[1] A good introduction to the calculation and interpretation of $I_c(H)$ patterns can be found in chapters 4 and 5 of [BP82] or in [Lik86].

5.1.3 Fluxon steps

The dynamics of fluxons in annular junctions can be observed, by introducing a given number N of fluxons into the junction, and subsequently measuring the current–voltage characteristics of the system.

Flux trapping

Trapping of fluxons was achieved by applying a small bias current to the junction above the critical temperature T_c and then slowly cooling it down to the superconducting state. Empirically we found that the bias current is to be chosen such that the voltage drop across the junction in the normal state is of the order of the voltage drop of the flux–flow step to be observed in the superconducting state. A variety of other flux trapping mechanism is used by other groups, e.g. locally heating up the junction with an electron microscope in an applied magnetic field [UDH$^+$92], or by cooling the junction through the superconducting phase transition with a magnetic field generated by an on–chip superconducting coil [VOU92].

Characteristics of a single fluxon step

When a number of fluxons is trapped and a small bias current is applied, the fluxons move under the influence of the Lorentz force and a finite voltage drop across the junction can be observed. Ideally, the zero voltage critical current is expected to be suppressed completely due to the absence of boundaries, if some fluxons are trapped in the junction. The small residual zero voltage critical current depends on the homogeneity of the junction. Such a critical current can be seen for the first fluxon step $V_{FF}^{(1)}$ of the junction *ANN1.1.1.1/BL* shown in Fig. 5.6.

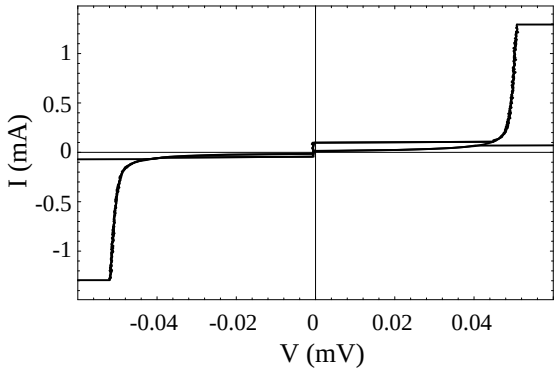

Figure 5.6: IV curve of the one fluxon resonance in the junction *ANN1.1.1.1/BL* at $T = 4.2$ K.

The shape of the fluxon step in the IV characteristic is with good accuracy determined, by its limiting voltage $V_{FF}^{(1)}$, related to the Swihart velocity, and the damping parameters α and β according to the PSGE

$$\phi_{\bar{x}\bar{x}} - \phi_{\bar{t}\bar{t}} = \sin\phi + \alpha\phi_{\bar{t}} - \beta\phi_{\bar{x}\bar{x}\bar{t}} - \gamma\,, \tag{5.9}$$

which describes well the fluxon dynamics in the junction. Using the perturbation theory for sine–Gordon systems developed by McLaughlin and Scott [MS78] the above damping parameters can be determined from the experimentally acquired data. In [MS78] it is assumed that the fluxon shape remains unaltered and only its velocity changes under the influence of the perturbative bias and damping terms. According to [DDKP85], the dependence of the normalized fluxon velocity u on the normalized bias current γ can be determined as

$$\gamma = \frac{4\alpha}{\pi}\frac{u}{\sqrt{1-u^2}}\left[1 + \frac{\beta}{3\alpha}\left(1 + \frac{u^2}{1-u^2}\right)\right] \tag{5.10}$$

using standard perturbation theory. Here α is the usual constant related to the quasiparticle tunneling and β is the damping coefficient caused by surface currents in the electrodes. The dynamic parameters of the

system can be determined by fitting the data to Eq. (5.10). The actual currents and voltages are related to γ and u by

$$I = \gamma I_c \,, \tag{5.11}$$
$$V = u V_{FF} \,. \tag{5.12}$$

To fit the experimental data to Eq. (5.10) it is convenient to plot I_c^2/I^2 vs. $1/V^2$, because in the case of $\beta = 0$ the quasiparticle damping term α can be directly extracted from the linear slope of the data. The β term is important at high velocities of the fluxon and determines the curvature of the characteristic in this representation. More details on the fitting procedure can be found in the original paper [DDKP85]. The fitted data is shown in Fig. 5.7. The fit parameters are

$$V_{FF}^{(1)} = 50.08\,\mu\mathrm{V}\,,$$
$$\alpha = 0.014\,,$$
$$\beta = 0.007\,.$$

Apparently the dynamics of the fluxon is well modeled by Eq. (5.10).

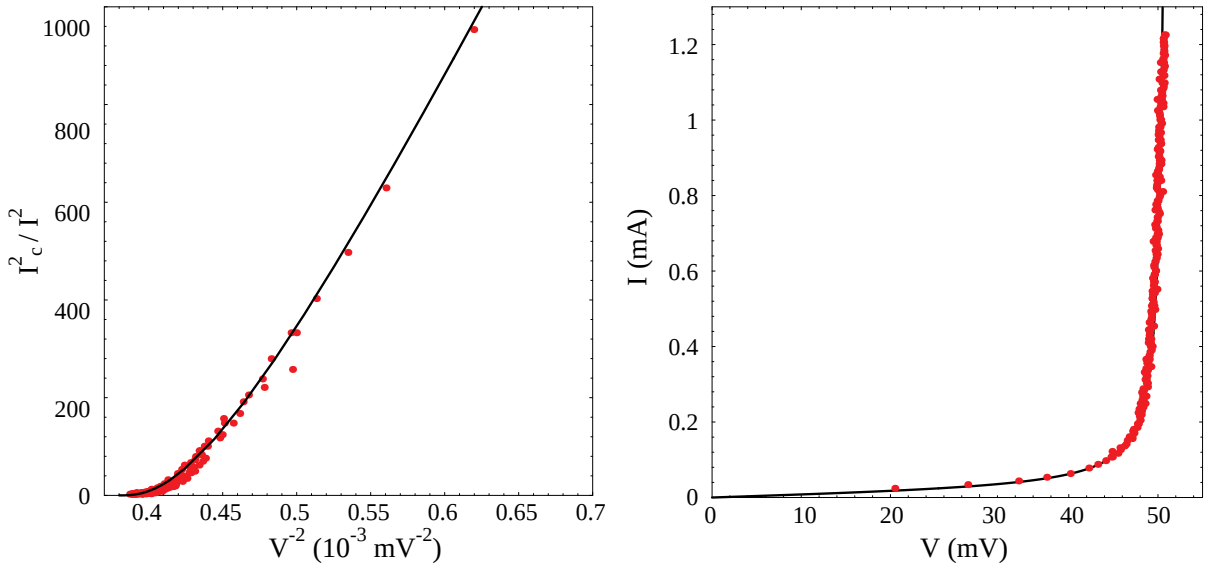

Figure 5.7: Single fluxon IV curve of junction *ANN1.1.1.1/BL* fitted with Eq. (5.10). Plot a) shows data (points) and the fitted function (solid line) according to the normalization I_c^2/I^2 vs. $1/V^2$. Plot b) shows the fluxon step in real coordinates.

From the parameters quoted above some basic junction properties can be determined. The specific capacitance C^* can be found from the equation for the resonant voltage of the step

$$V_{FF}^{(N)} = \Phi_0 N \frac{c_S}{L} \,, \tag{5.13}$$

with the Swihart velocity given by Eq. (2.10)

$$c_S = \frac{1}{\sqrt{\mu_0 C^* d'}} \,. \tag{5.14}$$

The subgap resistivity R^* of the quasiparticle tunnel current is determined by the equation for the damping term (2.14)

$$\alpha = \frac{\sigma}{\sqrt{\frac{2e}{\hbar} j_c C^*}} \,. \tag{5.15}$$

The results are

$$\begin{aligned} C^* &\approx 3.7\,\mu\mathrm{Fcm}^{-2}\,, \\ R^* &\approx 8.1\,\Omega\,, \end{aligned}$$

which are within the parameter range typically found for the long Josephson junctions fabricated in our laboratory. The value of R^* corresponds reasonably well to the quasiparticle resistance extracted directly from the sub–gap part of the IV characteristic in Fig. 5.4. C^* is slightly smaller than for typical junctions (see [SUK+94]), which is probably due to the low j_c of the junction *ANN1.1.1.1/BL*. The evaluation of flux-flow limiting voltages is a common way to measure the capacitance of a superconducting tunnel structure, which is otherwise hard to determine from geometrical and dielectric properties of the junction. Alternative methods to find the specific capacitance of Nb-Al/AlO_x-Nb interfaces are discussed in [MANK95] and [vdZROK94].

Additionally the single fluxon state can be identified analyzing the $I_c(H)$ pattern of the junction in this state. In comparison to the empty junction (Fig. 5.5), the pattern in Fig. 5.8 displays a distinct minimum with a cusp at $H = 0$. These effects are discussed in more detail in [VKT+96, KVL+96].

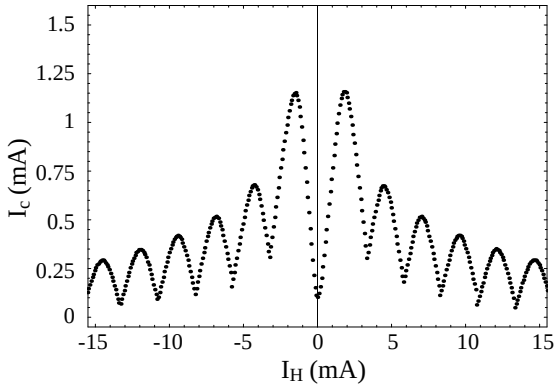

Figure 5.8: $I_c(H)$ pattern of junction *ANN1.1.1.1/BL* with one trapped fluxon for both polarities of the applied external magnetic field. $I_H = 1$ mA corresponds to $H = 0.4$ gauss.

Characteristics of multi fluxon steps

Higher order fluxon steps were observed as well. These states can be reached by applying larger bias currents to the junction during the trapping procedure. The resonant steps for 1, 2, 3, 4, and 5 trapped fluxons are shown Fig. 5.9. The asymptotic voltages of the higher order steps are to a good accuracy exact multiples of the one fluxon step as indicated by the vertical lines in Fig 5.9.

For a larger number of fluxons the perturbation analysis of the the flux–flow steps has to be extended using the exact multi–fluxon solution of the finite sine–Gordon system as zeroth order approximate solutions to the PSGE. The perturbation analysis has been carried out by Marcus and Imry [MI80] using the multi–fluxon solutions presented in the classic paper by Kulik [Kul67]. An application of this theory is demonstrated in [UDH+92], where the correction of the mistake in Eq. (2) of [UDH+92] leads to a good agreement between experiment and theory (see Sec. 3.3.1).

The main difference between the single fluxon characteristics and the multi-fluxon characteristics is that the effective damping per fluxon may decrease in the multi–fluxon case. This can be inferred as well from the flux-flow steps measured in the junction *ANN1.1.1.1/BL*. In Fig. 5.10 the voltages are plotted normalized to the number of fluxons in the junction. Moreover, fine structure appears on the flux–flow steps at higher fluxon densities, which is an indication of the mutual interaction between fluxons in the junction. Under certain conditions fluxons can form various bunched states with slightly different voltages at a given bias current [VLS+96].

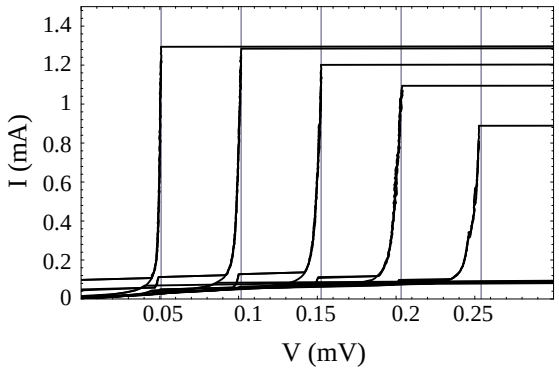

Figure 5.9: IV curve of junction *ANN1.1.1.1/BL* with 1 to 5 trapped fluxons. Multiples of first fluxon step are indicated by vertical lines.

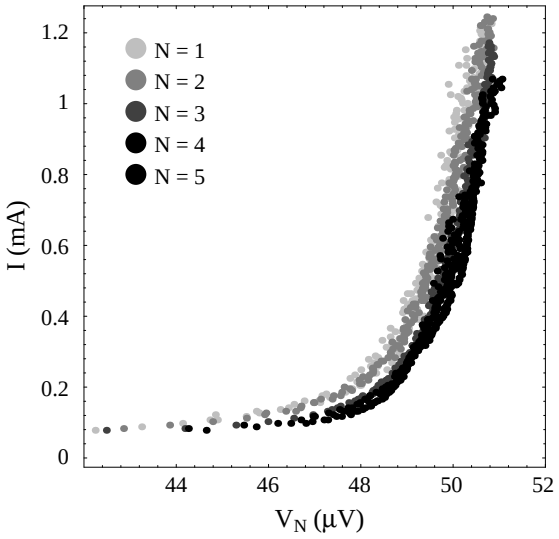

Figure 5.10: Superimposed IV curves of junction *ANN1.1.1.1/BL* with N fluxons enclosed. The voltages are normalized by N.

The $I_c(H)$ patterns measured for a larger number N of trapped fluxons show an increase in width of the suppressed critical current region at $H \approx 0$ with N. This feature can be explained by the subsequent trapping of fluxons in the applied external potential. This issue is discussed in detail in [VKT+96], who used similar junctions fabricated in our group. In this way the $I_c(H)$ patterns can also be used to identify states with different numbers of trapped fluxons indirectly. Further analysis of these patterns of annular junctions is currently in progress in other groups [MMS, MM96].

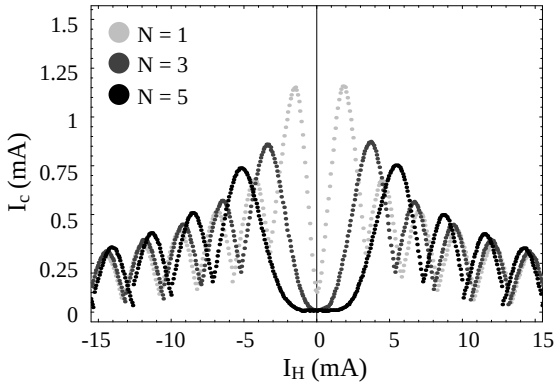

Figure 5.11: $I_c(H)$ pattern of junction *ANN1.1.1.1/BL* with 1, 3 and 5 trapped fluxon for both polarities of the applied external magnetic field. $I_H = 1$ mA corresponds to $H = 0.4$ gauss.

5.2 Stacked annular junctions

First measurements of fluxon steps in twofold stacked annular Josephson junctions are presented in this section. The main purpose of this work is devoted to advance the understanding of the phase locking in coupled long Josephson junctions. Therefore it is helpful to examine a simple system, like an annular junction, in detail. One crucial requirement is the possibility to measure voltage drops across individual junctions separately. Annular stacks that do not provide this possibility have been found more difficult to measure reproducibly in flux–flow states and to interpret the results.

5.2.1 Layout and measurement technique

A set of junctions was designed in a way such that contacts to the middle electrode could be realized. A somewhat simplified picture of the layout is presented in Fig. 5.12. In Fig. 5.12a one annular junction with a diameter of about 150 μm is shown. The bias and voltage contacts are indicated appropriately for later reference.

The top and bottom layers are designed in a standard fashion to provide a sufficiently homogeneous bias current flow through the junction. Three small ($\approx 5\,\mu$m wide) leads are connected to the middle electrode for voltage measurements. These leads can not be used for homogeneously biasing the junction since they inherently produce an inhomogeneous current distribution in the layer. Different junctions with larger leads were produced as well, but were not found working yet due to technological problems. In Fig. 5.12b an enlarged view of the junction is shown. The effective junction area is indicated by the light gray ring common to both the top and bottom tunnel barriers.

The main challenge in the fabrication performed by N. Thyssen at KFA was to guarantee a good electrical contact to the thin (< 90 nm) middle electrode. A sufficiently good contact has been realized by placing the first electrode into a small ‘basin’ etched into the thermally oxidized silicon wafer, to facilitate planar deposition of the middle electrode and its leads (also see Fig. 5.13). This particular feature of the junction might be the reason for some of the peculiarities in the IV characteristics, of the fluxon steps presented later. Therefore better solutions to realize this type of design are still under investigation. Details on the particular fabrication issues relevant for these samples will be presented elsewhere [Thyb].

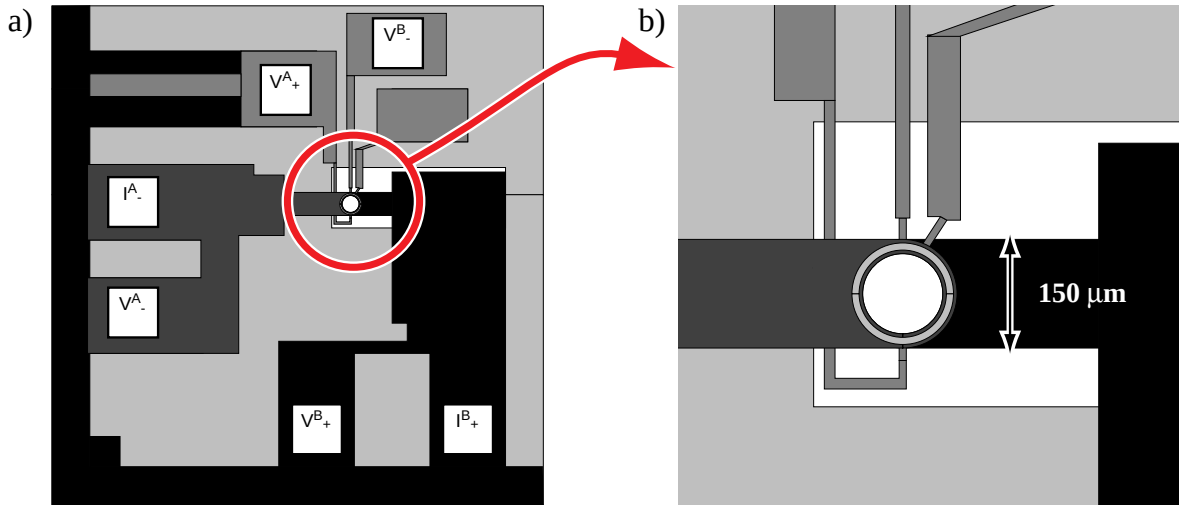

Figure 5.12: Layout of a twofold annular stack with contacts to the middle electrode. a) Full top view of junction including contact pads. The bias and voltage points are marked by white rectangles and labeled appropriately. b) Enlarged view of the junction area. Superconductor (S) layers are tinted according to: bottom layer (black), middle layer (light grey), top layer (dark grey).

5.2.2 Planar and vertical dimensions

So far one twofold stacked junction showed acceptable measurement results. The inner and outer diameters are given by $D_i = 122\mu\mathrm{m}$ and $D_o = 142\mu\mathrm{m}$, respectively. Thus the ring has a comparatively large width of $W = 10\,\mu\mathrm{m}$. Junctions with smaller widths showed characteristics which were of much lower quality than the wide junction characteristics from the point of view of junction homogeneity and spread in parameters between individual junctions of the stack. A probable explanation for this observation is, that the proper alignment of masks during the fabrication procedure is more critical for narrow rings, particularly taking into account the multiple lithography processes needed for fabricating stacks with middle contact.

The thicknesses of the multi–layer system are given according to Fig. 5.13. Again, the thicknesses were estimated from the typical sputtering rates during fabrication and thus are only accurate within approximately ±15%.

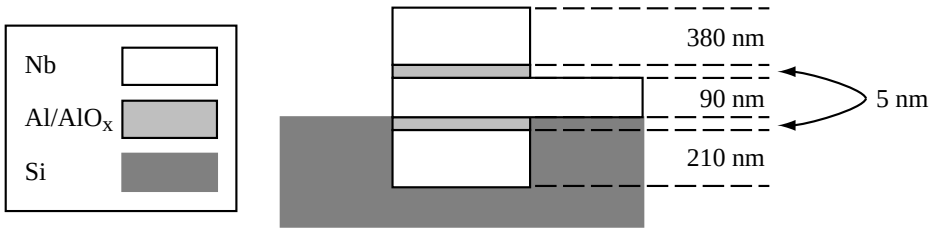

Figure 5.13: Vertical cut through the annular junction in the region of contact to the middle electrode. The layer thicknesses are indicated. The bottom electrode is placed into a basin etched into the oxidized Si wafer (dark gray).

5.2.3 Junction characteristics

In this section the characteristics of the stack without any trapped vortices are investigated.

Characteristics of the stack

In Fig. 5.14 a full IV curve of the twofold annular stack with contact to the middle electrode is shown. The dimensions are quoted above. The junction is current biased between bottom and top electrodes (I_+^B, I_-^A) and the voltage is measured across the whole stack (V_+^B, V_-^A) as indicated in Fig. 5.12a. The IV characteristic presented is very symmetric with respect to the polarity of the current. Individual junction critical currents coincide within a few percent. The curve at the first gap ($V \approx 2.6$ mV) was measured, when the weaker junction was switched to the resistive branch. From Fig. 5.14 the critical current density and the normal resistance of the stack can be estimated:

$$j_c \approx 200\,\mathrm{Acm}^{-2}\,, \tag{5.16}$$

$$R_N \approx 0.4\,\Omega\,. \tag{5.17}$$

It is worth noting that for these junctions the "knee feature" discussed in Sec. 1.4, is much less pronounced than in other samples. This indicates, that the aluminium layer in the barrier, which is causing the knee feature through the proximity effect, is smaller than in any other sample examined. Other modifications in the fabrication process, leading to changes in the tunneling characteristics, may not be excluded neither, because a new sputtering machine was employed.

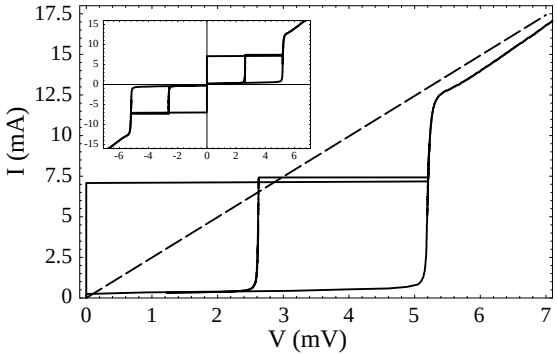

Figure 5.14: IV curve of the twofold annular stack at $T = 4.2$ K for positive bias currents. The normal resistance is indicated by a dashed line. In the inset the full IV curve is shown for both polarities of the current.

In Fig. 5.15 the $I_c(H)$ pattern of the stack biased as described before is displayed. It shows a pronounced maximum at $I_H = 0$ and is very symmetric with respect to the bias current and field polarities.

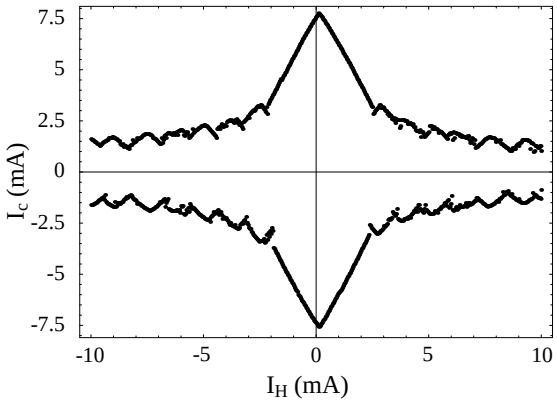

Figure 5.15: $I_c(H)$ pattern of the stack for both polarities of current and magnetic field. $I_H = 1$ mA corresponds to $H = 0.4$ gauss.

Individual junction characteristics

In a second set of measurements the stack was again biased in series (I_+^B, I_-^A), but voltages were measured individually for the bottom (V_+^B, V_-^B) and the top (V_+^A, V_-^A) junction (see Fig. 5.12). Using the available computerized measurement setup the voltage drops across both junctions could be measured simultaneously. The two IV curves are plotted vs. the bias current in Fig. 5.16. In comparison to Fig. 5.14 I observed exactly identical critical currents of the top and bottom junctions. This can be explained by the current locking phenomenon [NKH92, NEB94, YFTH94], which makes both junctions switch to higher voltages simultaneously, as soon as one junction reaches its critical current. A small difference between the gap voltages of the two junctions is observed. This indicates the difference between the junction parameters.

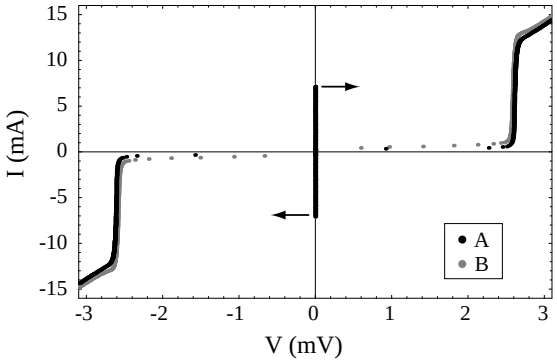

Figure 5.16: Simultaneously measured IV curves for voltages across top (A) and bottom (B) junction.

In Fig. 5.17 the $I_c(H)$ pattern of the top junction is shown, when the voltage is measured only across the junction itself. Again the typical pattern is observed, but additionally some differences from the single junction pattern are observed. Apparently, at some values of the external field, which are always larger than a certain threshold, the critical current is substantially enhanced. This situation corresponds to the case, when the second junction is switched to the resistive branch. A more detailed analysis of this phenomenon still needs to be done.

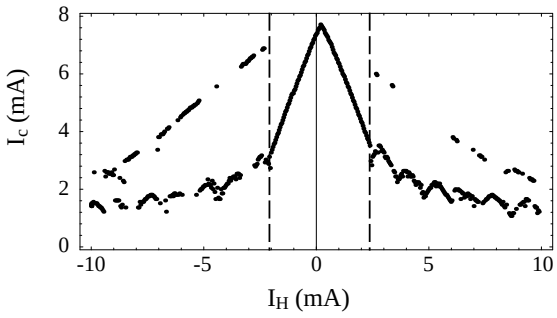

Figure 5.17: $I_c(H)$ of top junction (A). Dashed lines approximate the first critical field of the junction. $I_H = 1$ mA corresponds to $H = 0.4$ gauss.

5.2.4 Characteristics with trapped fluxons

The characteristics of the twofold annular stack without any trapped flux were presented in the previous section. In this section controlled trapping of flux is demonstrated and fluxon steps in the stack are shown.

Trapping of fluxons

Trapping of fluxons was performed in a fashion similar to the one already described in Sec. 5.1.3. The stack was current biased between the top and bottom electrodes and the voltage drops across each junction were monitored individually using two oscilloscopes. Applying a small bias current to the stack above its critical temperature T_c and then cooling down the sample resulted in combinations of n fluxons being trapped in the top and m fluxons being trapped in the bottom junction. I label these states according to $(n|m)$. Any states up to $(n|m) = (3|3)$ could be prepared reproducibly. The main difficulty was to prepare such states without any parasitic flux being trapped in the superconducting electrodes, which would destroy the homogeneous fluxon dynamics. The number of trapped fluxons was inferred from the voltage drop across each junction. The values of n and m were influenced by the applied current in the resistive state of the junction above T_c upon trapping, as discussed already in Sec. 5.1.3.

Measurements

The $(1|0)$ state. In Fig. 5.18, the individual IV characteristics of both junctions in the configuration $(1|0)$ are shown at $T = 4.2$ K. The acquired step in the top junction is stable and has a large height of about 50% of the full junction critical current. In junction A a large residual critical current ($I_c^A \neq 0$) due to pinning is observed. The pinning might be induced by the leads to the common electrode or by some other inhomogeneity of the junction. A splitting of the fluxon step into two branches, i.e. the in–phase and the out–of–phase like modes was not observed at this or any higher temperature T. A possible explanation is that the junctions in the stack are coupled at an intermediate strength of $S \approx -0.35$, as calculated from the layer thicknesses and λ_L according to Eq. (2.51). In prior experiments with linear junctions the in–phase mode has only been observed at either much lower or much higher values of the coupling parameter $|S|$.[2]

As another important feature we observe that the two junctions switch simultaneously, i.e. at the same maximum bias current, to the McCumber branch, one from $V = 0$ and the other from the fluxon step (see Fig. 5.18a). As in comparison to the $(0|0)$ configuration, the critical current of the bottom junction is reduced by the existence of a fluxon in junction A. This is an interesting feature that deserves further study in the future. To get a consistent picture of the $(1|0)$ state of the system the dependence of the critical current on the magnetic field was measured also. The pattern is shown in Fig. 5.18b, where a pronounced minimum is observed for junction A and a maximum for junction B near $I_H = 0$. The slight shift of the pattern in the positive direction of the coil current I_H is most probably due to some self field induced by the currents flowing through the bias leads of the junction. Similarly, as the $I_c(H)$ patterns for single annular junctions could be related to the number of trapped fluxons (see Sec. 5.1.3), the pattern observed here strengthens the interpretation of the step observed in Fig. 5.18a as a single fluxon step. As observed before in Fig. 5.18b some data points deviate from the main pattern. This can be interpreted in terms of the other junction being switched to the McCumber branch or remaining in the zero voltage state. This results in two different patterns for the system being in two different states.

The fluxon step has also been investigated at higher temperatures, at which the critical current is decreased and the damping of the fluxon motion is increased. Frequently dynamic states of a long junction become more stable and can be investigated easier in these conditions, still no in–phase branch could be observed. Instead an additional feature appeared on the step at higher temperatures, as discussed in the next paragraph.

The $(1|1)$–state at different temperatures. The current voltage characteristics of the stacked annular junction were measured in the $(1|1)$ state at different temperatures. The main goal was to observe the two phase locked modes corresponding to in–phase and out–of–phase motion of fluxons in the twofold stack. As in the $(1|0)$ state, no clear indication of the existence of the two distinct modes was found in

[2]Recently new ideas about the interaction of coupled junctions in the $(0|1)$ or similar asymmetric modes are discussed in our group. New types of modes related to Cherenkov–radiation being induced in the stack have been observed experimentally and numerically. Possibly the existence of in–phase type modes in these systems has to be reevaluated.

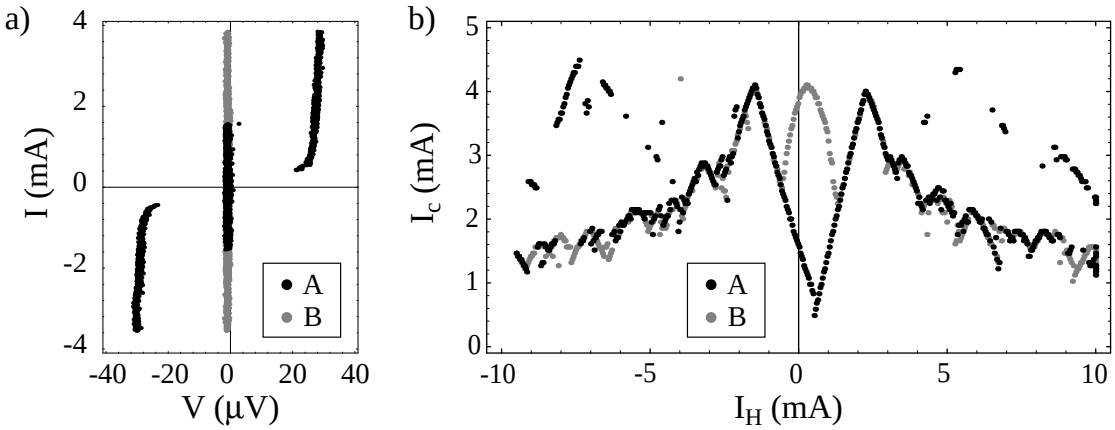

Figure 5.18: a) Separate IV curves of the junctions comprising the stack in the $(1|0)$ state. b) $I_c(H)$ pattern in the same configuration. $I_H = 1$ mA corresponds to $H = 0.4$ gauss.

this system. The $(1|1)$ fluxon step at $T_0 = 4.2$ K is shown in Fig. 5.19. The characteristics of the two junctions coincide within the accuracy $(\pm 0.2\ \mu\mathrm{V})$ of our measurement setup. Identical fine structure of the IV curve and identical switching currents suggest that the two junctions are in a frequency locked state. The actual phase relation between fluxons in both junctions could possibly be verified performing measurements of the radiation emitted by the stack. In such a measurement the fundamental frequency is expected at less than 12 GHz, according to the limiting voltage of the observed fluxon step. In this frequency range conventional off-chip detection techniques can be used. We believe that the observed mode is the out–of–phase one, which is the genuinely stable configuration of fluxons in twofold stacks. This assumption is also supported by the fact that the asymptotic voltage of the step is considerably smaller than that of the fluxon step measured for the single junction of the same dimensions in Sec. 5.1.3.[3]

At higher temperatures ($T > 4.2$ K) a peculiar "knee" feature, indicated by arrows in Fig. 5.19, appeared in the IV characteristics. This step was measured at $T_1 = 6.2\mathrm{K}$. The temperature was determined from the measured gap voltage using a phenomenological approximation [Lin93, She66] to the temperature dependence of the gap parameter in BCS theory. The gap voltages at the two temperatures are compared in Fig. 5.20. The origin of this step was investigated by systematically changing T and the externally applied magnetic field H.

The dependence of the size and position of the "knee" on T and H suggested that this feature is probably induced by a geometry–determined non–uniformity of the junction. In particular the application of an additional external magnetic field resulted in an enhancement of the "knee" feature. Similar properties have recently been observed in single annular junctions subject to an externally applied magnetic field H [Ust96, UT96]. In these experiments H was applied in the plane of the junction area. The origin of the step was attributed to the interaction of the fluxon with the sinusoidal potential induced by the magnetic field. Theoretical models and numerical simulations were proven to explain position and size of the "knee" feature adequately.

Since we observed the very pronounced "knee" features in our sample without any applied external field we attribute its existence to a periodic potential related to the intrinsic structure of the junction. Two possible origins for this potential can be suggested:

- The current leads connected to the middle electrode could serve as a pinning potential for the fluxon motion.

- The bottom electrode is sunk into the silicon wafer. Therefore the fluxon moving in the ring faces a

[3]To further clarify the identity of the step comparative measurements with single junctions on the same chip were tried. As a matter of fact all single layer junctions did not allow measurements of stable fluxon steps. I believe that this is mainly due to the fact that the junctions are embedded in the wafer, and thus the homogeneity of the junction is disturbed.

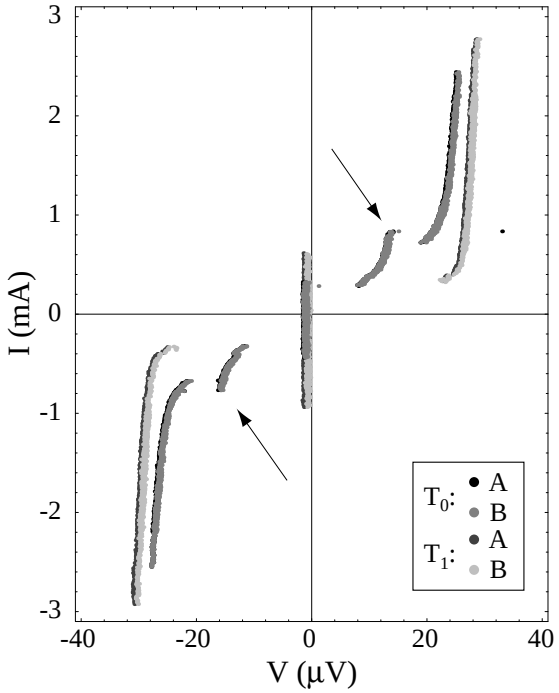

Figure 5.19: Phase locked state for 1 fluxon trapped in each junction at low and higher temperature.

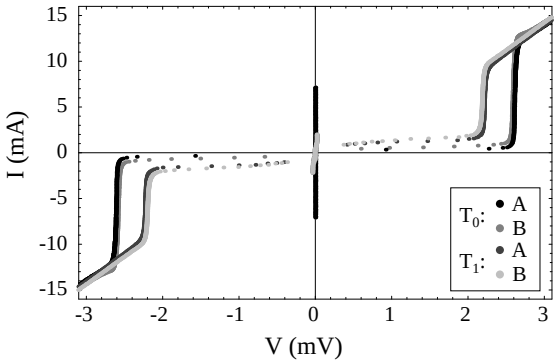

Figure 5.20: Full IV curves at $T_0 = 4.2$ K and $T_1 = 6.2$ K. T was determined from the temperature dependence of the gap voltage.

SiO_x environment during one half–cycle and a Nb environment during the other half–cycle.

Both effects could be likely reasons for the "knee" feature observed. Another indication for the potential hypothesis is the large residual critical current observed in the case of trapped fluxons in both junctions. In an ideal junction an infinitely small bias current would set the junction into a finite voltage state. Therefore one can claim that in this junction the fluxons are pinned by a potential at low bias currents.

5.2.5 Conclusions

Twofold long Josephson stacks with contact to the middle electrode have been successfully tested. Individual junction voltages were measured. Taking advantage of this possibility, a more detailed and reproducible analysis of fluxon states in annular stacks became feasible.

The splitting of fluxon modes in a single ring into two fluxon resonances in the twofold stacked rings was not observed at the coupling parameter ($S = -0.3$) predetermined by the S layer thicknesses of the junction prepared. I attribute the fluxon steps observed in the stack to the c_-–mode. At temperatures above $T = 4.2$ K a pronounced knee structure appeared on the fluxon step. This feature is ascribed to the interaction of the fluxon with a periodic potential in the ring. The potential can be related to a periodic inhomogeneity of the junction, that is due to the technique employed to fabricate the stack with contacts to the middle electrode.

Several technological issues have to be addressed in more detail to allow for further investigations.

- The fabrication methods have to be modified in order to construct a sample that is spatially homogeneous and still provides for the opportunity to measure voltages of single junctions in the stack.
- The thickness of the middle electrode has to be either increased or decreased systematically to investigate the influence of the coupling strengths on the modes of the system.

As soon as the work on these issues advances, a better understanding of phase–locking and fluxon states in stacked Josephson structures will become possible.

Summary and prospects

In the course of this diploma thesis the dynamics of solitons in stacked long Josephson junctions have been examined numerically and experimentally. Especially the application feasibility of stacked junctions as radiation sources was investigated. The Sakai–Bodin–Pedersen model [SBP93] was discussed and extended to take into account coupled oscillators with spread in parameters. The influence of different resistances and critical currents of two long junctions comprising a stack was analyzed in detail using numerical simulations.

To perform the simulations, a C–program capable of modeling one–dimensional electrodynamics in single and stacked long Josephson junctions has been developed. Particularly implemented were quantitatively accurate methods for analyzing the space and time dependent fields in the junctions by means of Fourier analysis. Special windowing techniques were used to investigate the characteristic radiation spectra of periodic voltage signals with good amplitude and frequency resolution. Techniques to automatically analyze the calculated spectra, i.e. extracting amplitudes and frequencies, have been developed as well. The program is capable of simulating most relevant features of fluxon motion in long junctions of annular and linear geometry, such that it finds applications in a number of related projects. In particular, it is used to interpret experimental data and to compare analytical calculations of the PSGE system with direct numerical simulations.

In the simulations of twofold Josephson stacks the in–phase and out–of–phase modes of fluxon motion have been examined in case of identical junctions and with spread in parameters. The spectra in both modes are explained using the concept of magnetic images induced by coupling and the phase dependent addition of Fourier components of the electromagnetic fields in the junctions. It was found that the out–of–phase mode generates radiation at the second harmonic Josephson frequency, the amplitude of which was always considerably lower than the one of a similar single junction. In contrast, the in–phase mode displayed the possibility to coherently operate the stack providing a gain in first harmonic power of slightly more than a factor of 4 over a single junction. Furthermore it was pointed out that stacked oscillators cannot generate “hyperradiance” effects as suggested in [GJB93]. Differences in parameters of the two junctions comprising the stack were analyzed, and it was noted that a spread of more than 10% leads to a crucial reduction of the locking range.

The numerical results were compared to on–chip radiation measurements of a twofold stacked long linear junction. Due to technological difficulties and electrostatic sensitivity of the circuits, only few chips were found to be operating properly. Moreover, the oscillator could not be operated in the cavity resonance–free flux–flow mode as it was intended. Still, radiation measurements revealed that in the out–of–phase mode the dominant power is emitted at the second harmonic and in the in–phase mode at the first harmonic [SUIK96], as predicted in the numerical simulations. In experiments the radiation power emitted in the in–phase mode was found to be larger than in the out–of–phase mode, in agreement with simulations. Detailed fits of the data to numerical results were not intended due to the imperfection of the samples. However, Koshelets’ group has compared their radiation measurements of a single flux–flow oscillator with our numerical results and good agreement was found [KSF$^+$97].

In conclusion, one may state that the stacked oscillator operating in the in–phase flux–flow mode does work at higher frequencies as well as higher output powers than a single junction. However, it is very sensitive to spread in parameters and thus it is a more technologically demanding task to produce well

performing devices. Nevertheless, stacked long Josephson junctions display a lot of interesting features as coupled non–linear oscillators that are worth further investigation. Very basic questions still remain open for the soliton dynamics in these systems . Moreover, intrinsically stacked high T_c superconductors as BSCCO with inherently identical junction parameters might possess interesting features with respect to their future use as multi–stacked Josephson oscillators.

In the main part of this work phase locked states of the twofold stacked Josephson oscillator were considered. An interesting dependence of the phase locked range on the coupling strength, the fluxon density and the spread in damping parameters was observed and stimulated a more detailed numerical and theoretical investigation. The locking range in bias current was determined numerically and compared to a theoretical model using a collective coordinate approach. Excellent agreement between numerical and theoretical results was found and better understanding of the phase locking mechanism in stacks with a spread in parameters was gained. Moreover, this method can be extended to examine the influence of the spread in other parameters.

Stacked annular Josephson junctions with contact to the middle electrode providing the opportunity to determine individual junction voltages were measured for the first time. This type of measurement is interesting to investigate soliton dynamics in the most simple stacked system. Trapping of fluxons in various configurations and measurements of individual junction voltages have been achieved. However, the homogeneity of junctions produced so far was insufficient to perform measurements of undisturbed fluxon motion, as needed to confirm the theoretical predictions put forward in chapter 3. To improve the homogeneity of the junctions, the fabrication process, in particular the implementation of the contacts to the middle electrode, has to be improved.

Our advances on the experimental investigation of stacked annular Josephson junctions are to be presented at the 1997 spring–conference of the German Physical Society (DPG) in Münster. The theoretical and experimental investigation of the effective length of annular Josephson junctions with finite width is currently in progress. This issue is of fundamental importance when interpreting measurements of fluxon dynamics in annular junctions, as briefly mentioned in chapter 5. Results of this work will also be presented at the DPG spring–conference.

Publications and contributions to conferences

- Numerical analysis of the coherent radiation emission by two stacked Josephson flux–flow oscillators
  A. Wallraff, E. Goldobin, and A.V. Ustinov
  Journal of Applied Physics, **80**(11):6523–6535, 1996
  This work has also been presented at the "1996 Spring–Conference of the German Physical Society, Regensburg, Germany" and at the "Applied Superconductivity Conference (ASC) 96, Pittsburgh, USA".

- Delocking of flux–flow states in dc–driven magnetically coupled Josephson junctions
  E. Goldobin, A. Wallraff, B.A. Malomed and A.V. Ustinov
  Physics Letters A, **224**(3):191–195, 1997

- Effective length of annular long Josephson junctions with finite width: theory and experiment.
  A. Wallraff, V.V. Kurin, N. Thyssen, and A.V. Ustinov
  1997 Spring–Conference of the German Physical Society, Münster, Germany

- Fluxon dynamics in annular Josephson junctions under the influence of a field–induced potential.
  N. Thyssen, A. Wallraff, and A.V. Ustinov
  1997 Spring–Conference of the German Physical Society, Münster, Germany

Appendix A

Fabrication of Josephson junctions

In this appendix the basic fabrication technique for stacked Josephson tunnel junctions based on Nb–Al/AlO_x–Nb technology is reviewed very briefly. Some references covering fabrication issues in more detail are given.

All single long junctions and twofold stacks of annular and linear geometry were fabricated by N. Thyssen at KFA. N. Thyssen also prepared twofold stacked junctions with electrical contact to the common electrode, measurements of which are discussed in Sec. 5.2. Designs and layouts of these junctions were done by A. Ustinov. The twofold stacks with on–chip detector were fabricated by N. Iosad at KFA, based on a design by S. Shitov and A. Ustinov.

A.1 Stacked junctions

As an example for the general fabrication methods employed I discuss the preparation of a single twofold long Josephson stack. Slightly modified techniques are employed for fabrication of the more complicated junctions with contact to the common electrode and the on-chip detector samples.

The stacked long Josephson junctions used in this work are produced using the well established and reliable Nb–Al/AlO_x–Nb technology [KHN+97]. All junctions are fabricated on thermally oxidized silicon wafers. Each wafer typically carries 9 chips with up to 4 junctions on each chip. The fabrication method described subsequently is very similar to the SNAP (selective niobium anodization process) discussed in [HG85]. In a first step the Si wafer is coated with a thin film (about $1.5\ \mu\mathrm{m}$) of photo resist (PR). The structure defining the ground plane of the junction is transferred from the mask 1 (see Fig. A.1.1) to the PR using photolithography. After development of the PR the first Nb–Al/AlO_x–Nb trilayer is deposited on the wafer using sputtering techniques [MH87]. During the sputter process first a poly-crystalline Nb layer of several $100\ \mathrm{nm}$ is deposited. Next the aluminum layer is sputtered and subsequently oxidized in a oxygen atmosphere within the sputter chamber, to form the tunnel barrier. Typically the Al layer is about $3-5\ \mathrm{nm}$ thick, a fraction of which ($2-3\ \mathrm{nm}$) is oxidized to AlO_x. Properties of the aluminiumoxide layer crucially determine the junction characteristics, like critical current density, quasiparticle resistivity and specific capacity. The second junction (or any number of subsequent junctions) is formed by repeating Al sputtering, oxidization and niobium deposition. In Fig. A.2a a cross-section through the junction area at this stage of fabrication is shown. After deposition of all layers a lift-off [YKN87], removing the five layer system from the parts of the wafer covered with photoresist, is performed.

In a second photolithographic process, the effective junction area is defined by covering it with PR according to mask 2 (see Fig. A.1.2) and reactively etching through the layers until the bottom AlO_x layer is reached. This step is visualized in Fig. A.2b. The edges of the stacked structure are then electrically passivated by anodic oxidization [KGS91], where Nb_2O_3 and Al_2O_3 are grown from the bottom Nb–Al/AlO_x layers as indicated in Fig. A.2c. At the end of this step the PR is again removed. In the final lithographic step the current leads are defined according to mask 3 by depositing a final (wiring) layer of Nb (see Fig. A.2d) and performing a lift-off.

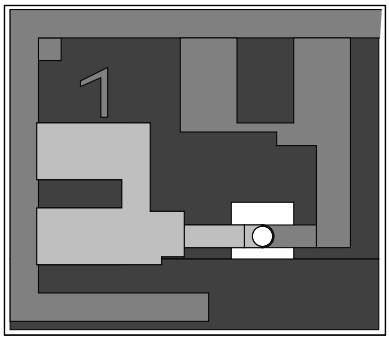

(0) masks combined in sequence (2), (1), (3)

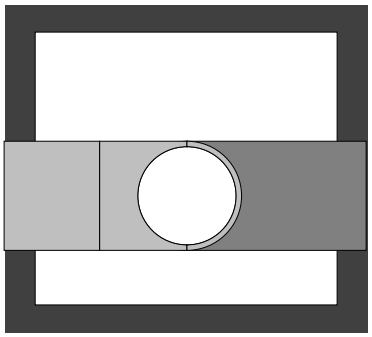

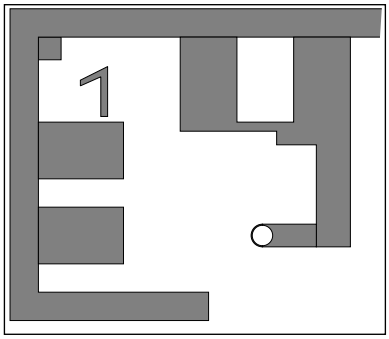

(1) ground plane mask

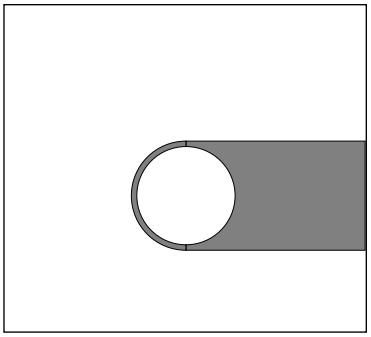

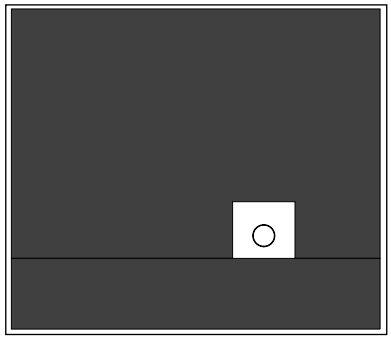

(2) etching mask

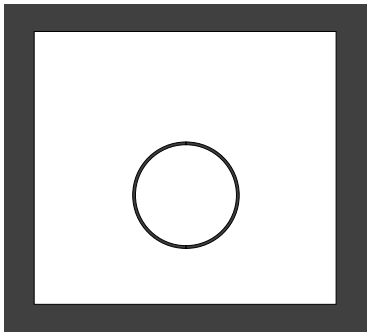

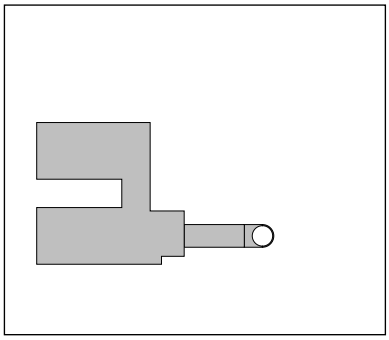

(3) wiring mask

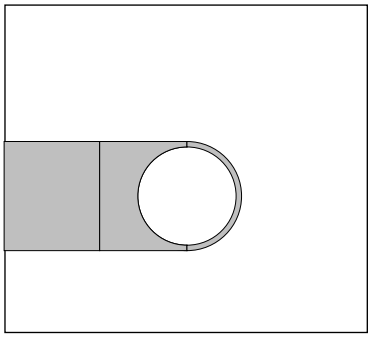

Figure A.1: Masks for photolithography of a twofold stacked annular long Josephson junction, left hand side showing the junction with contact pads, right hand side an enlarged view of the junction area. The real diameter of the junction is $D \approx 200\,\mu\mathrm{m}$

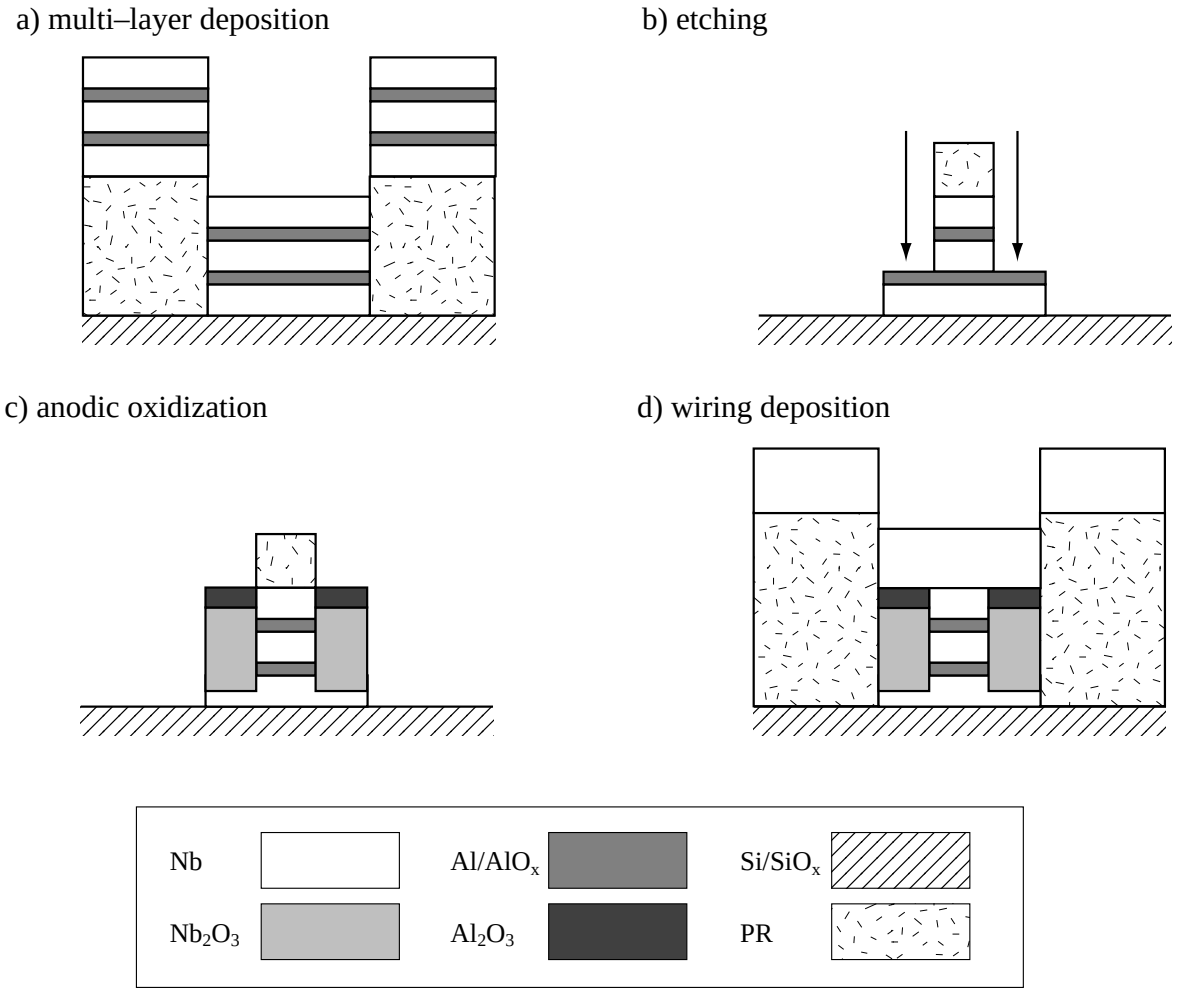

Figure A.2: Selected fabrication steps of a twofold Josephson stack (cross-sectional view). (a) Multi–layer deposition. (b) Reactive etching. (c) Anodic oxidization. (d) Deposition of leads.

These are the basic steps in fabrication of a twofold Josephson stack. Here most methods are presented in a simplified way. To produce reliable high quality junctions a great deal of expertise and experience with technological processes is required. A more detailed discussion of fabrication issues can be found in the diploma thesis of N. Thyssen [Thya].

Generally, more complicated structures may require more intermediate lithography steps, i.e. in case of contacts with access to the middle electrode an additional photomask is required to define the lead structure for the middle electrode.

Appendix B

Discrete Fourier transforms of periodic signals

In this appendix techniques employed in the calculation of numerical Fourier transforms of time dependent periodic voltages acquired from simulations of stacked long Josephson junctions are presented. Frequency and amplitude resolution of discrete Fourier transforms (DFT) in dependence on the window function are discussed. Controlled amplitude resolution is demonstrated by usage of Gaussian window functions.

B.1 Properties of discrete Fourier transforms

Numerical Fourier transforms work on a discretely sampled set of data derived from an originally continuous signal. The phase relation of the window in time over which data of the ideally infinite signal is sampled to the signal itself is crucial when dealing with periodic signals. The sampling rate and the total sampling duration determine the resolution of the Fourier transform. These issues are discussed in this section with focus on periodic signals.

B.1.1 Data acquisition

The time dependent voltage signal is sampled discretely at time intervals of Δt. The total number of samples is N. Thus the total time of sampling is

$$T_w = N\Delta t \,, \tag{B.1}$$

i.e. the first sample is taken at $t = \Delta t$ and the last at $t = N\Delta t = T_w$. As will be discussed in Sec. B.1.3, it is crucial for the accuracy of amplitude determination during numerical Fourier transforms that the time T_w is an exact multiple of the fundamental period of the signal T_s, when no special windowing technique is used. This criterion is difficult to fulfill with data given by simulations of stacked Josephson junctions because

- the voltage is intrinsically periodic but of an initially unknown period which depends on various parameters of the system under consideration,
- the period of the signal is not known exactly, which makes it hard to get exact values of harmonic amplitudes,
- the computational effort for finding the period of the signal in runtime is larger than using a windowing technique.

Therefore I have chosen not to match the sampling window width to the period of the signal during data acquisition but to rather use a windowing technique (see Sec. B.2).

B.1.2 Resolution in time and frequency domain

The accuracy at which the signal is sampled in the time domain depends on the Δt. If Δt is small compared to the the characteristic period of the signal the resolution in the time domain is high whereas for large Δt it is low. The maximum frequency that is contained in a set of data sampled at the rate $1/\Delta t$ is called the Nyquist frequency

$$\nu_N = \nu_{max} = \frac{1}{2\Delta t} \, . \tag{B.2}$$

The minimum frequency resolved is determined by the total sampling time T through

$$\nu_{min} = \frac{1}{T} \, . \tag{B.3}$$

The frequency resolution $\Delta\nu$ is also determined by the value of $1/T$, such that the frequencies appearing in the discrete Fourier spectrum are given by

$$\nu_i = n \, \Delta\nu = n \, \nu_{min} \, . \tag{B.4}$$

The value $\Delta\nu$ is crucial for the amplitude resolution of the discrete Fourier transform.

B.1.3 Theory of the DFT

In this section I discuss in detail how a numerical Fourier transform is calculated from an originally continuous and infinite signal. Let us first consider the ideal case in which the relation $T_w = nT_s$ with $n \in N$ is fulfilled for the sampled data. If the data is supplied to the Fourier algorithm as is, it is said to be acquired with a rectangular window. Thus the waveform which is Fourier transformed is given by the product of a window function $w(t)$ and the signal function $s(t)$

$$f(t) = w(t)s(t) \, . \tag{B.5}$$

The Fourier transform of $f(t)$ is given by

$$\mathcal{F}\left\{f(t)\right\}(\omega) = \tilde{f}(\omega) = \frac{1}{\sqrt{2\pi}} \int_{-\infty}^{-\infty} f(t) \exp^{-i\omega t} \, dt = \frac{1}{\sqrt{2\pi}} \int_{-\infty}^{-\infty} w(t)s(t) \exp^{-i\omega t} \, dt \tag{B.6}$$

which can be expressed as a convolution of the two individual Fourier transforms $\tilde{w}(\omega)$ and $\tilde{s}(\omega)$

$$\mathcal{F}\{w(t)s(t)\}(\omega) = \tilde{f}(\omega) = \frac{1}{\sqrt{2\pi}} \tilde{w}(\omega) * \tilde{s}(\omega) \tag{B.7}$$

As can be seen from this equation the continuous function in frequency space generated by Fourier transforming the windowed signal $f(t)$ crucially depends on the window function $w(t)$.

Let us now consider the case of a rectangular window function $w_\square$ of width T given by

$$w_\square(t) = \beta(t)\beta(T - t) \, , \tag{B.8}$$

where β is the Heaviside function

$$\beta(t - t_0) = \begin{cases} 1 & for \quad t \geq t_0 \\ 0 & for \quad t < t_0 \end{cases} \, . \tag{B.9}$$

As an example the influence of this window function on the discrete Fourier transform of a purely sinusoidal signal

$$s_1(t) = A_1 \sin(\omega_1 t) \tag{B.10}$$

of amplitude A_1 and angular frequency ω_1 is demonstrated. The Fourier transform is given by the convolution of

$$\tilde{w}_{\square}(\omega) = \frac{1}{\sqrt{2\pi}} \exp^{-i\omega T/2} T \frac{\sin(\omega T/2)}{\omega T/2} \tag{B.11}$$

and

$$\tilde{s}_1(\omega) = \frac{1}{\sqrt{2\pi}} \frac{A_1}{2} \left(\delta(\omega - \omega_1) + \delta(\omega_1 - \omega)\right) \ , \tag{B.12}$$

i.e.

$$\mathcal{F}\{f(t)\}(\omega) = \frac{1}{\sqrt{2\pi}} \left[\frac{1}{\sqrt{2\pi}} \exp^{-i\omega T/2} T \frac{\sin(\omega T/2)}{\omega T/2}\right] * \left[\frac{1}{\sqrt{2\pi}} \frac{A_1}{2} \left(\delta(\omega - \omega_1) + \delta(\omega_1 - \omega)\right)\right] \tag{B.13}$$

This is the functional expression for the continuous Fourier transform of $f(t)$ in the frequency domain. Using numerical discrete Fourier transforms (DFT) or the fast Fourier transforms (FFT) the discrete set of values obtained are samples of the continuous FT at values of $\nu = 0, 1/T, \ldots, 1/(2\Delta t)$ with $\Delta\nu = 1/T$, where $2\pi\nu = \omega$. The discrete sampling of the transform is the source of large errors in Fourier amplitudes of periodic signals in case $T_w \neq nT_s$.

B.1.4 An example

The issues discussed in Sec. B.1.3, are illustrated by an example (see Fig. B.1). A sinusoidal signal of frequency $\nu_1 = 1\ \mathrm{s}^{-1}$ with the amplitude A_1, sampled at the rate $1/\Delta t = 16\ \mathrm{s}^{-1}$ with a rectangular window function, is considered. In subfigure (a) the situation $T_w = n\,T_s$, where $n = 4$ is shown. In this case, the continuous FT is sampled, such that the spectrum accurately consists of one peak at the frequency $\nu_1 = 1$ with the amplitude $A_1 = 1$, i.e. the discrete spectrum is identical to the analytically calculated one. Subfigure (b) displays the result for $n = 4.25$, i.e. a mismatch of a quarter of a period between the signal and the window. As a result amplitudes appear at frequencies that do not exist in the original signal. The main amplitude is decreased as compared to the ideal case. This effect is called *leakage*. In subfigure (c) the same effect is shown for the worst case $n = 4.5$, i.e. a mismatch of half a period.

The leakage error is strongly related to the shape of the window function. By choosing an appropriate function the leakage error can be controlled effectively.

B.2 Windowing

The leakage error can be substantially reduced by choosing a non rectangular window function. The window function has to be selected to suit the required needs.

B.2.1 Choosing a window function

There are two major issues to consider when choosing a window function:

- frequency resolution ,
- amplitude resolution .

These two quantities are intrinsically related to each other in a way that one cannot maximize the two independently, if the window has fixed width T. A higher frequency resolution leads to a lower amplitude resolution and vice versa.

In the harmonic analysis of fluxon oscillations, we are mainly interested in accurate amplitude resolution, whereas frequency resolution is not as crucial because periodic signals with an intrinsically large separation in harmonic components are analyzed. In the following section I will discuss one particular type of window that suits this need. There are several other window types, e.g. Parzen or Hamming windows, serving other needs discussed in literature [Ram85].

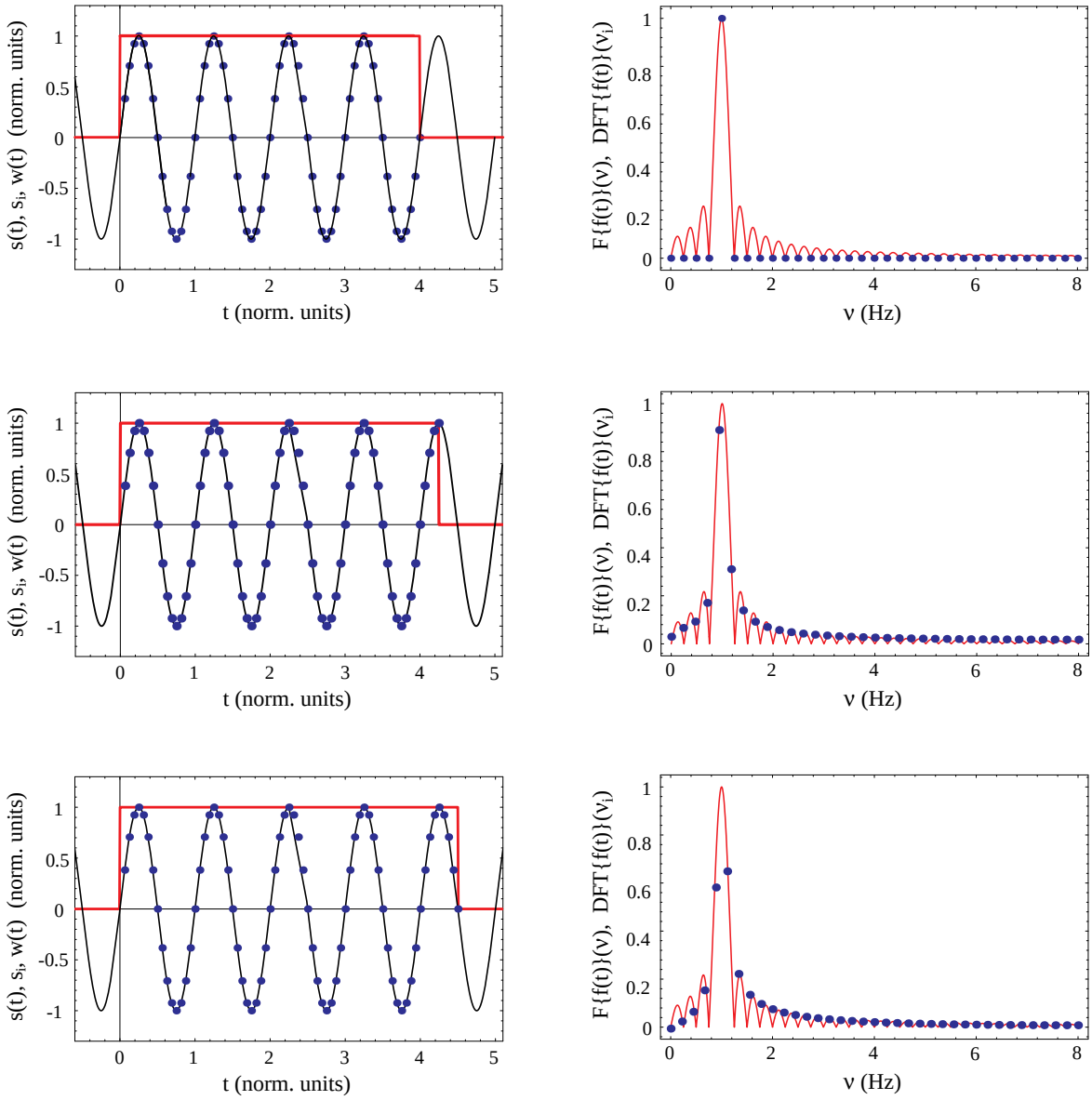

Figure B.1: On the left hand side, the continuous signal (solid line), windowed by a rectangular window function (thick line) and sampled at discrete times (dots) is shown. On the right hand side the continuous FT of the windowed signal (solid line) and the final sampled data are displayed. The rows show (a) perfect matching, (b) quarter period mismatch and (c) half period mismatch.

B.2.2 Gaussian window function

A Gaussian is a suitable function for windowing periodic data because its width can be adjusted easily in a controllable way, providing the needed accuracy in amplitude determination. A normalized Gaussian centered at t_0 with a variance of σ is given by

$$g(t) = \frac{1}{2\pi\sigma} \exp^{-\frac{1}{2}\frac{(t-t_0)^2}{\sigma^2}} \quad . \tag{B.14}$$

Its FT is

$$\tilde{g}(\omega) = \frac{1}{\sqrt{2\pi}} \exp^{i\omega t_0} \exp^{\frac{\sigma^2\omega^2}{2}} \quad . \tag{B.15}$$

The maximum error in a Fourier amplitude that can arise when using a Gaussian window function is dependent on its variance σ and its total width T. The aim is to choose σ in a way to control the relative error

$$\epsilon_{A_i} = \frac{\Delta A_i}{A_i} = \frac{A_i - A_i{}^{FFT}}{A_i} \tag{B.16}$$

through leakage, where A_i is a harmonic amplitude of the signal

$$s(t) = \sum_{i=1}^{\infty} A_i \sin(i\, 2\pi\, \nu\, t) \ . \tag{B.17}$$

Letting $t_0 = 0$, the maximum relative error in A_i that can occur is determined by the equation

$$\tilde{g}(\omega)\Big|_{\omega=\pm\frac{2\pi}{2T}} = \frac{1}{\sqrt{2\pi}} \exp^{\frac{\sigma^2}{8T^2}} \tag{B.18}$$

depending on the discretization step $\Delta\nu = 1/T$ in the frequency domain, as can be inferred from Fig. B.2. Choosing a maximum acceptable error ϵ_{A_i} one can solve the Eq. (B.18) for the required variance σ of the

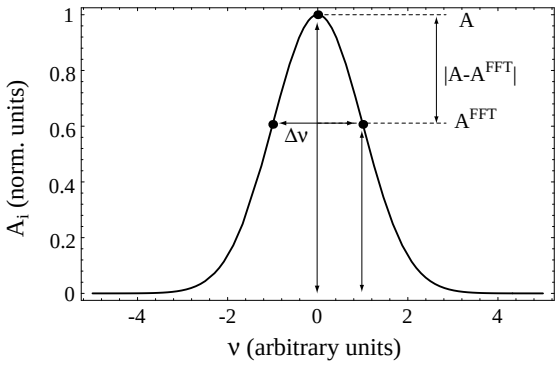

Figure B.2: Determination of the relative error ϵ_{A_i} in dependence on the discrete frequency spacing $\Delta\nu$ and the window width in frequency space.

Gaussian window function:

$$\sigma = \sqrt{\frac{2T^2}{\pi^2} \ln \frac{1}{1-\epsilon_{A_i}}} \ . \tag{B.19}$$

This function is plotted in dependence on ϵ_{A_i} in Fig. B.3.

To guarantee a maximum relative error of $\epsilon_{A_i} = 0.01$ we have to set $\sigma = 0.045$. An example of this window in time and frequency domain is given in Fig. B.4 for $T_w = 1$ and $\Delta t = 0.01$. From this plot you can see, that the FT of the window function is very wide in frequency space. The width is determined by the maximum error ϵ_{A_i} and the length of the window T_w. Thus, the Fourier components of the signal have to have a minimum frequency separation, to avoid amplitude errors through overlap of lobes

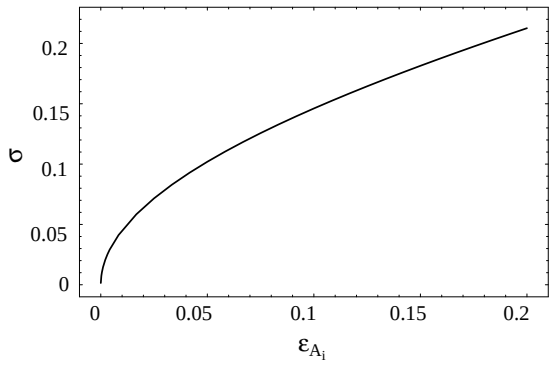

Figure B.3: Required variance σ of the Gaussian window as a function of the maximum relative error ϵ_{A_i} for $T = 1$.

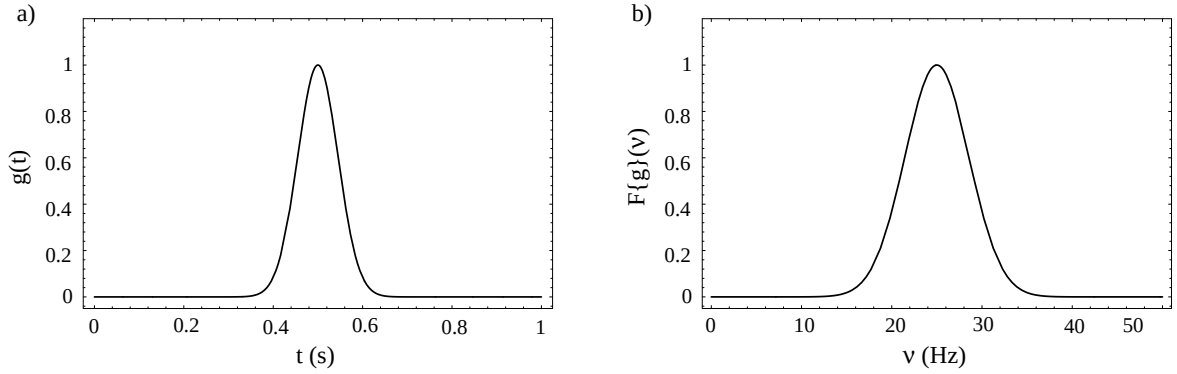

Figure B.4: Plot(a) shows the Gaussian window function for a window width of $T = 1\,\mathrm{s}$ with an amplitude normalized to 1 in the time domain. Plot (b) shows the FT of the same Gaussian function with the amplitude normalized to 1. Here $\Delta t = 0.01$ is chosen, thus $\nu_{max} = 50\,\mathrm{Hz}$. The Gaussian is arbitrarily centered at the frequency $\nu_0 = 25\,\mathrm{Hz}$.

and simultaneously allow different frequency components to be resolved. To achieve a better frequency resolution, one has to choose a bigger T_w, which will reduce the width of the window in frequency space.

As another important factor Δt has to be chosen according to the Nyquist frequency in order to include the highest relevant frequencies present in the signal. Otherwise folding of frequencies in the spectrum, better known as *aliasing*, will occur. Aliasing produces wrong components in the spectrum and may even change amplitudes of real components, when the alias and real frequency coincide.

B.3 Conclusion

When numerically Fourier transforming periodic signals, special care has to be taken in sampling the signal. Either data has to be acquired in sets of *exact* multiples of the fundamental period of the signal or windowing techniques have to be employed. Properties of the window function have to be chosen carefully according to the required amplitude and frequency resolution. Additionally the total sampling duration and the sampling rate are crucial parameters.

Appendix C

Perturbation theory

C.1 Dense fluxon chain approximation

A useful and mathematically simple approximate solution of the sine–Gordon equation can be calculated in the *dense fluxon chain approximation*. In this approximation it is assumed, that the phase in a junction essentially varies linearly with a small sinusoidal modulation in correspondence to the integral of the average magnetic field in the junction (see Fig. C.1).

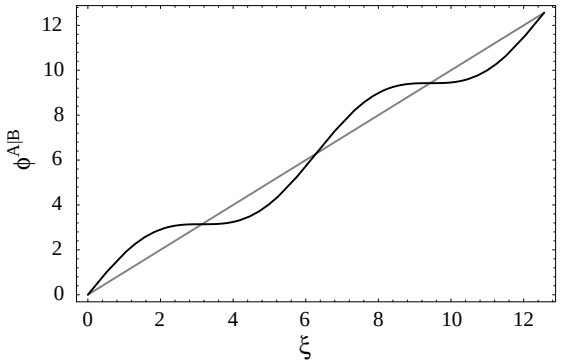

Figure C.1: Phase distribution $\phi(\xi)$ along a one-dimensional long junction in the dense fluxon chain approximation ($H = 1, \ell = 4\pi$).

C.1.1 Perturbation expansion

Mathematically an expression for the phase can be found by considering a perturbation expansion of ϕ to the first order

$$\phi = \phi^{(0)} + \phi^{(1)} \; . \tag{C.1}$$

The zeroth order term $\phi^{(0)}$ can be inferred from the boundary condition in the linear case or the average magnetic field in the junction in the annular case

$$\phi^{(0)}_{\xi} = \tilde{H} \; . \tag{C.2}$$

Neglecting integration constants $\phi^{(0)}$ is given by

$$\phi^{(0)}(\xi) = \tilde{H}\xi \; . \tag{C.3}$$

The first order term $\phi^{(1)}$ can be found by inserting the perturbation expansion (C.1) into the SGE

$$\phi_{\xi\xi} = \sin\phi \tag{C.4}$$

and expanding the sine-term for small values of $\phi^{(1)}$. Using (C.3) the equation determining $\phi^{(1)}$ is

$$\phi^{(1)}_{\xi\xi} = \sin(\tilde{H}\xi) \ . \tag{C.5}$$

By integration we find the first order perturbation expression for the phase ϕ to be

$$\phi(\xi) = \tilde{H}\xi + \frac{1}{\tilde{H}^2}\sin(\tilde{H}\xi) \ . \tag{C.6}$$

Equation C.6 is plotted vs. ξ in Fig. C.1. The approximation is valid as long as the modulation of the phase in space is sinusoidal and its amplitude is much less than the average magnetic field $\tilde{H}$. In general the range of validity of this expansion strongly depends on parameters and has to be checked carefully, for example by doing direct numerical simulations of the system under consideration.

C.1.2 Field profiles in coupled stacks with spread in critical currents

In this section I apply the dense fluxon chain approximation to the twofold stack of Josephson junctions with different critical currents but otherwise identical parameters. This approach was used to check numerical simulations, which initially produced unexpected results in the regime of different critical currents. Predictions from this analytical calculation were very different from numerical results, which stimulated a repeated checking of the simulation code. Finally a bug in a coefficient of the numerical code was found and removed. After recalculation excellent agreement between the perturbation approach and the numerical solutions were found.

Dense chain analysis

The phase profiles in each junction of a twofold stack can be calculated using the dense fluxon chain approximation. Starting from Eq. (3.1) I consider the simplified case

$$\begin{array}{rcl} \frac{1}{1-S^2}\phi^A_{\xi\xi} = & \sin\phi^A + \frac{S}{1-S^2}\phi^B_{\xi\xi} \\ \frac{1}{1-S^2}\phi^B_{\xi\xi} = & \frac{1}{J}\sin\phi^B + \frac{S}{1-S^2}\phi^A_{\xi\xi} \end{array} \ , \tag{C.7}$$

only taking into account the terms describing the coupling (S) between the junctions and the differences in critical currents given by $J = j_c^A/j_c^B$. Now I use the dense fluxon chain approximation (C.6) introducing two additional parameters A and B to take into account the different field amplitudes in each junction that are to be investigated :

$$\begin{array}{rcl} \phi^A & = & H\xi + A\sin(H\xi) \\ \phi^B & = & H\xi + B\sin(H\xi + \pi) \end{array} \ . \tag{C.8}$$

A phase shift of π between junction A and B is chosen in order to consider the out–of–phase mode, which is the stable solution at small perturbations and low bias currents.

Substituting Eqs. (C.8) into (C.7) one can solve for the unknown amplitudes A and B. After some calculation

$$\begin{array}{rcl} A & = & \frac{S-J}{JH^2} \\ B & = & \frac{1-SJ}{JH^2} \end{array} \tag{C.9}$$

are found and the ratio of the amplitudes A/B is given by

$$\left|\frac{A}{B}\right| = \frac{J-S}{1-JS} \ . \tag{C.10}$$

For single junctions ($S = 0$) the ratio of amplitudes of junctions with different critical currents is identical to J, whereas in the coupled system it is given by Eq. (C.10).

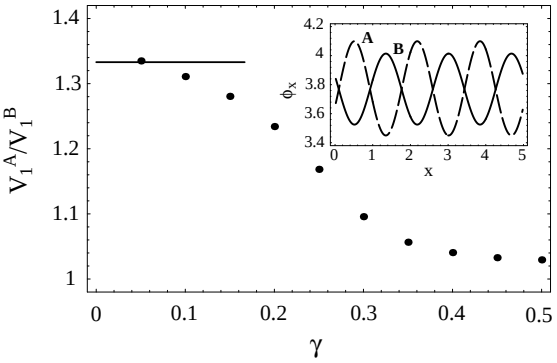

Figure C.2: V_1^A/V_1^B vs. γ for $J = 2.0$. Black line is indicating analytical result. The inset shows magnetic field profiles in junction **A** and **B** at $\gamma = 0.05$

Comparison to numerical results

The numerical results acquired for the system of equations (3.1) with $J \neq 1$ and $S = -0.4$ presented in Sec. 3.3.2 are checked against Eq. (C.10). Excellent agreement is found for low bias currents γ at all values of J. As an example V_1^A/V_1^B is plotted vs. γ for $J = 2.0$ in Fig. C.2. The result from Eq. (C.10) is plotted as a solid line. As an inset the magnetic field profile of the system is shown at $\gamma = 0.05$. The field profiles are in good approximation sinusoidal and the ratio of their amplitudes coincides with the one found from Eq. (C.10). For higher bias currents γ the calculation in the previous section is not valid any more, because the perturbation terms neglected in (C.7) become important and change the result. As can be seen from Fig. C.2 and the analysis presented in Sec. 3.3.2 the ratio V^A/V^B is approaching unity for high bias γ, i.e. when the fluxon chains approach their limiting velocity.

Appendix D

Computational aspects

D.1 Specification of simulation code “STKJJ.exe”

STKJJ.exe is a program for simulating twofold stacks of long Josephson junctions with arbitrary parameters. The program was developed by myself in collaboration with E. Goldobin. It is based on the original code by P. Bodin, who is one of the developers of the SBP model [SBP93] for magnetically coupled Josephson junctions discussed in detail in Sec. 2.3 and chapter 4. During this work the original source code for identical junctions, was extended to do analysis of stacks with spread in junction parameters. To our knowledge, STKJJ.exe is the first program developed which is capable of simulating the influence of differences in junction parameters on fluxon dynamics in a stack. In its current version STKJJ.exe can simulate most experimentally relevant quantities and moreover provides methods to analyze temporal and spatial variations of electromagnetic fields, to better understand the complex dynamics in single and stacked long Josephson junctions. Different features provided by the program are briefly discussed in Sec. D.1.3.

D.1.1 Design considerations

STKJJ.exe is designed with a commandline interface, which greatly enhances the portability of the code between different systems. Portability is an important feature, because, depending on the complexity of the task, different computer systems had to be used. The program was tested and run on PC, Apple Macintosh, IBM and HP unix workstations as well as on a CRAY supercomputer.

All input parameters are either parsed from the commandline, read from a parameter file, or in case of initial conditions read from data files. All output is written to data files either in preprocessed or unprocessed form. This mode of operation allows to conveniently run time consuming simulations in batch mode. Most data analysis is done externally, with the users software of choice.

D.1.2 Running STKJJ.exe

In unix or DOS STKJJ.exe is started from the commandline of a csh or a DOS window. In general the program is invoked by typing a string of commands of the following structure on the command line, where % is the prompt of the shell.

```
% STKJJ.exe outputfile.dat -@stdoptsfile -option:arg currentStart
currentStop currentStep
```

There are two types of arguments to STKJJ.exe, namely parameters and options. Options are arguments that are preceded by a “–” sign. All other arguments are considered as parameters. Parameters have to be specified in their proper sequence, whereas options can have arbitrary positions on the commandline. The meaning and usage of different elements on the commandline is briefly explained in the following list:

- **STKJJ.exe** : This is the call to the executable C program. It may include the full pathname, if necessary.

- ***outputfile*.dat** : This parameter specifies the name of the file to which the calculated IV curve is written. It is generated in all operation modes of the program

- ***-@stdoptsfile*** : *stdoptsfile* is the name (if necessary including the path) of a separate file that contains standard options that the user might want to specify.

- ***-options:arg*** Any number of options can be specified on the commandline directly, which is useful, if an option frequently changes between different runs of the program.

- **currentStart currentStop currentStep** : The remaining parameters at the end of each commandline specify how the bias current γ current is swept for the current run. The initial currents, end currents and current steps have to be specified sequentially according to the following order

$$\begin{array}{lll} \text{start current} & \text{stop current 1} & \text{step current 1} \\ & \text{stop current 2} & \text{step current 2} \quad . \\ & \dots & \dots \end{array}$$

  The current step has to be specified as a positive quantity. If the stop current is smaller than the start current the program will automatically change the sign of the current step.

D.1.3 Selected features of STKJJ.exe

STKJJ.exe provides a wide range of features to simulate different properties of twofold stacks of long Josephson junctions. Different modes of operation as well as input and output formatting are briefly reviewed in this section.

Geometrical and electrical properties of the stack

Before simulations can be started the parameters of the system to be investigated have to be specified for the two junctions JJ^A and JJ^B. The basic geometrical and electrical parameters are listed in Tab. D.1.

Table D.1: Basic electrical and geometrical parameters of the stack, as they have to be passed to STKJJ.exe.

`-Topology:`*`arg`*	geometry of the stack: linear ($arg = 1$), annular ($arg = 0$)
`-JJ_Length:`*`arg`*	one-dimensional length ℓ of JJ^A, specifying the physical length of the stack.
`-Alfa0:`*`arg`*	damping parameter α^A
`-Alfa1:`*`arg`*	damping parameter α^B
`-Alfa:`*`arg`*	common damping parameter $\alpha = \alpha^A = \alpha^B$
`-J:`*`arg`*	ratio of critical currents j_c^A/j_c^B
`-R:`*`arg`*	ratio of quasiparticle resistivities R^{*A}/R^{*B}
`-C:`*`arg`*	ratio of specific capacitances C^{*A}/C^{*B}
`-D:`*`arg`*	ratio of effective magnetic thicknesses d'^A/d'^B
`-L:`*`arg`*	ratio of magnetic thicknesses Λ^A/Λ^B
`-S:`*`arg`*	coupling parameter S
`-Bias0:`*`arg`*	detuning factor γ^A/γ of bias current for JJ^A
`-Bias1:`*`arg`*	detuning factor γ^B/γ of bias current for JJ^B

Current voltage characteristics

In the basic operation mode, i.e. not specifying any other options than the ones quoted in this and the previous subsection, STKJJ.exe calculates current voltage characteristics of the stack. To perform this operation some numerical parameters have to be set initially (see Tab. D.2).

Table D.2: Numerical settings.

`-dx:`*arg*	discretization in space Δx
`-dt:`*arg*	discretization in time $\Delta t = arg\,\Delta x$ relative to descretization in space
`-IV_T_Init:`*arg*	initial relaxation time before averaging of voltage is started
`-IV_T_Aver:`*arg*	initial averaging period, before averaging algorithm starts checking for accuracy of voltage
`-IV_T_Err:`*arg*	maximum acceptable difference in averaged voltage between two periods
`-IV_T_Fact:`*arg*	factor by which the averaging time is extended if minimum error is not met on the previous step
`-IV_T_Max:`*arg*	maximum period after which averaging is stopped unconditionally

Simulations can be started with an initial phase distribution in each junction according to the settings in Tab. D.3. Moreover in the linear case the boundary conditions can be fixed by specifying an externally applied magnetic field.

Table D.3: Initial and boundary conditions.

`-NFlux0:`*arg*	number of fluxons N^A in JJ^A in annular case
`-NFlux1:`*arg*	number of fluxons N^B in JJ^B in annular case
`-NFlux:`*arg*	equal number of fluxons $N = N^A = N^B$ in both junctions for annular case
`-H:`*arg*	value of normalized externally applied magnetic field $\tilde{H}$ for linear case
`-H_RF:`*arg*	value of normalized externally applied ac magnetic field for linear case
`-Omega_RF:`*arg*	frequency of externally applied ac magnetic field for linear case
`-SavedState:`*name*	starts system with initial phase distribution stored in the file *name*
`-InitCond:`*arg*	defines type of initial conditions to use: (*arg* = 1) uniform field distribution (linear phase) according to specified number of fluxons N^A and N^B; (*arg* = 2) as in *arg* = 1 but according to the value of $\tilde{H}$; (*arg* = 3) N^A, N^B fluxons localized in the center of each junction, i.e. $N^{A\|B}2\pi$ kink; (*arg* = 4) N^A, N^B fluxons distributed uniformly along respective junction junction
`-ICSpeed:`*arg*	initial velocity $arg = u$ of fluxons in both junctions
`-ICXShift0:`*arg*	shift of fluxons in JJ^A to the right by $arg = \Delta x$
`-ICXShift1:`*arg*	shift of fluxons in JJ^B to the right by $arg = \Delta x$
`-ICPS:`*arg*	shift of phase in JJ^B by $arg = \Delta\phi$ with respect to JJ^A

Space and time dependent fields

As an important feature a variety of space and time dependent fields can be calculated using STKJJ.exe. The fields are saved to separate files after the calculation of each single point of the IV curve. The appropriate options to specify are quoted in Tab. D.4. All files are saved according to naming and formatting conventions quoted in Tab. D.6.

Table D.4: Space and time dependent fields.

`-SaveState+`	saves phase distribution of both junctions for the past two time–steps to a file (filename: stat####.dat)
`-OutPhase+`	saves phases of both junctions to a file (filename: p####.dat)
`-OutVoltage+`	saves voltage of both junctions to a file (filename: v####.dat)
`-OutField+`	saves magnetic field of both junctions to a file (filename: h####.dat)

Fourier transforms

Fourier transforms performed by STKJJ.exe use a special windowing technique discussed in detail in appendix B. The FFT of the windowed data is performed using a NAG library routine. The specific options to use the FFT features of STKJJ.exe are reported in Tab. D.5.

Table D.5: Fourier transform settings.

`-MaxFreq:`*arg*	sets the Nyquist frequency for sampling $V(t)$ signals for output and FFT
`-OutVT:`*arg*	saves local voltage $V(t)$ of both junctions at *arg* time–steps with a rate determined by the Nyquist frequency to a file (filename: VT####.dat)
`-FFTWindowType:`*arg*	specify choice of window function: rectangular ($arg = 0$); Hamming ($arg = 1$); Parzen ($arg = 2$); gaussian ($arg = 3$)
`-OutFFT:`*arg*	Switches on numerical FFT of *arg* samples of the local voltage $V(t)$ of both junctions. The rate of samples in time is determined by the Nyquist frequency. Automatically evaluates spectra to find maxima. Writes spectra and maxima to files. (filenames: fft####.dat, maxx###.dat)
`-SEP+`	skips unnecessary points in FFT on output in order to save space. (filename: fftxx###.dat)

D.1.4 Output file formats

The output formats of files generated by STKJJ.exe when the appropriate options are invoked are specified in Tab. D.6. Additionally STKJJ.exe saves a copy of the commandline in the file *cmdline* and a log file in the file *stkjj.log* on each single run of the program.

Table D.6: Format of output files.

No.	file		column				
	name	phys. data	1	2	3	4	5
1	outputfile.dat	I(V)	index	γ	$< \phi^A_{\tilde{x}}(\tilde{x},\tilde{t}) >_{\tilde{x},\tilde{t}}$	$< \phi^B_{\tilde{x}}(\tilde{x},\tilde{t}) >_{\tilde{x},\tilde{t}}$	$< \tilde{t} >$
2	stat####.dat	$\phi^{0\ldots N}_{n,g}state$	ϕ^A_n	ϕ^A_g	ϕ^B_n	ϕ^B_g	-
3	p####.dat	$\phi^{A,B}(\tilde{x},\tilde{t}_0)$	$\tilde{x}$	$\phi^A(\tilde{x},\tilde{t}_0)$	$\phi^B(\tilde{x},\tilde{t}_0)$	-	-
4	h####.dat	H(x)	$\tilde{x}$	$\phi^A_{\tilde{x}}(\tilde{x},\tilde{t}_0)$	$\phi^A_{\tilde{x}}(\tilde{x},\tilde{t}_0)$	-	-
5	v####.dat	V(x)	$\tilde{x}$	$\phi^A_{\tilde{t}}(\tilde{x},\tilde{t}_0)$	$\phi^B_{\tilde{t}}(\tilde{x},\tilde{t}_0)$	-	-
6	VT####.dat	V(t)	$\tilde{t}$	$\phi^A_{\tilde{t}}(\tilde{x}_0,\tilde{t})$	$\phi^B_{\tilde{t}}(\tilde{x}_0,\tilde{t})$	$\phi^A_{\tilde{t}} + \phi^B_{\tilde{t}}$	-
7	fft####.dat	FFT	frequency	$Ampl^A$	$Ampl^B$	$Ampl^{A+B}$	-
8	fftxx###.dat	sparse FFT	frequency	$Ampl^A$	$Ampl^B$	$Ampl^{A+B}$	-
9	maxx###.dat	max(FFT)	frequency	$Ampl^A$	$Ampl^B$	$Ampl^{A+B}$	-
10	stkjj.log	log file	log of all actions and files				
11	cmdline	commandline	echo of arguments on commandline on execution				

Bibliography

[Abd94] F. Abdullaev. *Theory of Solitons in Inhomogeneous Media*. Wiley, 1994.

[AR63] J.R. Anderson and J.M. Rowell. Probable observation of the Josephson superconducting tunnel effect. *Phys. Rev. Lett.*, 10:230, 1963.

[Bar95] P. Barbara. *Fluxon dynamics in single and stacked Josephson tunnel junctions*. PhD thesis, Technical University of Denmark, Physics Department, 1995.

[BB95] P.A.A. Booij and S.P. Benz. In *Proceedings of ISEC'95*, page 513, 1995.

[BCS57] J. Bardeen, L.N. Cooper, and J.R. Schrieffer. *Phys. Rev. B*, 108:1175, 1957.

[BMP+95] P. Barabara, J. Mygind, N. F. Pedersen, G. Costabile, A. D. D'Anna, R. D. Parmentier, and Malomed B. A. In R. D. Parmentier and N. F. Pedersen, editors, *"Nonlinear Superconducting Devices and High-T_c Materials"*. World Scientific, Singapore, 1995.

[BP82] A. Barone and G. Paterno. *Physics and Applications of the Josephson Effect*. Wiley, 1982.

[BS59] N.N. Bogolubov and D.V. Shirkov. *Introduction to the theory of quantized fields*. Interscience Publishers, New York, 1959.

[BS83] N.N. Bogolubov and D.V. Shirkov. *Quantum Fields*. The Benjamin/Cummings Publishing Company, 1983.

[CPS+78] G. Costabile, R.D. Parmentier, B. Savo, D.W. McLaughlin, and A.C. Scott. Exact solution of the sine–Gordon equation describing oscillations in long (but finite) Jospehson junctions. *Appl. Phys. Lett*, 32:587, 1978.

[CPS81] M. Cirillo, R.D. Parmentier, and B. Savo. Mechanical analog studies of a perturbed sine–Gordon equation. *Physica 3D*, 18:565, 1981.

[DDKP85] A. Davidson, B. Dueholm, B. Kryger, and N.F. Pedersen. Experimental investigation of trapped sine-Gordon solitons. *Phys. Rev. Lett.*, 55(19):2059, 1985.

[DPP86] A. Davidson, N.F. Pedersen, and S. Pagano. The effect of surface losses on soliton propagation in Josephson junctions. *Appl. Phys. Lett.*, 48(19):1306, 1986.

[Fis64] M.D. Fiske. *Rev. Mod. Phys.*, 36:221, 1964.

[FLS65] R.P. Feynman, R.B. Leighton, and M. Sands. *Lectures in Physics*, volume 3. Addison-Wesley, 1965.

[GGU96] E. Goldobin, A. Golubov, and A.V. Ustionv. Twofold stacks of long Jospehson junctions with different parameters. *Czech. J. Phys.*, 46:663, 1996. LT-21 Suppl. S2.

[GHG+95] A.A. Golubov, E.P. Houwman, J.G. Gijsbertsen, V.M. Krasnov, J. Flokstra, J. B. le Grand, and P.A.J. de Korte. Proximity effect in superconductor-insulator-superconductor Josephson tunnel junctions: Theory and experiment. *Phys. Rev. B.*, 49:1073, 1995.

[Gij95] H. Gijsbertsen. *Superconducting tunnel junctions for x–ray detection*. PhD thesis, University of Twente, Netherlands, 1995.

[GJB93] N. Grønbech-Jensen and J.A. Blackburn. Hyperradiance from phase–locked soliton oscillators. *Phys. Rev. Lett.*, 70:1250, 1993.

[GJBS96] N. Grønbech-Jensen, J.A. Blackburn, and M.R. Samuelson. Phase locking between Fiske and flux–flow modes in coupled sine–Gordon systems. *Phys. Rev. B*, 53(18):12364, 1996.

[GJC94] N. Grønbech-Jensen and M. Cirillo. Phase locking of Fiske modes in sine–Gordon systems. *Phys. Rev. B*, 50(17):12851, 1994.

[GJOS93] N. Grønbech-Jensen, O.H. Olsen, and M.R. Samuelsen. Fluxons in magnetically coupled Jospehson junctions. *Phys. Lett. A*, 179:27, 1993.

[GK88] A.A. Golubov and M.Yu. Kupriyanov. Theoretical investigation of Josephson tunnel junctions with spatially inhomogeneous superconducting electrodes. *J. Low Temp. Phys.*, 70:83, 1988.

[GKU96] E. Goldobin, H. Kohlstedt, and A.V. Ustinov. Tunable phase locking of stacked Josephson flux–flow oscillators. *Appl. Phys. Lett.*, 68(2):250, 1996.

[Gol] E. Goldobin. private communication.

[GWMU96] E. Goldobin, A. Wallraff, B.A. Malomed, and A.V. Ustinov. Delocking of flux–flow states in dc–driven magnetically coupled Josephson junctions. *Phys. Lett. A*, 224(3):191, 1996. accepted for publication.

[HG85] H.A. Huggins and M. Gurvitch. Preparation and characteristics of Nb/Al-oxide/Nb tunnel junctions. *J. Appl. Phys.*, 57(6):2103, 1985.

[Jos62] J.D. Josephson. Possible new effects in superconductive tunneling. *Phys. Lett.*, 1(7):251, 1962.

[KGS91] H. Kohlstedt, K.H. Gundlach, and A. Schneider. Investigation of the tunnel barrier in Nb-based junctions prepared by sputtering and electron beam evaporation. *IEEE Transactions on magnetics*, 27(2):3149, 1991.

[KHN+97] H. Kohlstedt, G. Hallmanns, I.P. Nevirkovets, D. Guggi, and C. Heiden. Preparation and properties of Nb/Al-AlO_x/Nb multilayers. *IEEE Trans. Appl. Supercond.*, 3:1993, 2197.

[KI96] T. Kato and M. Imada. Macroscopic quantum tunneling of a fluxon in a long Jospehson junction. *J. Phys. Soc. Jpn.*, 1996. submitted 26.04.96.

[Kle94] R. Kleiner. Two-dimensional resonant modes in stacked Jospehson junctions. *Phys. Rev. B*, 50(10):6919, 1994.

[KM88] Yu.S. Kivshar and B.A. Malomed. Dynamics of fluxons in a system of coupled Josephson junctions. *Phys. Rev.B*, 37:9325, 1988.

[KM89] Y.S. Kivshar and B.A. Malomed. Dynamics of solitons in nearly integrable systems. *Rev. Mod. Phys.*, 61(4):763–915, 1989.

[KM90] S.E. Koonin and D.C. Meredith. *Computational Physics*. Addison-Wesley, 1990.

[KM94] R. Kleiner and P. Müller. *Phys. Rev. B*, 49:1327, 1994.

[KSF+96] V. P. Koshelets, S.V. Shitov, L.V. Filippenko, A.M. Baryshev, H. Golstein, T.de Graauw, W. Luinge, H. Schaeffer, and H. vandeStadt. First implementation of a superconducting integrated receiver at 450 GHz. *Appl. Phys. Lett.*, 68:1273, 1996.

[KSF+97] V.P. Koshelets, S.S. Shitov, L.V. Filippenko, A.M. Baryshev, W. Luinge, H. Golstein, H. van de Stadt, J.R. Gao, and T. de Grauw. An integrated 500 GHz receiver with superconducting local oscillator. *To be published in IEEE Trans. Appl. Supercond.*, 1997. Proceeedings of ASC 96.

[KSKM92] R. Kleiner, F. Steinmeyer, G. Kunkel, and P. Müller. *Phys. Rev. Lett.*, 68:2394, 1992.

[KSSF93] V. P. Koshelets, A. V. Shchukin, S. V. Shitov, and L. V. Filippenko. *IEEE Trans. on Appl. Supercond.*, 3:2524, 1993.

[Kul67] I.O. Kulik. Wave propagation in a Jospehson tunnel junction in the presence of vortices and the electrodynamics of weak superconductivity. *Sov. Phys. JETP*, 24:1307, 1967.

[KVL+96] S. Keil, I.V. Vernik, A. Laub, H. Preßler, R.P. Huebener, N. Thyssen, A.V. Ustinov, and H. Kohlstedt. Magnetic flux pinning in annular josephson junctions in a barrier parallel dc magnetic field. *Phys. Rev. B*, 1996. submitted.

[KWTU] V.V. Kurin, A. Wallraff, N. Thyssen, and A.V. Ustinov. Effective length of annular long Josephson junctions with finite width: theory and experiment. to be presented at DPG Frühjahrstagung 1997, Münster, Germany.

[LDL+95] A. Laub, T. Doderer, S.G. Lachenmann, R.P. Huebener, and V.A. Oboznov. Lorentz contraction of flux quanta observed in experiments with annular Josephson tunnel junctions. *Phys. Rev. Lett.*, 75(7):1372, 1995.

[lG94] J. B. le Grand. *X–ray response of superconductive tunnel junctions with trapping layers*. PhD thesis, University of Utrecht, Netherlands, 1994.

[Lik79] K.K. Likharev. Superconducting weak links. *Rev. Mod. Phys.*, 51(1):101–159, 1979. Review.

[Lik86] K.K. Likharev. *Dynamics of Jospehson Junctions and Circuits*. Gordon and Breach Science Publishers, 1986.

[Lin93] D.S. Linden. A modified two–fluid model of conductivity for superconducting surface resistance calculation. Master's thesis, MIT, USA, 1993.

[MANK95] M. Maezawa, M. Aoyagi, H. Nakagawa, and I. Kurosawa. Specific capacitance of Nb/AlO_x/Nb Josephson junctions with critical current densities in the range of 0.1–18 kA/cm^2. *Appl. Phys. Lett.*, 6(16):2134, 1995.

[McC68] D.E. McCumber. *J. Appl. Phys.*, 39:3113, 1968.

[MH87] Shin'ichi Morohashi and Shinya Hasuo. Experimental investigation and analysis for high-quality Nb/Al-AlO_x/Nb Josephson junctions. *J. Appl. Phys.*, 61(10):4835, 1987.

[MI80] P.M. Marcus and Y. Imry. Steady oscillatory states of a finite Josephson junction. *Solid State Comm.*, 33:345, 1980.

[MKS+95] J. Mygind, V.P. Koshelets, A.V. Shchukin, S.V. Shitov, and I.L. Lapitskaya. *IEEE Trans. on Appl. Supercond.*, 5:3057, 1995.

[MM96] N. Martucciello and R. Monaco. Annular josephson tunnel junctions in an external magnetic field: the statics. *Phys. Rev. B*, 53(6):3471, 1996.

[MMS] N. Martucciello, R. Monaco, and C. Soriano. Annular Jospehson tunnel junctions in external magnetic field. (preprint).

[MS78] D.W. McLaughlin and A.C. Scott. Perturbation analysis of fluxon dynamics. *Phys. Rev. A*, 18:1652, 1978.

[MSM96] N. Martucciello, C. Soriano, and R. Monaco. Annular Jospehson tunnel junctions in external magnetic field: the dynamics. *Phys. Rev. B*, 1996. submitted.

[NEB94] I.P. Nevirkovets, J.E. Evetts, and M.G. Blamire. Transition from single junction to double junction behaviour in SISIS–type Nb–based devices. *Phys. Lett. A*, 187:119, 1994.

[NEIY83] T. Nagatsuma, K. Enpuku, F. Irie, and K. Yoshida. Flux-flow type oscillator for millimeter and submillimeter wave region. *J. Appl. Phys.*, 54(6):3302, 1983.

[NEYI84] T. Nagatsuma, K. Enpuku, K. Yoshida, and F. Irie. Flux-flow type oscillator for millimeter and submillimeter wave region. ii. modeling. *J. Appl. Phys.*, 56(11):3284, 1984.

[NEYI85] T. Nagatsuma, K. Enpuku, K. Yoshida, and F. Irie. Flux-flow type oscillator for millimeter and submillimeter wave region. iii. oscillation stability. *J. Appl. Phys.*, 58(1):441, 1985.

[NKH92] I.P. Nevirkovets, H. Kohlstedt, and C. Heiden. *Cryogenics*, 32:583, 1992.

[Pag87] S. Pagano. *Nonlinear Dynamics in Long Josephson Junctions*. PhD thesis, The Technical University of Denmark, The Danish Center for Applied Mathematics and Mechanics, 1987.

[Par93] R.D. Parmentier. *The new superconducting electronics*, page 221. Kluwer, Dordrecht, 1993.

[Ped82] N.F. Pedersen. *Advances in Superconductivity*, chapter Solitons in long Josephson junctions. Plenum Press, New York, 1982.

[PJFC95] C.P. Poole Jr., H.A. Farach, and R.J. Creswick. *Superconductivity*. Academic Press, 1995.

[PPSD86] S. Pagano, N.F. Pedersen, S. Sakai, and A. Davidson. Analytical and numerical results for a long Josephson junction with surface losses. In *Proc. Appl. Sup. Conf., Baltimore*, 1986.

[PU95] N.F. Pedersen and A.V. Ustinov. Fluxons in Josephson transmission lines: new developments. *Supercond. Sci. Technol.*, 8:389, 1995. Review article.

[PUPS94] A. Petraglia, A.V. Ustinov, N.F. Pedersen, and S. Sakai. Numerical study of fluxon dynamics in a system of two–stacked Josephson junctions. *J. Appl. Phys.*, 77(3):1171, 1994.

[Ram85] R.W. Ramirez. *The FFT, fundamentals and concept*. Prentice–Hall, N.J., 1985.

[SBP93] S. Sakai, P. Bodin, and N.F. Pedersen. Fluxons in thin–film superconductor–insulator superlattices. *J.Appl.Phys.*, 73:2411, 1993.

[SCP96] C. Soriano, G. Costabile, and R.D. Parmentier. Coupling of Josephson flux–flow oscillators to an external RC load. *Supercond. Sci. and Tech.*, 9:578, 1996.

[She66] T.P. Sheahen. Rules for the energy gap and critical field of superconductors. *Phys. Rev.*, 149:368, 1966.

[Sol72] L. Solymar. *Superconductive tunneling and applications*. Chapman and Hall, London, 1972.

[SUIK96] S.V. Shitov, A.V. Ustinov, N. Iosad, and H. Kohlstedt. On-chip radiation detection from stacked Jospehson flux-flow oscillators. *J. Appl. Phys.*, 80(11), 1996.

[SUK+94] S. Sakai, A.V. Ustinov, H. Kohlstedt, A. Petraglia, and N.F. Pedersen. Theory and experiment on electromagnetic–wave–propagation velocities in stacked superconducting tunnel structures. *Phys. Rev. B*, 50(17):12905, 1994.

[Swi61] J.C. Swihart. Field solution for a thin-film superconducting strip transmission line. *J. Appl. Phys.*, 32:461, 1961.

[TF85] J.R. Tucker and M.J. Feldman. Quantum detection at millimeter wavelengths. *Rev. Mod. Phys.*, 57(4):1055–1113, 1985.

[Thya] N. Thyssen. Experimentelle Untersuchung der Josephson-Flußquantendynamik in langen Josephson-Tunnelkontakten mit elektromagnetischem Fenster. Master's thesis, Mathematisch-Naturwissenschaftliche Fakultät der RWTH-Aachen.

[Thyb] N. Thyssen. private communication.

[UDH+92] A.V. Ustinov, T. Doderer, R.P. Huebener, N.F. Pedersen, B. Mayer, and V.A. Oboznov. Dynamics of sine-Gordon solitons in the annular Josephson-junction. *Phys. Rev. Lett.*, 69(12):1815, 1992.

[UK96] A.V. Ustinov and H. Kohlstedt. Interlayer fluxon interaction in Josephson stacks. *Phys. Rev. B*, 54(9), 1996.

[UKC+93] A.V. Ustinov, H. Kohlstedt, M. Cirillo, N.F. Pedersen, G. Hallmanns, and C. Heiden. Coupled fluxon modes in stacked Nb/AlO_x/Nb long Josephson junctions. *Phys. Rev B*, 48(14):10614, 1993.

[Ust96] A.V. Ustinov. Observation of radiation induced soliton resonances in a Josephson ring. *JETP Lett.*, 1996. (submitted).

[UT96] A.V. Ustinov and N. Thyssen. Experimental study of fluxon dynamics in a harmonic potential well. *J. of Low Temp. Phys.*, 1996. (submitted).

[VDT81] T. Van Duzer and C.W. Turner. *Principles of superconducting devices and circuits*. Edward Arnold, U.K., 1981.

[vdZROK94] H.S.J. van der Zant, R.A.M. Receuver, T.P. Orlando, and A.W. Kleinsasser. One–dimensional parallel Jospehson–junction arrays as tools for diagnostics. *App. Phys. Lett.*, 65(16), 1994. Preprint.

[VKT+96] I.V. Vernik, S. Keil, N. Thyssen, T. Doderer, A.V. Ustinov, H. Kohlstedt, and R.P. Huebener. Fluxon pinning in annular josephson junctions by an external magnetic field. *Phys. Rev. B*, 1996. (submitted).

[VLS+96] I.V. Vernik, N. Lazarides, M.P. Soerensen, A.V. Ustinov, N.F. Pedersen, and V.A. Oboznov. Soliton bunching in annular Josephson junctions. *J. Appl. Phys.*, 79:7854, 1996.

[VOU92] I.V. Vernik, V.A. Oboznov, and A.V. Ustinov. *Phys. Lett. A*, 168:319, 1992.

[WGU96] A. Wallraff, E. Goldobin, and A.V. Ustinov. Numerical analysis of the coherent radiation emission by two stacked Jospehson flux–flow oscillators. *J. Appl. Phys.*, 80(11):6523, 1996.

[YFTH94] H. Yamamori, A. Fujimaki, Y. Takai, and H. Hayakawa. Simultaneous switching on vertically stacked Josephson junctions with very thin intermediate electrode. *Jpn. J. Appl. Phys.*, 33:L846, 1994.

[YKN87] Masahiro Yuda, Ken'ichi Kuroda, and Jun'ichi Nakano. Small Nb/Al-Oxide/Nb Josephson junction fabrication using lift-off processes. *Jpn. J. of Appl. Phys.*, 26(3):L166, 1987.

Acknowledgements

First of all I want to express my gratitude to my supervisor Prof. Dr. Alexey Ustinov for his continuous support and encouragement. He made this work possible by sharing his vast knowledge about Josephson junctions and general physics with me.

I am thankful to the director of the Institute of Thin Film and Ion Technology (ISI) of the Research Center Jülich (KFA) Prof. Dr. Alex Braginski for providing the opportunity to conduct this research at his institute. I also like to thank him for his help concerning the administrative aspects of work.

The work I carried out in the course of this 'Diploma Thesis' (Diplomarbeit) benefited a lot from the collaboration with a number of members of the low temperature superconductivity group at ISI. In particular I gained a lot from the theoretical, computational and experimental expertise of Edward Goldobin. I enjoyed very much the cooperation on common projects and discussions on many issues of Josephson physics. My experimental work relied strongly on the excellent samples fabricated by Norbert Thyssen. I also thank him and Herrman Kohlstedt for their support in many physical and technical problems. I also profited a lot from discussions with and help of Susanne Lachenmann and Lilly Caputo. Additionally I want to thank all members of our group, who made this year into a successful and exciting one to me.

In particular I am thankful that I did get the possibility to get to know a large number of guests, including A. Golubov, V. Koshelets, M. Kuprianov, B. Malomed, N .F. Pedersen, S. Sakai, S. Shitov and many more, who visited our group during the time of my diploma thesis. I want to thank Prof. Boris Malomed for his contribution to one of the publications covered in this work and for his assistance (via email) in a number of theoretical problems that arose during my work. Moreover I appreciate having had the opportunity to participate in the radiation measurements of stacked long junctions with on-chip detector technology provided by S. Shitov, N. Iosad and V. Koshelets.

I want to express my thanks to the staff of the workshops and the secretaries of our institute for their help. In particular I like, to thank Falk Schmidt for his assistance in using the computing facilities at ISI.

I also would like to thank my family and all the friends who accompanied me during the years of my undergraduate studies in Aachen, London and Jülich. Especially I want to thank Philipp Kurz and Arno Straessner for the great and successful time we had.